Evolution of a crack-seal calcite vein network in limestone: a high resolution structural, microstructural and geochemical study from the Jebel Akhdar high pressure cell, Oman Mountains

Diplomarbeit

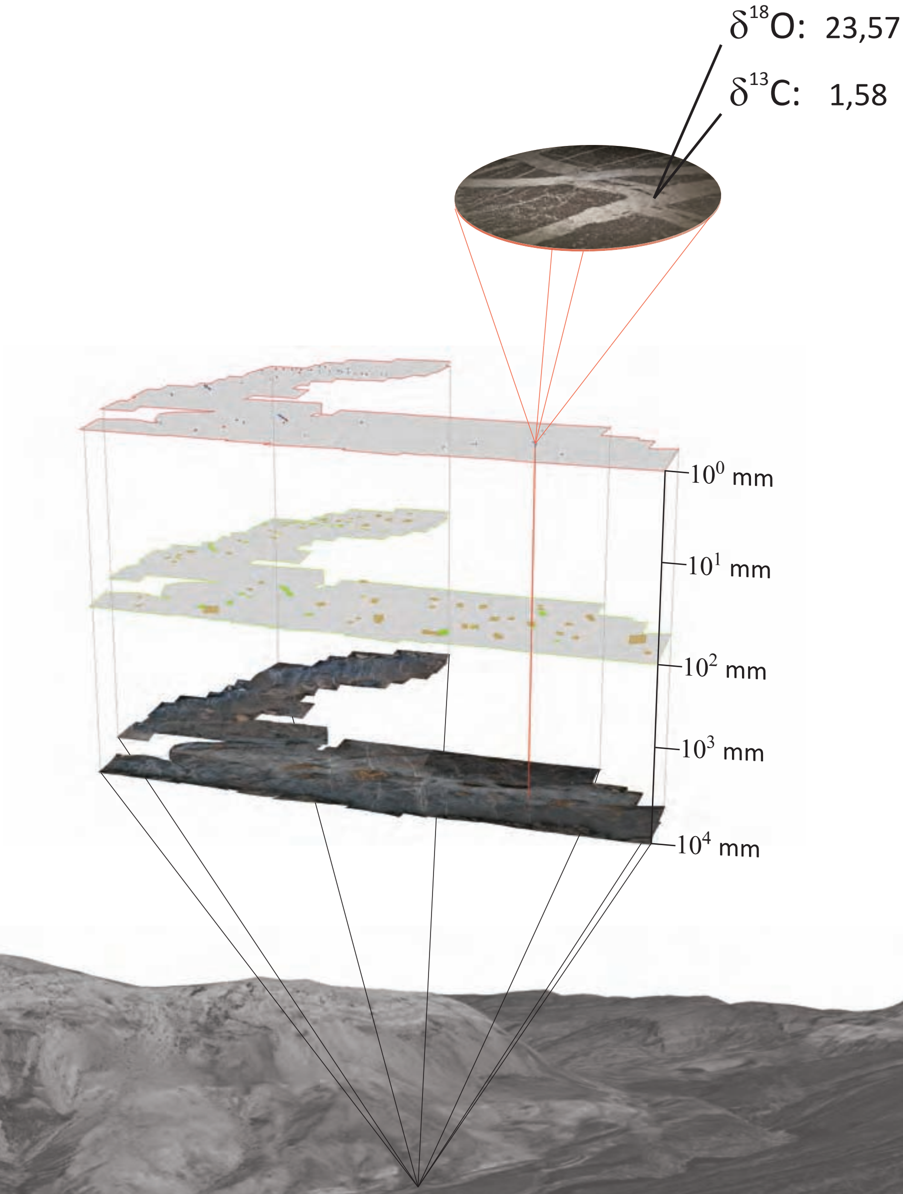

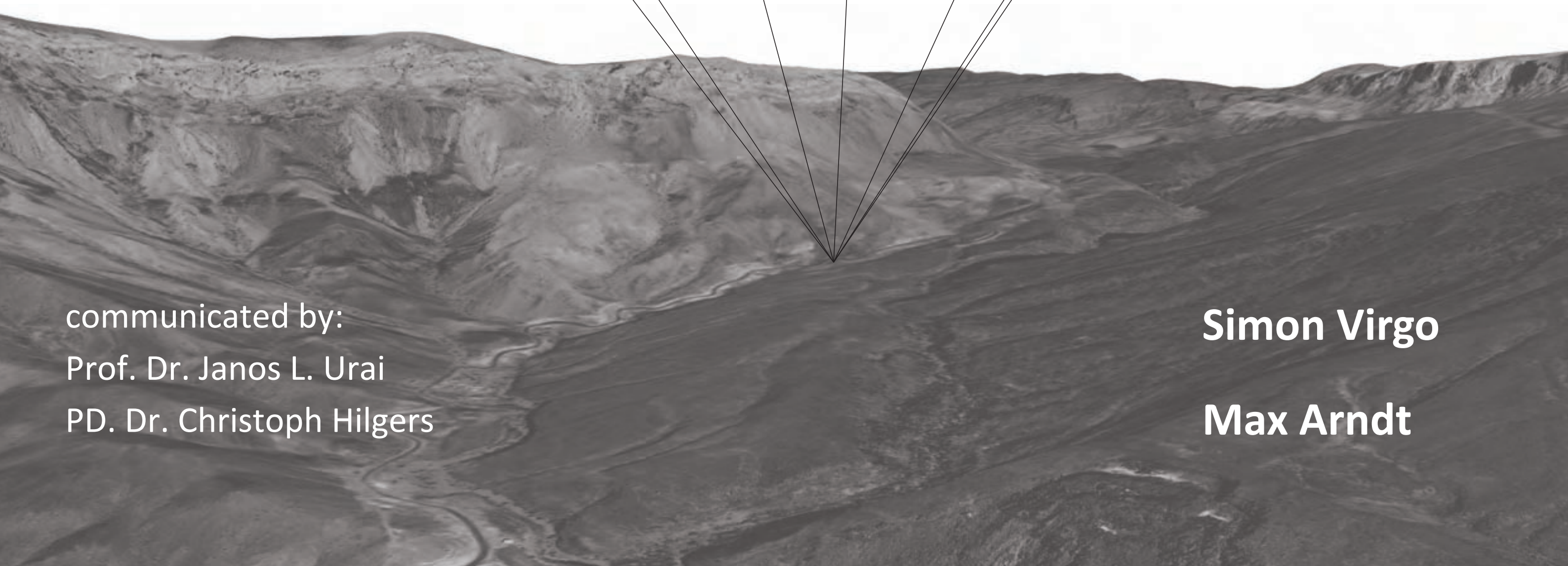

communicated by:
Prof. Dr. Janos L. Urai
PD. Dr. Christoph Hilgers

Simon Virgo

Max Arndt

Communicated by Prof. Dr. Janos. L. Urai
RWTH Aachen University
Geologie-Endogene Dynamik (531220)
Lochnerstrasse 4-20
52056 Aachen,
Germany

Diplomarbeit eingereicht am 20. September 2010 durch Cand. Geol. Simon Virgo und Cand. Geol. Max Arndt.

Ich versichere hiermit, dass die von mir erstellten Abschnitte selbstständig verfasst und keine anderen Hilfmittel als die angegebenen verwendet wurden.

Aachen, den 20. September 2010

Max Arndt

Ich versichere hiermit, dass die von mir erstellten Abschnitte selbstständig verfasst und keine anderen Hilfmittel als die angegebenen verwendet wurden.

Aachen, den 20. September 2010

Simon Virgo

Abstract

We present a workflow to acquire and create a 1.2 Gipapixel high-resolution outcrop panorama of a polished limestone pavement on the Western flank of Jabal Shams in the Oman Mountains. The outcrop panorama serves as a basemap to integrate structural, microstructural and geochemical investigations in a Geographic Information System.

The outcrop provides insight to the evolution of a high density calcite vein network in Limestone. The network as it appears in the outcrop has never been a network of interconnected open fractures, but it evolved dynamically. Subvertical dilatant veins with variable strike directions show mutual age relationships, indicating a uniaxial horizontal extension under close to lithostatic fluid pressure conditions. The high vein density and lacking abutting of veins suggest a quick restoration of bulk strength by fracture healing. Large vein apertures are realized by both vein stacking and a multitude of crack-seal cycles, as indicated by hostrock inclusions. The episodic growth of veins, which is accompanied by episodic fluid flow, is also suggested by large isotope variations across single veins. Existing veins act as anisotropies depending on orientation and their sealing driven strength regeneration. They significantly influence the formation of new fractures and largely control the geometry of the vein network.

Stable isotope measurements imply alteration of the host rock by external fluids prior to the formation of the vein network. The majority of the veins show a rock-buffered isotopic signature. Low d13C values in some veins suggest an influx of oxidized light hydrocarbons. The fluid system was unlocked by E-W striking normal faults, which is preserved in fault related veins by increased d18O values.

Contents

1 Introduction (Max Arndt)

1.1 Location

The Sultanate of Oman is situated on the northeastern rim of the Arabian Peninsula (Figure 1). The Oman Mountain chain spans from the Musandam peninsula in the north (at the street of Hormuz) to the Batain coast in the northeast of Oman. Figure 1 shows a true-color Landsat scene where the Oman Mountains appear as a dark brown band in Northern Oman.

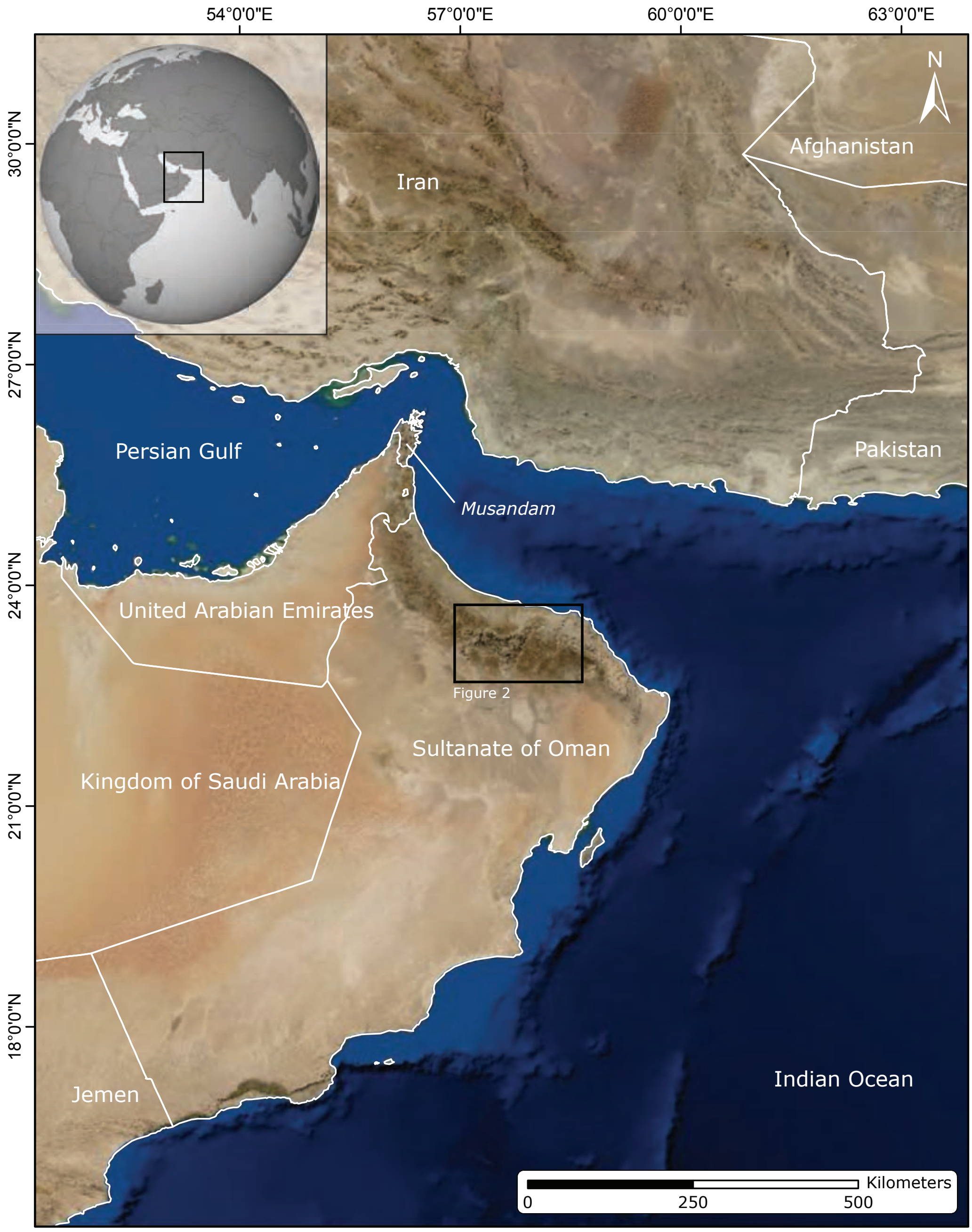

Figure 1: Landsat scene showing the eastern part of the Arabian Peninsula with the Sultanate of Oman and its bordering countries UAE, KSA and Yemen. The black rectangle indicates position of inset map in figure 2.

The large Jabal Akhdar anticline is the main topographic feature of the central Oman Mountains (Figure 2). The anticline has a wavelength of 60 km (Searle 2007) and its major fold axis strikes at the Northwestern tip close to Murri around NW beneath the Hawasina Window while turning more to EWE in the center part and finally NEN at the Northeastern tip close to Sumail (Figure *2*)(Searle 2007). The Landsat imagery in figure 2 shows the different major rock types of Northern Oman namely the famous Sumail Ophiolites appearing brownish while the Oman Exotics (allochthonous limestone - seamounts) appear in the SW of the Anticline with bright colors (Figure 2 and Figure 5). The sedimentary autochthonous limestone succession of Jabal Akhdar shows up as grey blue on the satellite image (Figure 2 and Figure *5*).

The area of interest namely the investigated "Discotheque pavement" outcrop is located on the western flank of Oman's highest peak, Jabal Shams. Jabal Misfat borders the western flank to the west. This is an Oman Exotic block that builds up a steep cliff facing Jabal Shams (see figure 4).

Figure 5 contains an intermediate zoom step (inset map) at a suitable resolution to display the Discotheque Pavement's location (actual image). The outcrop can be reached conveniently by following the black top road from Al Hamra to Jabal Shams after passing village Ghul, which is located at the entrance of Wadi Nakhr and a couple of small villages in Wadi Ghul (i.e. Minthar).

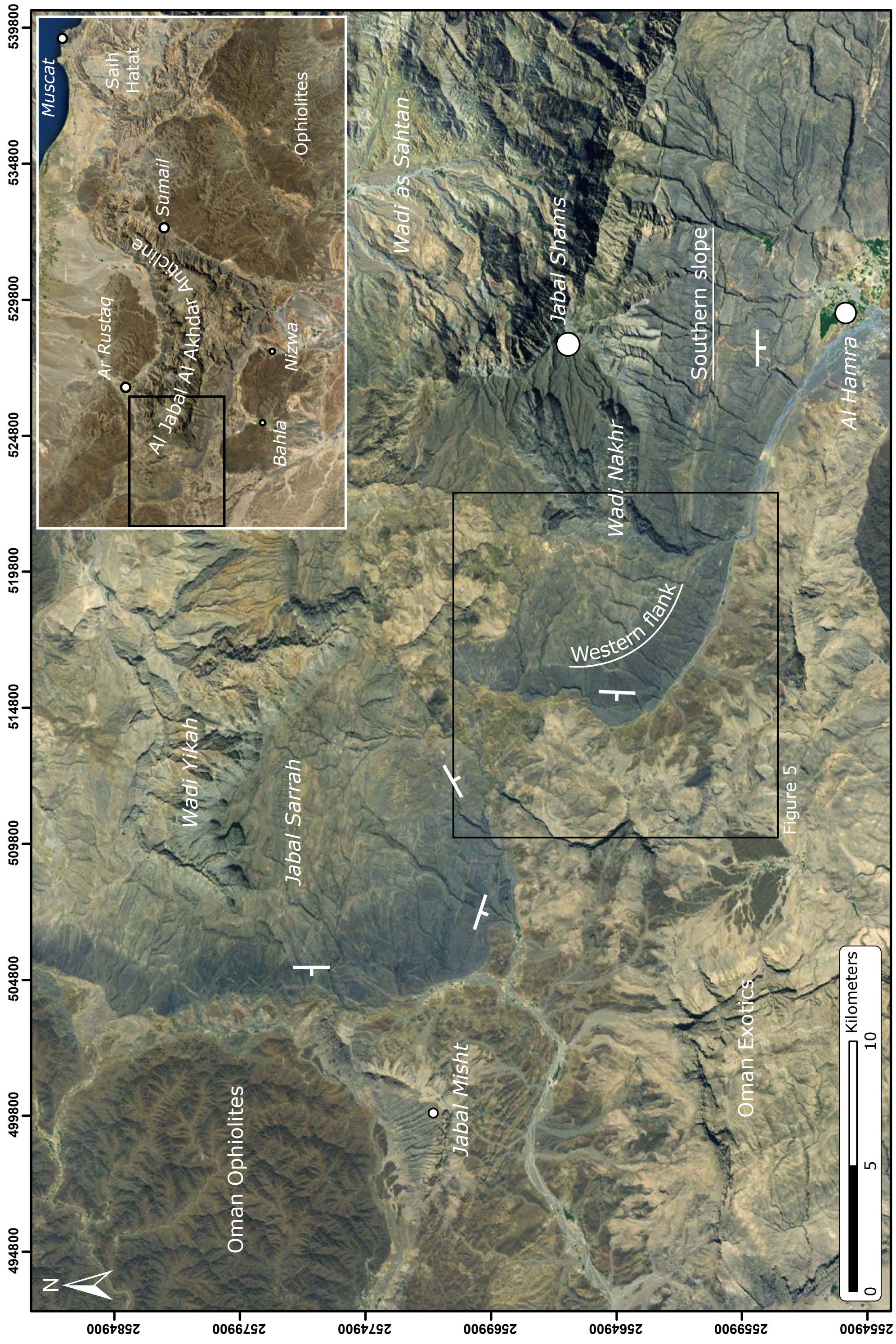

Figure 2: Landsat image of western Jabal Akhdar anticline. See inset map for image location. The black rectangle indicates location of inset map in figure 5.

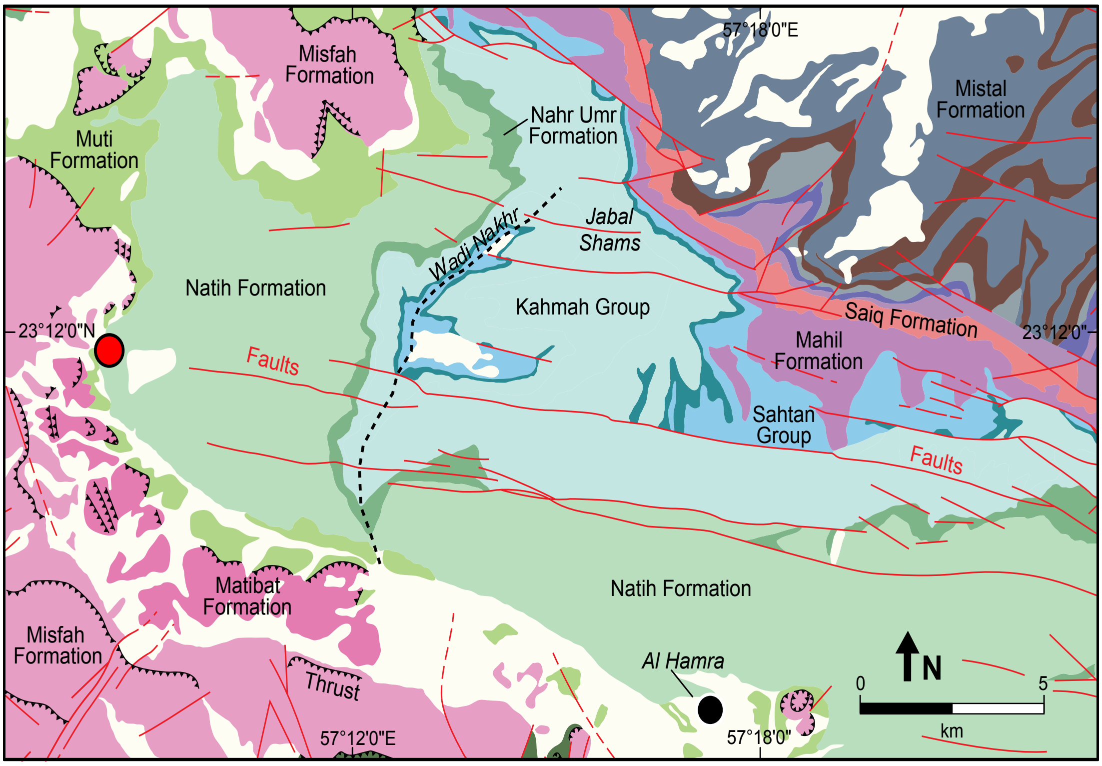

Figure 3: Basic geological map of the Jabal Shams area. The position of the investigated outcrop is marked with a red dot.

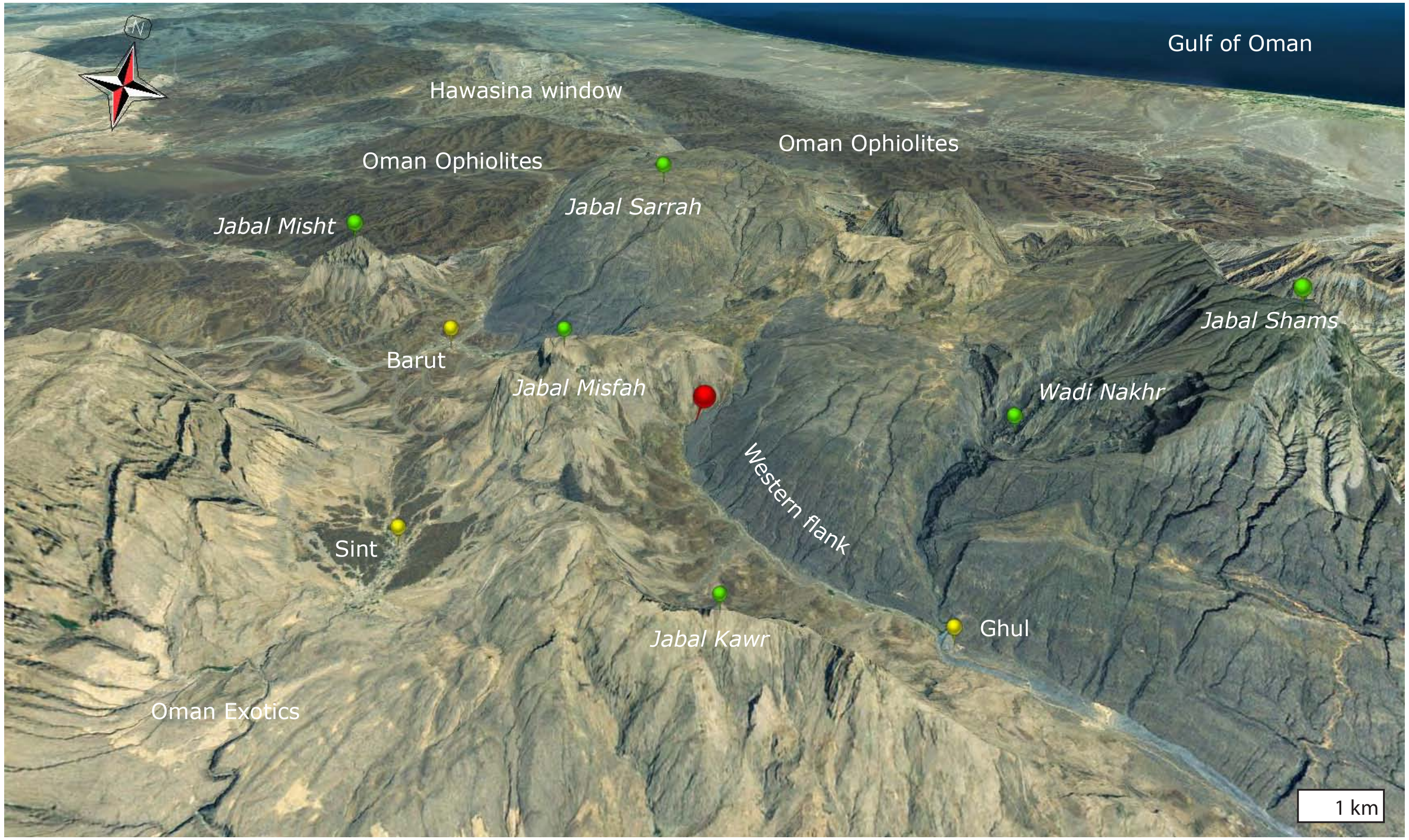

Figure 4: Artificial 3D view of the western Jabal Akhdar with oblique view to NNW. The autochthonous limestones (Hajar Unit) appear as dark grey- grey rocks. The lower left part of the image shows a massive block of bright grayish allochthonous limestones (Oman exotics). Note the brown colored rocks towards the NW. These are the Oman Ophiolites. Red pin marks the position of the Discotheque outcrop at the western flank of Jabal Shams. Mountain peaks are marked with green pins, while settlements are marked with yellow pins. Note the deeply incised canyon of Wadi Nakhr, the grand canyon of Oman. The drop shadow in the afternoon of Jabal Misfah allowed image acquisition during diffuse light conditions.

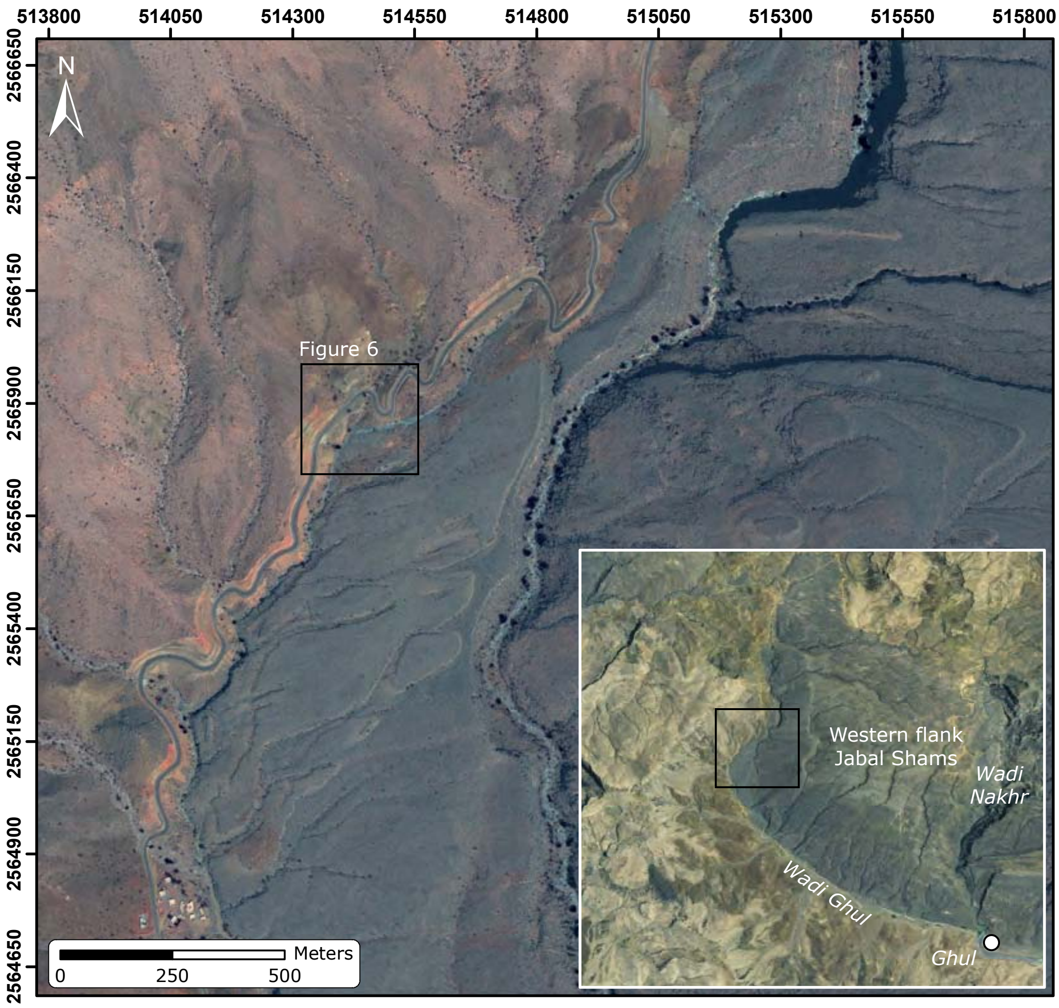

Figure 5: GeoEye satellite image scene giving an overview on surrounding landscape of the Discotheque outcrop. See text for further explanations.

Figure 5 displays the different rock types, i.e. the dark grayish to bluish limestone rocks of the upper Natih Formation, the bright yellow to orange shales and limestones of the Muti Formation and the light grey to reddish colored limestone rocks of the Oman Exotics. The road that was mentioned earlier can be seen easily as it is winding up to the Jabal Shams plateau along the geologic boundary between autochthonous limestones of the Natih Formation in the East and the allochthonous Exotics in the West. The surrounding geology of the Discotheque Pavement area will be explained further in the next chapter.

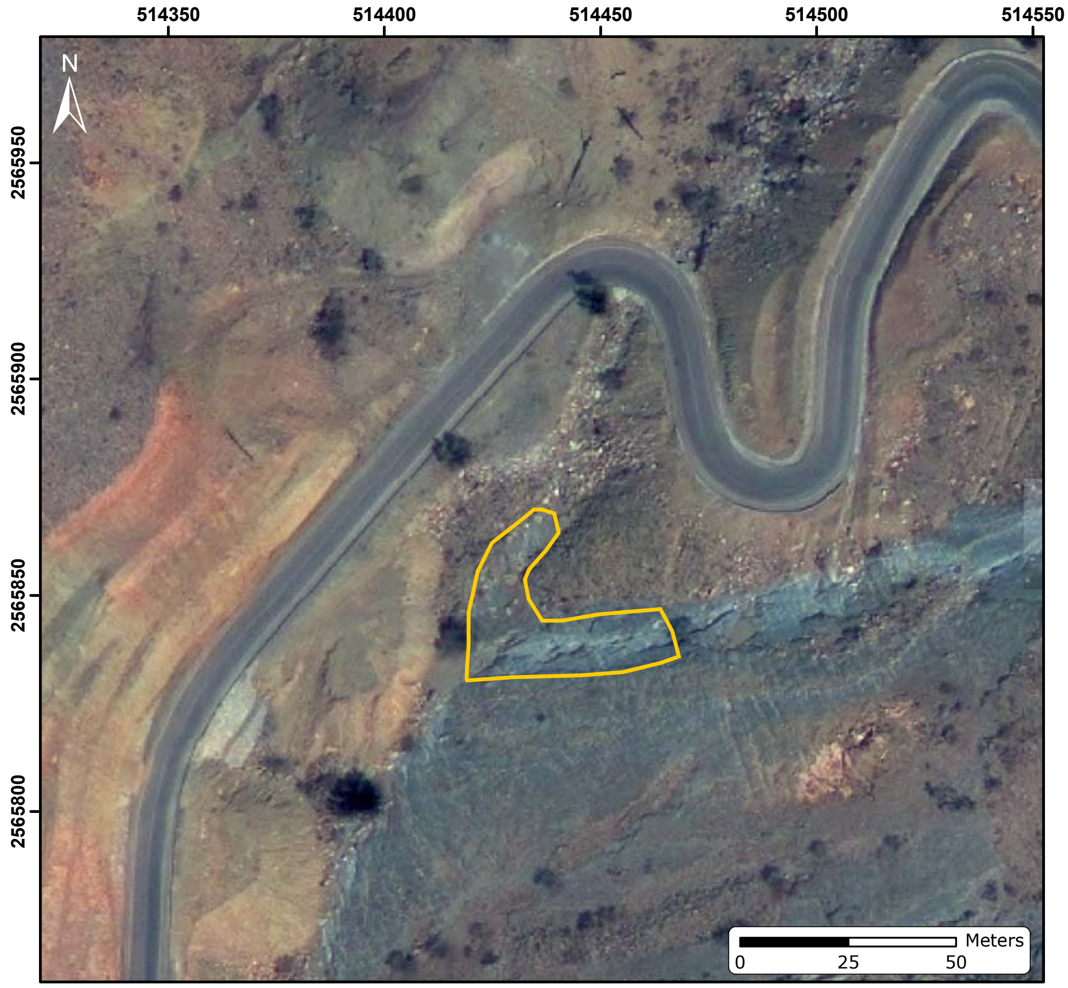

Figure 6: GeoEye satellite image at full resolution showing the Discotheque outcrop, which is right next to the road that leads to the top of Jabal Shams, Oman's highest mountain. The road has been build coincidently along the boundary between the Turonian Natih formation (SE from the road) and the Turonian-Coniacian Mutih formation (NW from the road).

The actual location of the investigated limestone outcrop is shown in Figure 6 (yellow line). It is closely situated to the road. The outcrop extends about 40 m from North to South and roughly 50 m from East to West. Two small wadis that act as drainage system in response to the episodic rainfall events have polished this particular area leaving a smooth surface on the limestone beds that can be studied.

1.2 Geologic Evolution

The Oman Mountains have a complex geological history. Hence we would like to focus on the geology that surrounds the Discotheque Pavement. The outcrop is part of the Upper Cretaceous Natih Formation, which was deposited from Cenomanian to Turonian times onto the passive continental margin between the Arabian plate and the Neothethys (van Buchem et al. 2002). The Upper Natih Formation is a carbonate ramp depositional system (van Buchem et al. 2002).

The Oman Mountains are part of the Alpine-Himalayan chain and formed during a NE directed subduction of the Arabian plate underneath the Eurasian plate (Breton et al. 2004, Hilgers et al. 2006, Holland et al. 2009b, Searle 2007). The subduction started as an intra-oceanic subduction in the Cenomanian (Searle 2007) and led to SSW directed obduction of the Sumail Ophiolites onto the passive margin starting in early Turonian (Breton et al. 2004, Hilgers et al. 2006, Searle 2007). The oceanic crustal rocks dragged along the Hawasina Nappes (Permian-Cretaceous volcano-sedimentary rocks, (Hilgers et al. 2006) as well as the time-equivalent syntectonic Aruma Group sediments (e.g. Muti Formation). The Hawasina nappes incorporate the shallow water carbonate rocks of the Oman Exotics, which are believed to be seamounts in the Hawasina basin (Bernecker 2007). The obduction ceased in early Maastrichtian (Breton et al. 2004, Searle 2007). Hence the Autochthonous Natih limestones were rapidly overridden and buried. That led to high fluid overpressures in the autochthonous rocks, which caused several phases of veining and faulting (Hilgers et al. 2006, Holland et al. 2009b). Breton et al proposed an upper Anchizone metamorphism with pressures of 2-4 kb and temperatures lower than 200°C in the Autochthon (Breton et al. 2004). The ongoing convergence of Arabia and Asia forced the exhumation of the autochthonous platform carbonates in correspondence with contemporary erosion of overlying rocks, namely the Hawasina nappes and the Ophiolites. Searle et al proposed two main phases of tectonic uplift of Jabal Akhdar, the first being a ramp culmination towards the foreland basin during late Cretaceous and the second uplift in post-late Eocene/Oligocene (Searle 2007). Robertson suggested that the carbonate platform edge was initially uplifted during the Turonian and deeply eroded, creating the 'Wasia-Aruma break' (Robertson 1987). However the dome shape that was caused not only by NE-SW compression, but also by NW-SE compression (Searle 2007) is not well understood.

1.3 Stratigraphy

The outcrop of interest, the Discotheque Pavement is part of the Natih Formation (Natih A; Homewood et al. 2008, Razin 2010). The Albian-Cenomanian-Turonian Natih Formation is part of the Lower-Upper Cretaceous Wasia Group, which belongs to the Permian-Cretaceous Hajar unit (Autochthon B) in the Oman Mountains (Figure 7; Breton et al. 2004). It conformably overlies the Nahr Umr Shale and is unconformably overlain by the semi-autochthonous Muti Formation of the Aruma group (Wasia-Aruma Break (Robertson 1987)). Well-known lateral age-equivalent formations in the Middle East are the Mauddud Formation, the Mishrif Formation and the basinal Shilaif-Khatiyah Formation (van Buchem et al. 2002). The formation is famous since it is one of the most productive oil-bearing carbonate deposits worldwide (Filbrandt et al. 2006, van Buchem et al. 2002). The Formation provides both source and reservoir rocks due to it's own depositional sequences (van Buchem et al. 2002). Two major depositional systems control the facies of the formation: the first is a flat-bedded, mixed carbonate-clay ramp dominated by benthic foraminifera and the latter one is a carbonate-dominated ramp bordering an intrashelf basin with abundant rudists and organic-rich basinal facies (van Buchem et al. 2002). The Natih A itself consist of shallow water carbonate platform limestones exclusively. It is discussed that top of Natih A is an exposure surface (sub-aerial erosion) since there are some incisions and terrigeneous influx associated with in several place (W. Khamah near Tanuf, W. Muaidin, J. Madar, J.Qusaibah, etc.). This exposure could have developed in a fore bulge context just prior to the major flexure and flooding of the Arabian platform recorded by the deposition of the Muti Fm. (Homewood et al. 2008, Razin 2010, van Buchem et al. 2002).

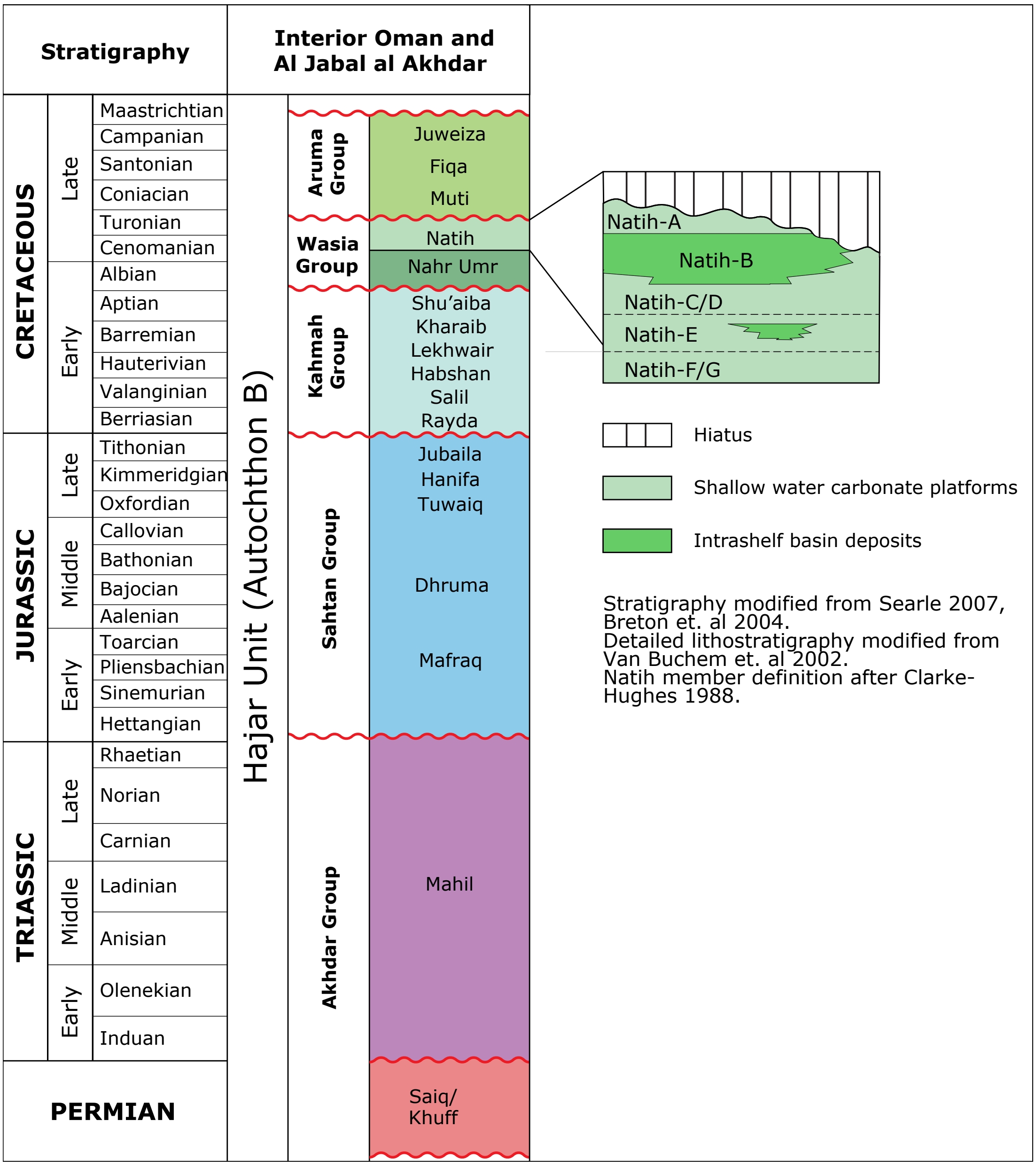

Figure 7: Regional Stratigraphy of the area of interest. The figure contains combined information from Breton et al. 2004, Searle 2007 and van Buchem et al. 2002.

1.4 History of Vein research in the Oman Mountains

Since the world class limestone outcrops in the Jabal Akhdar region allow detailed and diversified field investigations, several workers in the past did focus on research on the ubiquitous veins in the Oman Mountains. Hilgers et. al started in 2006 differentiating seven vein generations and defining a relative timing of these generations (Hilgers et al. 2006). Stylolite veins (#1) perpendicular to bedding were followed by bedding-normal veins (#2), which cross cut the bedding parallel stylolithes. The timing of pinch and swell veins (#3) was not entirely constrained. However bedding parallel veins with top to north shear (#4) truncated vein generation #2 under lithostatic fluid pressure conditions and were themselves offset by veins related to normal faulting (#5, #6). Thrust veins (#7) cross cut veins #2, #4 and #5 and are therefore believed to be the last generation of veins. The authors found that the veins are consistently filled with calcite and quartz crystals. Oxygen and Carbon isotope studies revealed a host rock buffered geochemical signature for generation #2-#5, while during faulting a more open system allowed external fluid to infiltrate the rocks at drained conditions and precipitate the youngest sets of veins (#6 and #7). Hilgers et. al proposed fluid overpressures until normal faulting released the pressure by draining the rock sequence. The study and sample acquisition focused mostly on deep wadis across the entire dome structure (Hilgers et al. 2006).

Vein generation	Description	Evidence for relative age relationship	Regime
#1	Stylolite vein	Cross cut by extension veins (#2)	σ1 normal to bedding
#2	Extension vein, boudinage vein	Truncated by bedding-parallel vein (#4)	σ1 normal to bedding
#3	Pinch & sell vein	Undeformed extension vein nearby, truncated by normal fault (#5, 6), relative timing to #4 unclear	σ1 oblique to bedding
#4	Bedding-parallel vein	Displaced by normal faults (#5), top-to-the north directed shear indicators indicating bedding parallel slip, crosscutting relationship of #4.1 and #4.2 unclear	σ1 oblique to bedding
#5	En echelon extension vein array	Aligned along and often displaced by normal faults (#6), no visible offset by bedding parallel slip (i.e. #4)	σ1 normal to bedding
#6	Veins in dilation sites of normal faults	Truncate en echelon veins (#5)	σ1 normal to bedding
#7	Thrust veins	Cross cuts #2, #4, and #5	σ1 oblique to bedding

Table 1: Vein sets in the Jabal Akhdar dome (after (Hilgers et al. 2006))

Holland et al. published a detailed study in 2009 concentrating on the southern flank of Jabal Shams incorporating relative timing of structural elements, paleo-temperatures and a schematic evolutionary model for the so called Jabal Akhdar high pressure cell (Holland et al. 2009a, Holland et al. 2009b).

Referring to the #2 vein set of the work by Hilgers, Holland defined four fracture (vein) generations, which suggested an anticlockwise rotating stress field. The generations have been evaluated from systematic recording of vein overprinting relationships over the entire field area. Holland et al. agreed with Hilgers et al. about the formation of veins due to high fluid overpressures and about the fact that normal faulting released the fluid overpressures. Both studies propose lithostatic fluid pressure conditions during emplacement of bedding parallel shear and related top to northeast shear (Hilgers et al. 2006, Holland et al. 2009b). The interpretation on the succession of structural events was based o the hypothesis that each fracture and fault has been healed before a next event occurred.

Holland et al published a second paper dealing with the evolution of crack-seal pattern (pseudo Zebra-carbonates) in the area. The authors investigated the relationship between the mechanical strength of host rock (matrix “T_M”) vein cement (“T_C”) and the interface (matrix “T_I”). Image analysis and stable isotope measurements were concluded in a model that proposed different crack-seal patterns that form if the relationship of the three different strengths is varying (see figure 8 afterHolland & Urai in press).

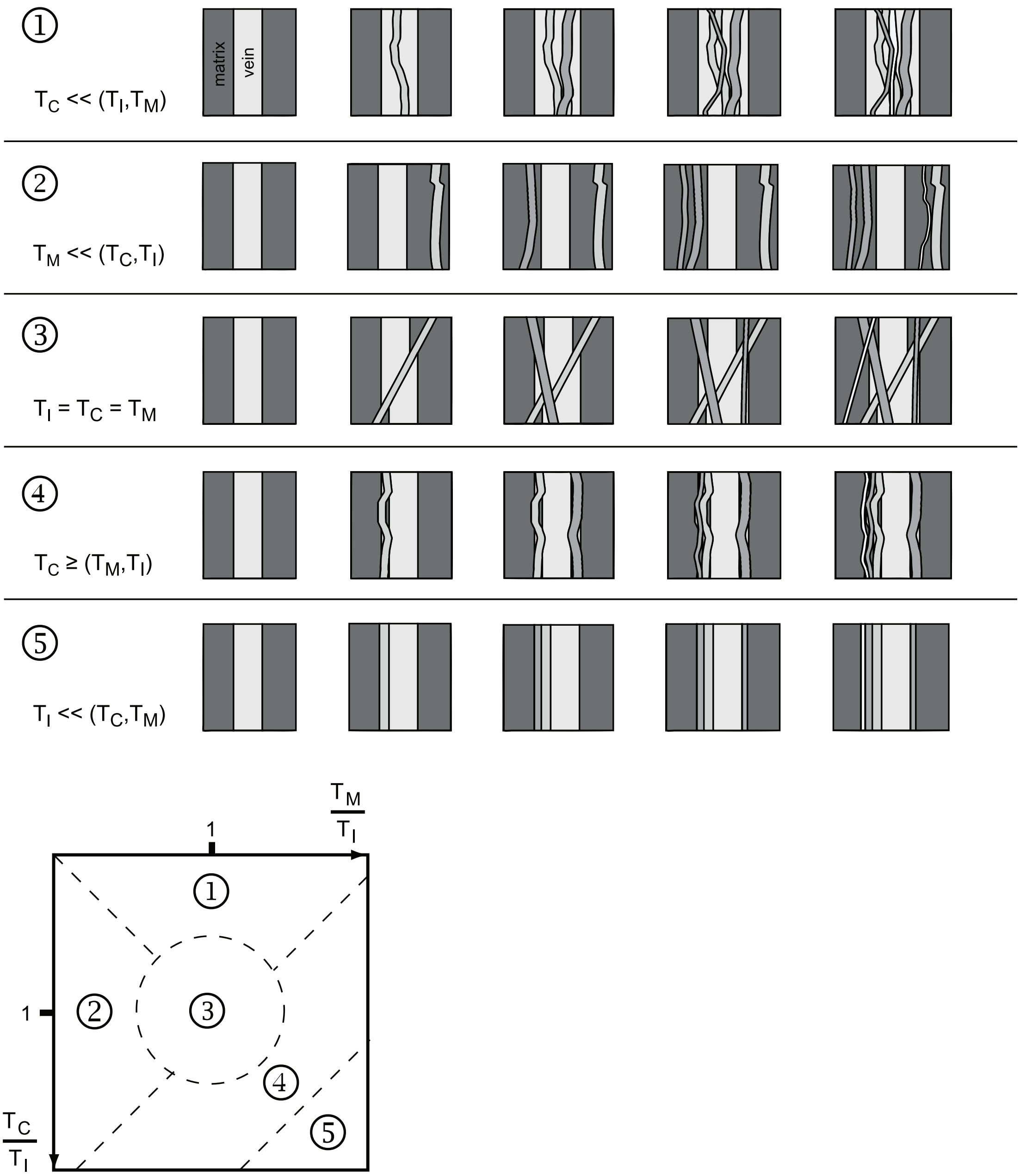

Figure 8: Conceptional model on the impact of the mechanical strength of matrix (TM), vein cement (TC) and the interface (TI) on the formation of successive fracture and healing events (simplified model; not to scale). From (Holland & Urai in press).

1.5 Study intention and used methods

1.5.1 Multi-scale study of vein networks

We decided to combine observations from multiple scales in one study. The aim was to capture an outcrop comprising three polished bedding planes. A huge image that has been created by stitching smaller images together shall serve as a convenient foundation to allocate all observations made on different scale. We did not just work at outcrop and meso scale (e.g. vein age relationships), but also on micro scale (microstructural analysis) and integrated stable isotope measurements.
By creating the dataset of different structures on different scales and linking observable properties with experimentally measured values we hope to get insights on the evolution of highly complex calcite vein networks.

1.5.2 Taking the outcrop home

One of the major ideas about the project was not just to measure and acquire data of geological structures, but also to create a virtual outcrop and acquire data in a way that it can be displayed on the virtual outcrop at the right location. After putting a 2x2 m grid on the outcrop surface we were able to very accurately localize every observation that has been made.
The virtual outcrop can be used to investigate relationships of structures and trends of measured properties that may be related to structures. The work does not only allow analysis of data that exist, but also adding field information and measurement that are made in the dataset at home.

1.5.3 Fully georeferenced dataset

As described in the previous chapter all information that has been collected has been attached to the outcrop panorama (georeferenced). The image has been rectified in a geographic information system (GIS) with a customized coordinate system that is based on the 2x2 m grid. This setup enables the allocation of any observation that has been made in the field and to make further measurements on any structure and geometry that is visible on the outcrop panorama or either detail images, thin sections etc. Every measurement can be assigned to its exact location and the GIS system enables us to produce all sorts of maps and visualizations based on the georeferenced data.
The integration of outcrop imagery with field measurements and experimental data hosted in a geographic information system is an innovative approach to display, measure, analyze and evaluate geological structures.

2 Methods (Simon Virgo)

2.1 Outcrop Panorama

2.1.1 Dipod Design

The need to take photographs vertically downwards from an elevation of 2-3m could not be met with any commercially available tripod design. With the help of Franz Gruemmer (Geological Institute, RWTH Aachen University) we constructed a dipod, basically consisting of two expandable telescopic aluminum rods (originally sold as gardening tools) and a custom-made aluminum cross bar that can carry a digital camera via a quick release plate (Figure 9).

Since the dipod has only 2 legs it is not able to stand unsupported. It is designed to be operated by 2 people. Spirit levels at the telescopic legs allow the operators to accurately level the dipod.

Two aluminum protection pins that are attached perpendicular to the cross bar protect the camera from damage in case the dipod tilts over. The Telescopic legs can be locked in 4 positions, allowing shots from the heights of 1,57m, 1,85m, 2,30m and 2,60m. The angle between the legs was matched to the angle of field of the camera setup, so that at any height of the shot the legs of the dipod do not appear on the photograph.

Figure 9: Assembly of the photography setup. The camera is pointing vertically downward. In the pictures the telescopic legs are locked in the second position.

2.1.2 **Camera Setup**

We used a Nikon D 80 digital SLR together with a Tokina AT-X 4,0/12-24 mm Pro lens to shoot the photographs (tiles) for the mega stitch. The D80 ‘s sensor has a resolution of 10.8 megapixels at an area of 23,6mm x 15,8mm. Because of the small sensor, the field of view provided by the lens cannot be used completely. The field of view is analogue to a full frame camera with a lens 18-36mm focal length. However this range is suitable to cover a sufficiently big area from 2m – 3m distance.

Even at low focal length the distortion of the Tokina lens is relatively low for a wide angle lens and easy to correct (see 2.1.6.1) (Schroiff 2010). A camera cable release was used to remotely fire the shots.

2.1.3 **Gridding the outcrop**

After measuring and sketching the outcrop, we created a NS and EW trending orthogonal grid with a cell size of 2m for referencing the merge afterwards and roughly locate age relationship observations and drill sites in the outcrop.

To establish the grid, we spanned an orthogonal wireframe across the outcrop, parallel to North-South and East-West direction, which is subparallel to the mean strike and dip directions of the outcrop surface. The wireframe did at no time cover the outcrop in a whole but was subsequently moved over the outcrop by discarding existing strings and establishing new ones.

Each intersection of the 2m spaced strings was projected normal to the grid plane onto the ground and marked with a permanent marker pen. These grid points mark the junctions of 4 cells.

Each 2m x 2m cell was named by its XY-position in the outcrop with a letter and a number, ranging from “1” to 24” West to East and “a” to “s” from South to North.

Figure 10: As the first step the 2 orthogonal axes of the grid are established with measure tapes and carefully beared.

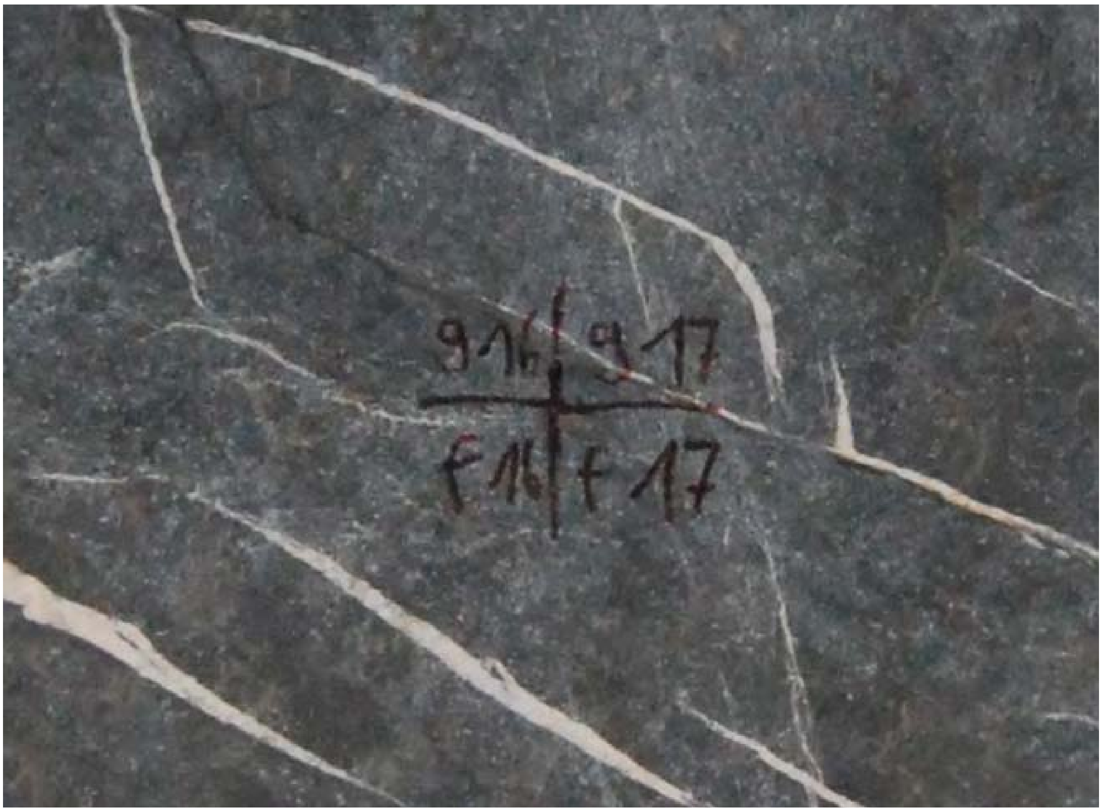

Figure 11: Grid points are drawn onto the outcrop with a red permanent marker pen. The grid point on the picture is the common point of 4 cells: f 16 (bottom left), f 17 (bottom right), g 16 (top left) and g 17 (top right)

2.1.4 Image acquisition

The panorama of the outcrop consists of 191 single 10.8 Megapixel photos (tiles). To create panoramas from Photographs, some important issues have to be considered during the acquisition of the Images.

2.1.4.1 Acquisition procedure and Dipod leveling

The photographs were taken by stepwise carrying the dipod in E-W and W-E oriented track over the outcrop. After reaching the border of the gridded area, the dipod was moved 2m southward from the finished track and a new track was started parallel to the finished one, but in the opposite direction (meander scan pattern).

The surface dips with 15° roughly to the West (see chapter 1.1). Because we wanted our photos to be taken orthogonal to the surface, we kept the two legs of the dipod parallel to the movement direction (E-W). The tilt of the camera towards the West was therefore the same as the average dip of the surface in East West direction between the two points where the legs of the dipod touched the ground. The spirit levels on the dipod legs were than used to eliminate any tilt of the camera towards the North or South before a photo was taken.

2.1.4.2 Coverage and overlap

Automatic photo stitching necessitates that photographs overlap. The bigger the common area on 2 or more photos is, the easier it is for the software to align and blend the pictures. For targets with sufficient contrasts and non-recurrent textures (like our outcrop), 20% overlap of adjacent images is usually sufficient for automated panorama creation. The coverage of each photograph of the series is ~3,8 m in N-S and ~2,6 m in E-W direction. For each photograph the guiding leg of the dipod was placed exactly on a marked grid point, which ensured that the distance from one shot location to the next was constantly 2m. The theoretical overlap of the photographs is therefore 180 cm (47%) in N-S direction and 60 cm (23%) in E-W direction. Nevertheless it can differ due to topography (see Chapter 2.1.5.1.3)

2.1.4.3 **Illumination**

To get a consistent panoramic picture in the end, the illumination conditions during the acquisition of its tiles should stay as constant as possible. While changes in the overall light intensity and color of the light can be corrected automatically during picture acquisition or post processing, changes in illumination direction and moving shadows can lead to big problems for the automatic photo stitching, since they would change the appearance of a common area on 2 pictures in between their acquisition. A major problem of the dipod design is that it drops a shadow into the aimed area if operated in direct sunlight. The only way to avoid a costly flash setup was therefore to take the picture during times of diffuse natural illumination.

Especially in Oman this is a problem!

Because of its geographic position, in Oman the change from day to night happen very rapidly. The times of diffuse lightning during dusk or dawn are therefore very short.

Although the precipitation in the Jabal Akhdar is higher than in the rest of Oman, (Metz 1994) a continuous cloud cover that would provide a diffuse illumination, is present at only a few days a year and may usually be accompanied with heavy rainfall. Fortunately in the Southwest and the West of the outcrop the merging foothills of Jabal Misfah and Jabal Ghul, that form a steep and high cliff towards the East (Figure 22), shield the outcrop from sunlight: In the afternoon (during the field season around 16:00h) the shadow of the cliff reaches the outcrop and provides 3 hours of diffuse illumination. Nevertheless the light intensity is still high enough to get good photographs. A weak illumination of the outcrop would lead to a drop in picture quality: a longer exposure time would increase the risk of camera movement and thus blur of the picture. By increasing the ISO sensitivity of the camera, this effect can be reduced. However the sensitivity should not exceed a certain value (in our case ISO 800) to restrict noise within the pictures. Due to the high air temperature especially the thermal noise might contribute significantly to the overall noise in the photographs.

2.1.5 Panorama creation

2.1.5.1 General issues and systematic problems

2.1.5.1.1 Grid accuracy

To establish the grid on the outcrop, the first cord in NS direction as well as the first cord in EW direction had to be carefully oriented with a magnetic compass (Figure 10). The inaccuracy of this method was estimated to be up to 3° (northing error). The maximum deviation from a right angle between the NS and the EW trending strings is therefore 6°. Multiple measurements with different compasses and with different facing directions however suggest that the deviation from a right angle is less than 1°. The strings were fixed at equal heights (~50 cm) at each side of the outcrop.

After establishing the first two strings, all parallel strings of the wireframe could be spanned without using a compass but only by measuring distances, which can be done with an accuracy of a few millimeters. By aiming with the eye over multiple strings, we made sure that the wireframe's plane does not twist.

Although the dip of the surface of the outcrop (which is a weathered bedding surface) does not significantly change across the outcrop, in some places the fluviatile erosion created a significant small-scale topography (wash-holes, bedding steps) with amplitudes up to 1 meter.

These weathering features are the most important source of error, not only for the stitching process (see chapter 2.1.5.1.3), but also for the precise placement of the grid points on the outcrop:

At each intersection of the 2 m spaced strings a grid point is projected normally to the plane of the wireframe onto the ground using one of the telescopic legs of the dipod. The inaccuracy of this method is estimated to be 10°, which means that the marked point is within a 10° error cone around the real normal. The placement error of the grid points is therefore less than 18% of the distance between the outcrop surface and the wireframe. Since this distance is usually less than 50cm, the accuracy of most of the grid points is within 10 cm. In some cases where the surface is incised by the weathering the error can grow to up to 30 cm.

2.1.5.1.2 **Lens distortion**

To successfully stitch overlapping photographs it is necessary that a photographed feature appears on a photograph always with the same geometry, regardless of where it is located in the picture. For the used camera setup this is not given. Especially wide-angle zoom lenses always show an amount of lens distortion.

The two types of distortion that can be distinguished are radial and tangential distortion (Ray 1999). The resulting errors from the radial distortion are symmetric to the principal point of the lens, where the projection ray is normal to the image sensor and the distortion is zero. From there the distortion grows towards the edges of the picture. It is dependent of focal length and can appear as a barrel type distortion (short focal length, linear features in the image bulge outward) or as pincushion type distortion (long focal length, linear features in the image bulge inward). Tangential distortion is non- systematic and occurs mostly in low quality lenses due to errors in alignment of optical elements. For a known camera setup and a known focal length it is possible to eliminate the effects of the radial distortion by image post processing. This however reduces the image quality since the image has to be resampled and interpolation errors occur. It is therefore important to choose a lens with low radial distortion. Test shots showed that the tangential distortion of our setup is negligible.

2.1.5.1.3 **Parallax error and perspective distortion**

A photograph of a 3 dimensional object is a projection into a 2 dimensional image space. The viewing angle (the direction defined by the position, the object is viewed from) therefore determines how the object appears on the photograph. Succinctly said: an object may look different viewed from the east than viewed from the west.

The usual way to create a panoramic image is to shoot overlapping photographs from a fixed camera position (at best with a stationary tripod).

The direction and tilt of the optical axis and in some cases also the focal length of the camera may be altered between the shots, but the camera remains stationary. The tiles of the panorama show different excerpts of the scene, but the viewing angle to the scene, as a whole does not change. Features in overlapping tiles are imaged always from the same viewing angle and therefore appear identically on the tiles.

Unfortunately the outcrop does not offer any elevated sites in it's surrounding that would allow to photograph the whole outcrop from a stationary position.

In our approach we alter the position of the camera during the image acquisition. We move the camera over the outcrop while keeping the optical axis of the camera setup perpendicular to the surface. This means that for every shot the viewing angle towards the outcrop as a whole changes.

As soon as the photographed surface is not perfectly planar, this leads to a parallax error: a topographic feature that appears on two adjacent tiles is imaged from another viewing angle on the one tile than it is on the other.
The effect of this error is that features in the overlapping area of the tiles are distorted relative to each other or can even disappear on one tile. The steeper the topography of the surface is, the more critical is the resulting error.
If the surface was perfectly planar, the parallax error would be reduced to a simple perspective distortion. For tiles acquired with the optical axis orthogonal to the surface, this distortion is already removed by the lens correction.
Since we have no influence on the topography of our outcrop, two variables can be tuned to minimize the parallax error during image acquisition: the camera height and the focal length. A higher focal length narrows the field of view of the camera setup and the maximum off-axis angle in each tile is lower. The disadvantage is that it increases the number of pictures that has to be taken to cover the whole outcrop. This can be countered by increasing the height of the camera. Increasing the distance between the camera and the surface additionally reduces the impact of the topography. However a bigger dipod would be much harder to operate.

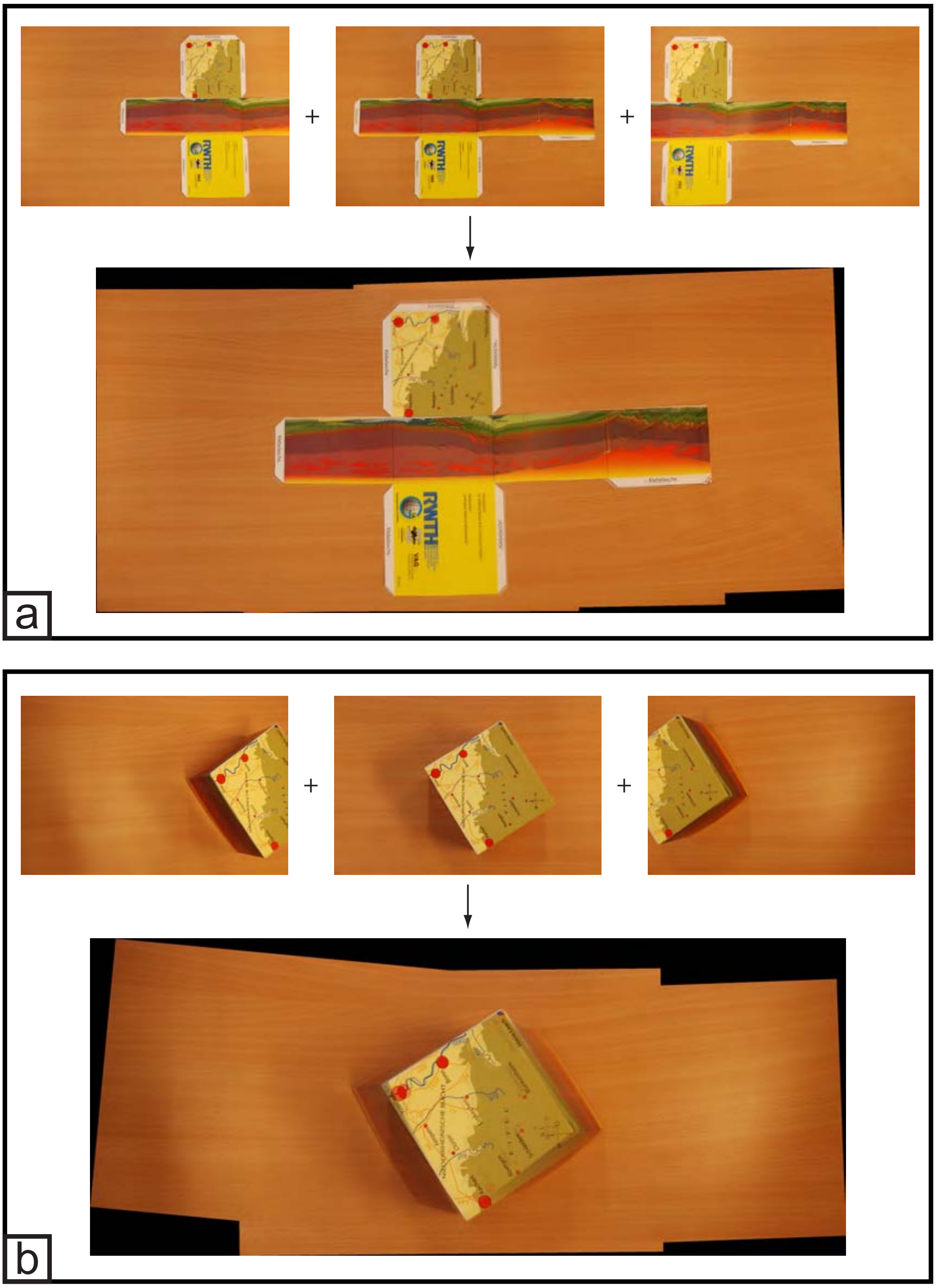

Figure 12: a planar surface (a) and a 3D object are photographed by parallel shifting of the camera. The photos are stitched together with autopano giga 2 and rendered with a linear blender to highlight the alignment error. The topography of the cube in Figure B causes a big error due to the parallax effect.

2.1.5.1.4 **Strike correction**

The way we set up the grid, acquired the photographic tiles and referenced the panorama results in imagery that is not horizontally orientated. The virtual position of the observer is not vertically above the outcrop, as like in a orthorectified aerial or satellite image, but views the outcrop from a position normal to the bedding (256/15). The imagery is therefore homogenously stretched in the direction of dip (Note that it is NOT a perspective distortion!). Since a strain changes all angles inside the pictures that do not coincide with the main axes of the strain ellipsoid (Ramsay & Huber 1984) strike directions measured in the referenced panorama must be corrected.

For this correction, Wettstein's Equation can be used (Ramsay & Huber 1984):

$$\tan\phi' = R^{-1} \tan\phi$$

Where f is the angle before deformation, f' the angle after deformation and R the ellipticity of the strain ellipse.

The ellipticity of the strain ellipse that transforms measured strike from the panorama into real strike depends only on the dip of the bedding (μ) and can be written as .

f is the deviation from the long axis of the ellipse, which is the strike of the bedding (166° or 346°)

However since the dip of the bedding is small in our outcrop, the deviation of the corrected values from the measured values is less than 1 degree for any direction.

2.1.5.2 **Software Autopano Giga 2**

After several dissatisfying attempts to merge parts of the tiles with Adobe Photoshop CS 3 (Adobe 2007), we tested several more specialized commercial and non-commercial Software to create the Panoramas. We finally were successful with the Software Kolor Autopano Giga 2 (Kolor).

Photoshop offers only a few presets for automatic panorama creations. After loading the pictures into the program and running the panorama function there is no way to have further influence on the matching and adjusting of the tiles as well as on the rendering.

Autopano Giga 2 on the other hand has a modular architecture, which allows full freedom of manipulation after the automated panorama creation. The rendering process itself is outsourced to a separate module.

The Software is capable of using multiple cores as well as the full resources of a 64 bit system and is therefore able to handle big datasets very time efficiently.

2.1.6 **Workflow**

2.1.6.1 **Image pre-processing**

The first step in the Workflow was to convert the RAW images from the camera into JPEGs using a Batch conversion tool in Photoshop CS3 (Adobe 2007).

During the conversion the white balance as well as the exposure was automatically leveled to maintain homogenous appearance of all pictures and to eliminate the effect of globally changing lightning conditions during the image acquisition.

Furthermore the contrast was enhanced to highlight the veins in the carbonate hostrock.

2.1.6.2 **Definition of subsets**

The stitched outcrop consists in total of 191 tiles.

After the attempt to create a panorama with all available pictures brought unsatisfactory results, we decided to divide the panorama into 5 separately treated subsets.

The Northern part of the outcrop is separated from the southern part by a bedding step of up to 2m height.

This topographic gap makes it impossible to align the subsets in this area accurately because it causes a very high parallax effect. Since the surface close to the gap in the southern part is covered with gravel and therefore does not contribute useful information to the dataset, it was clipped.

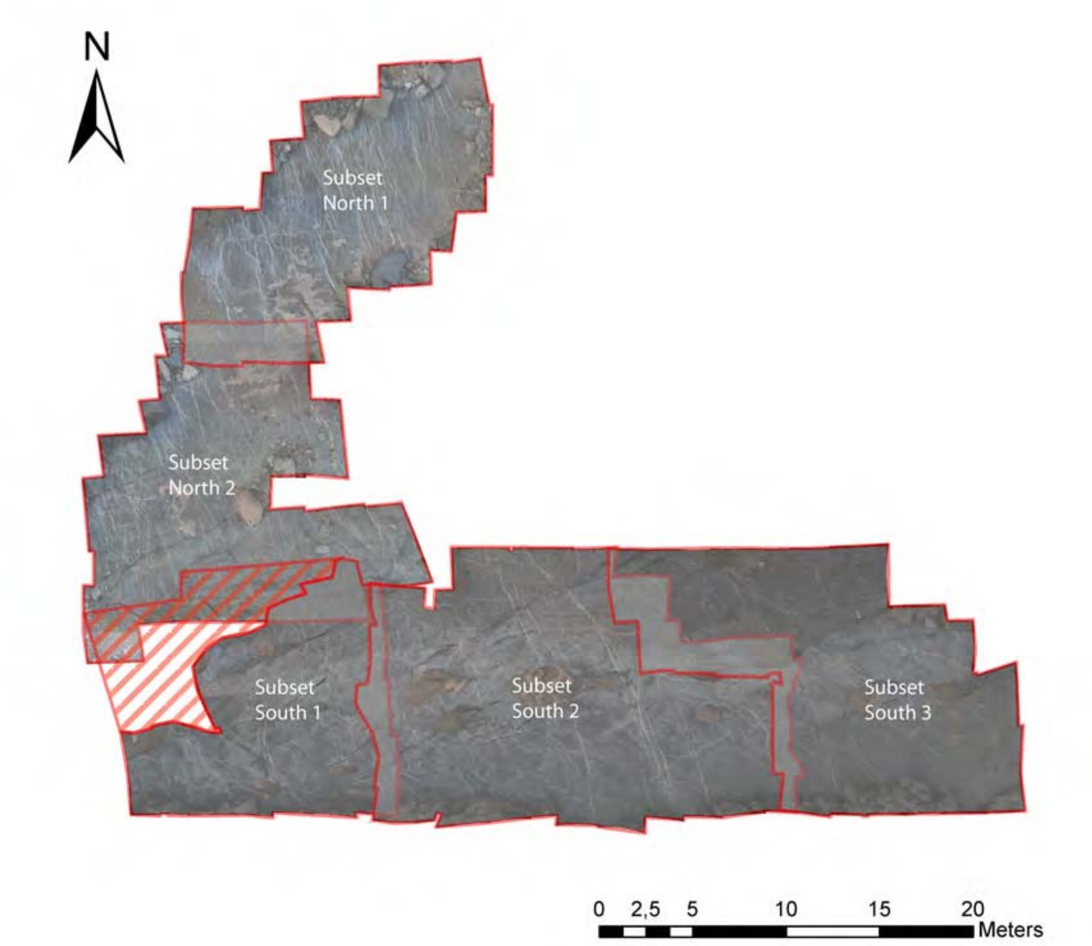

Figure 13: Overview picture of the outcrop photo mosaic. The extend of each subset is outlined with a red frame. The clipped area of subset South 2 is indicated with red shading. Subset North 1 consists of 38 tiles, North 2 consists of 32 tiles. The southern Subsets are made up of 31 tiles (South 1), 55 tiles (South 2) and 35 tiles (South 3).

2.1.6.3 **Automatic Panorama detections**

Once the tiles are loaded into the program, the automatic Panorama detection is started to identify overlaps in the pictures and reassemble them to panoramas. Several options are available to optimize the automatic detection to the particular requirements.

For our panoramas we achieved the best results by choosing the highest detection quality and limiting the number of control points to 50 for each image pair.

In the process of the automatic panorama detection also the radial lens distortion is removed. The required information like focal length and lens type are automatically read from each image's meta data.

On an modern desktop PC the panorama detection may take up to several minutes of processing time, depending on settings and number of input pictures.

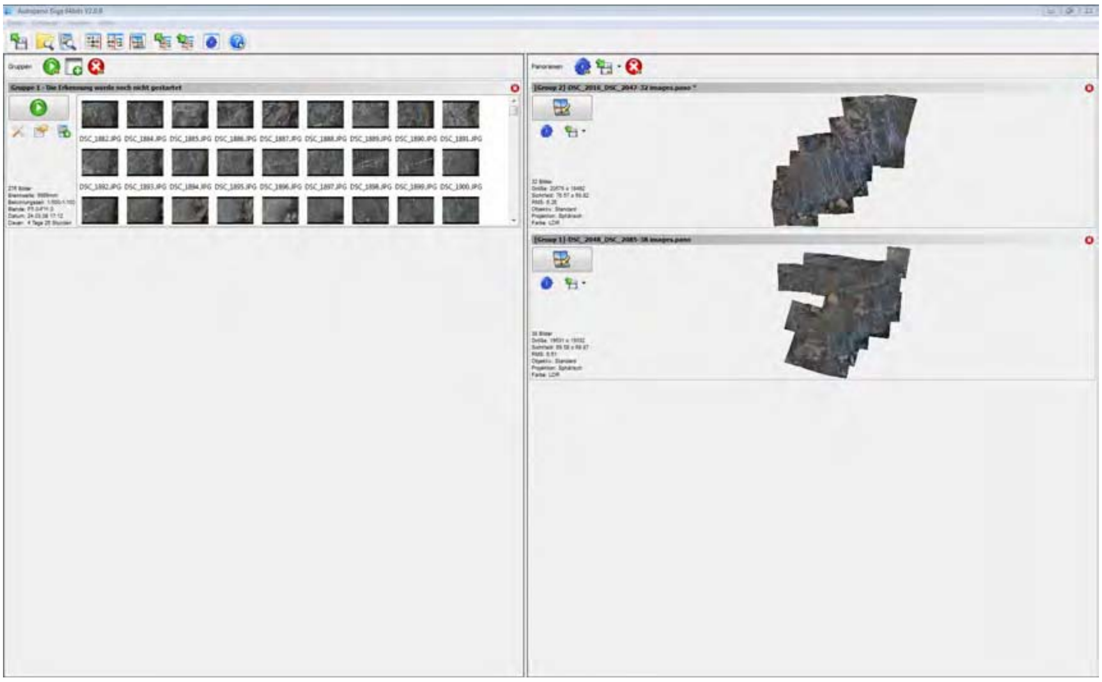

Figure 14: Screenshot of the Autopano Giga main screen (Kolor). The left column shows the input pictures. In the right column the detected panoramas are displayed.

2.1.6.4 Adjusting control points and optimization

After the detection module of Autopano Giga 2 has assembled one or more panoramas from the input images, the user has the opportunity to manually improve the outcome using the editing mode before the panorama is rendered (AutopanoWiki 2009a).

In the editing mode a preview of the panorama is displayed with a limited resolution. Furthermore the picture IDs of the tiles and all detected links together with their root mean square (RMS) error can be overlain.

The root mean square error is a value that describes the quality of the detected panorama. It is calculated for every link. It is the root of the mean of the squares of the relative deviation in position of the control points in the adjacent pictures. A high RMS value means that the pictures do not fit well together. The lower the RMS is, the better is the fit.

Double clicking onto a link opens the control point editor. The control point editor shows the two involved pictures of the link side by side at full resolution and the detected control points, color coded by their contribution to the local RMS error.

The control points of links with a very high RMS are usually located close to topographic features, for example within depressions or at topographic steps. In the control point editor these points can be deleted and new control points can be added to overlapping parts of the pictures where the topography is more flat.

After control points are deleted or added to the panorama, a global optimization process needs to be run that reassembles the pictures according to the changed control points in such a way that the RMS error of all control points the panorama is minimized.

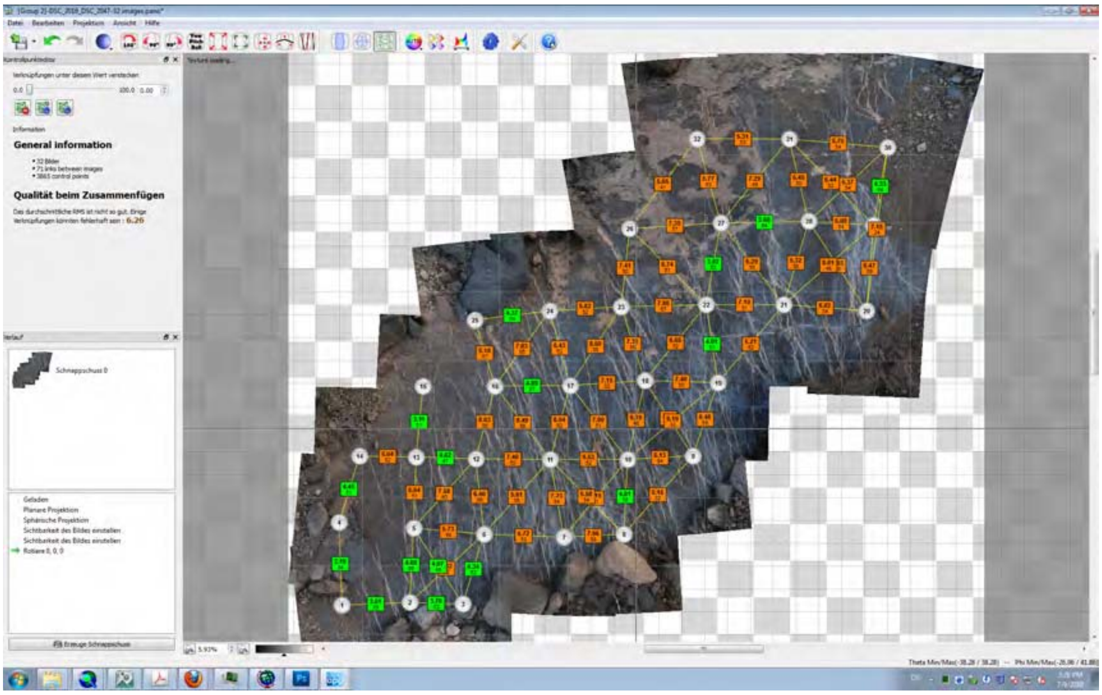

Figure 15: Screenshot of the Autopano Giga Editor window. A preview of the panorama is displayed at limited resolution. Numbers in grey circles are picture IDs; links are shown with yellow lines. The RMS value of each link is displayed in a color coded box. Green boxes indicate a low and orange boxes a higher RMS error of the link.

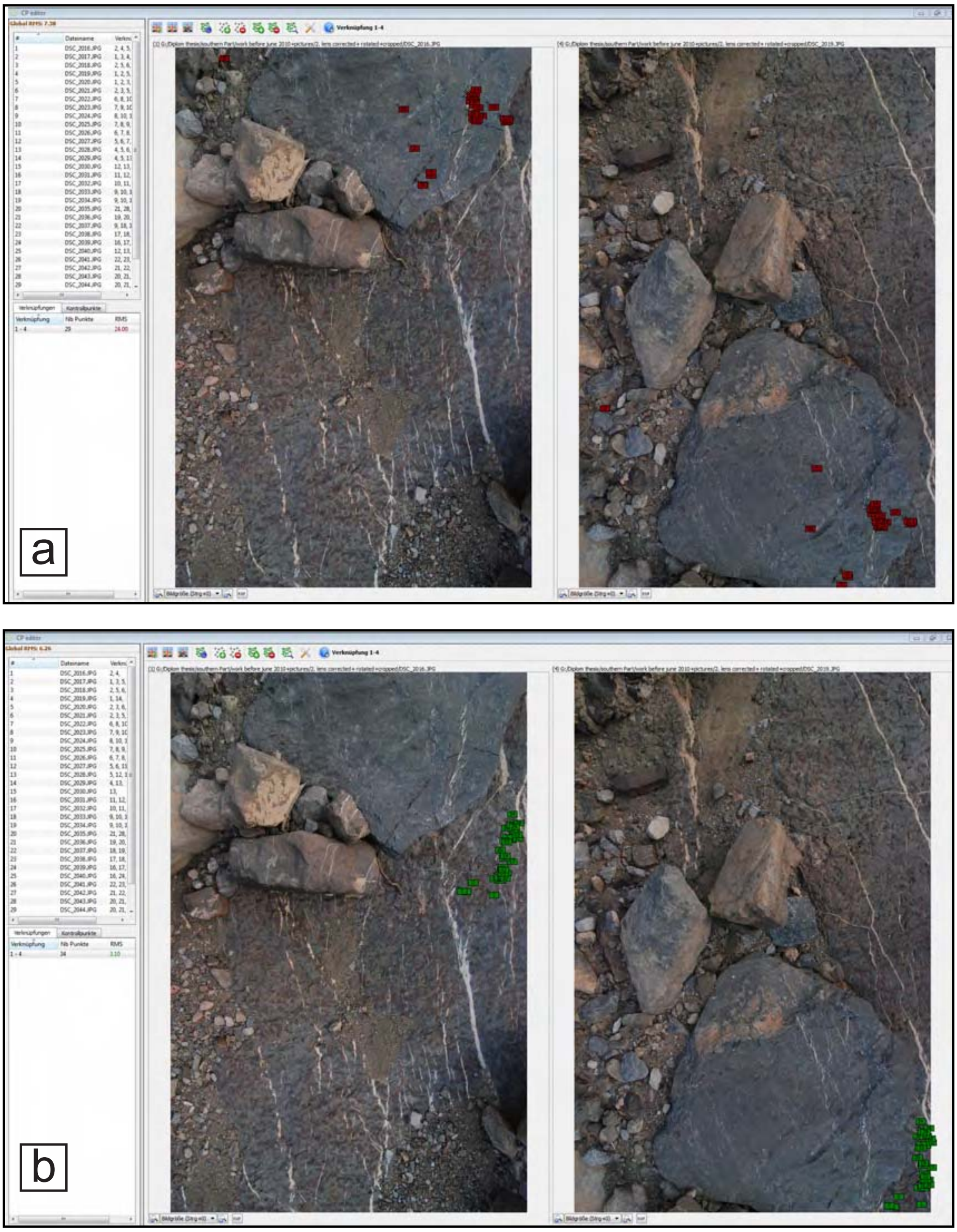

Figure 16: screenshots of the Control point editor . The linked pictures are displayed side by side together with the control points. To illustrate the effect of topography the control points in picture a are placed on a rock lying on the pavement. The control points do not match since the parallax error is high. Limiting the control points to the flat surface gives better results.

2.1.6.5 **Projection**

The software Autopano Giga 2 assumes that the tiles of any panorama are taken with a stationary camera. When the software assembles the tiles it therefore assigns them spherical coordinates on a hypothetical sphere around the shooting point.

The projection determines the way this sphere is "unwrapped" or in other words, how the texture of the sphere is displayed as a 2d image.

Since we moved our camera over the outcrop, and therefore the model of the sphere around the camera does not apply, any projection but the spherical projection would lead to strong distortion of our panorama (AutopanoWiki 2007).

2.1.6.6 **Blending**

The blender algorithm ("blender") is responsible for blending the image tiles in their overlapping area to make the transition zones of the pictures smooth.

4 different blender algorithms are available:

- None: The top picture is visible in the overlapping zone between the tiles. The image underneath is hidden. Blending is not performed. The seams of the tiles stay visible due to geometry, color or brightness contrasts
- Linear: the simplest and fastest blending algorithm: the opacity of the top image is reduced towards the edges of the tile. The tiles fade together in the transition zone
- Multiband: a more sophisticated algorithm than the linear blending, which adjusts the transparency of the top pictures based on the color changes of the overlapping pictures in the transition zone.
- Smartblend: additionally to a multiband analysis, a picture analysis engine identifies objects and common features in the overlapping area and creates a stitching seam based on this analysis. The smartblend algorithm can be very time consuming when applied to big datasets.

Two exigencies the blending algorithm has to meet:

1) The features in the transition zone must remain distinct, i.e. the veins must blur or get ambiguous interfaces.

2) Offsets of veins due to the inevitable parallax effects must be minimized.

For this reasons the smartblend algorithm was chosen. The decision what parts of which tile is visible in the end at what place in the overlapping area is based on a picture analysis and not predefined by the stacking order of the tiles. Furthermore it does not produce blurring, so that the contrast of veins towards hostrock stays sharp (AutopanoWiki 2008).

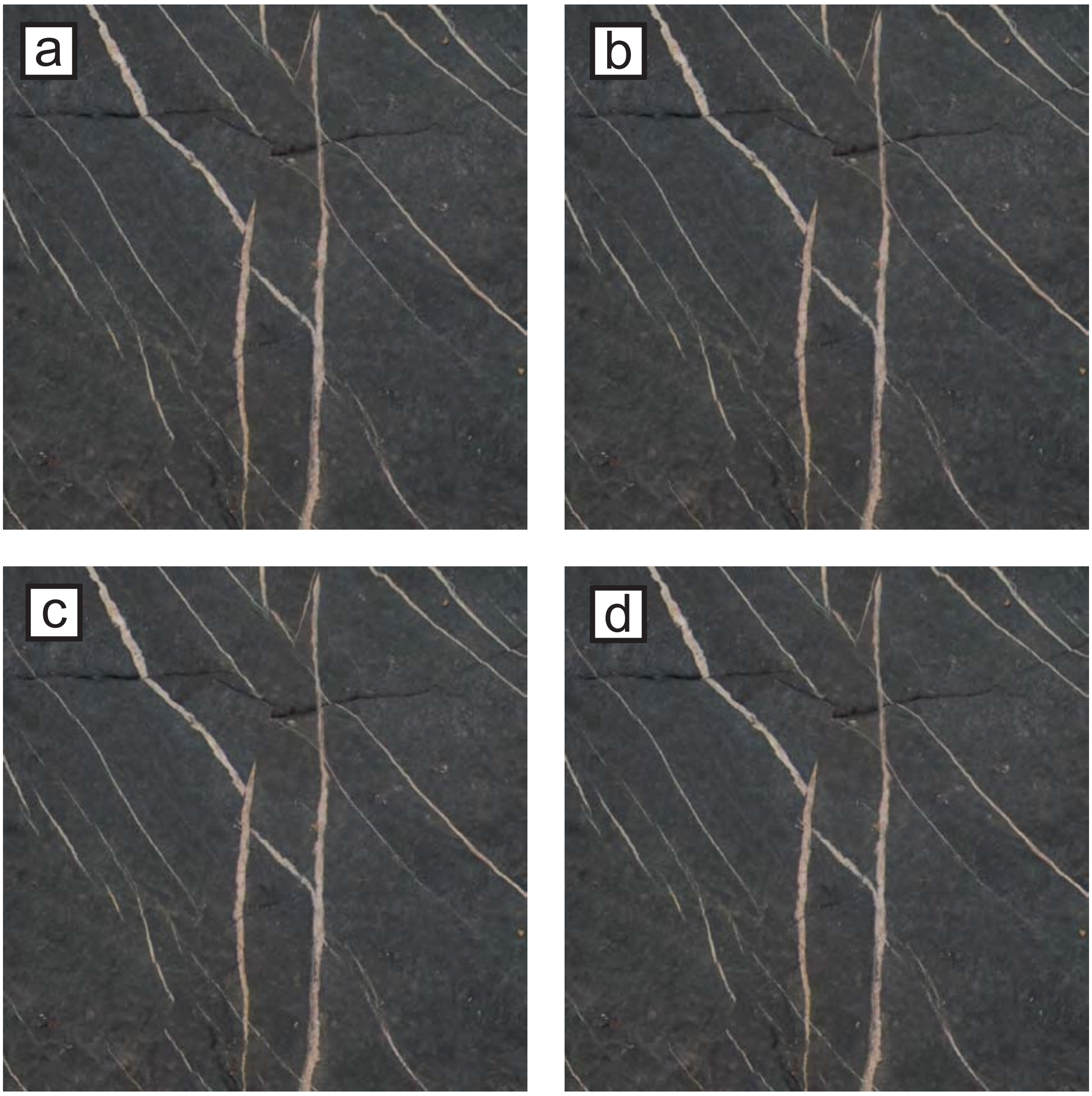

Figure 17: An 80cm x80 cm excerpt from the panorama rendered with no blending (a), linear blender (b), multiband blender (c) and smartblend (d). In the sample region 4 image tiles overlap and the local RMS of the links is high due to an adjacent topographic step. Without using a blender only the two uppermost pictures appear in the excerpt. The linear and multiband blender both produce semi transparent "ghost veins" and uncertain vein courses. With smartblend all veins are consistent and displayed without blurring.

2.1.6.7 Rendering and data format limitations

During the rendering process, the distortion, interpolation and blending of the tiles are performed at maximum resolution and the panorama is finally written into a single file (AutopanoWiki 2009b). The rendering is the most time expensive operation in the panorama creation workflow and may take up to several hours.

The created Panorama subsets have a resolution of several hundred megapixels., which is close to the limit of some image file formats:

Jpeg images can in theory be as large as 64.000 x 64.000 pixels. However, most software, including Photoshop and ArcMap are not able to open jpeg images where one side is larger than 30.000 pixels.

Tiff files have theoretically unlimited pixel resolution, but the file size is limited to 2 gigabyte.
If the panorama exceeds these values it is recommended to use PSB (Photoshop Big). This file format does not have a limitation in file size and can handle files as big as 90 gigapixel but can only be opened with Adobe Photoshop. Once this file is created it can be resampled or split up to match more compatible file formats.
Our subsets are chosen sufficiently small to fit into tiff files and could therefore be easily imported to ArcMap.

2.1.7 **Georeferencing**

To allow quantitative measurements in the panoramic picture, the datasets have to be fitted into a reference frame providing scale and direction. The referencing is performed in ESRI ArcMap 9.3 (ESRI 2004).

2.1.7.1 **Relative spatial referencing**

Relative referencing gives the dataset a dimension and an orientation but contains no information about its location. This means that features within the dataset can be spatially related to each other, but not to features from outside the dataset.
For this purpose a Cartesian coordinate system was established in ArcMap with the ordinate In N-S direction and the abscissa in E-W direction.
All marked grid points on the outcrop where then referenced to the coordinate system before the panoramas were distorted with a spline algorithm and saved.
We are not able to quantify the topography related error in the panoramas, so grid points are the only features of which we confidently know the location. Spline deformation moves these features exactly to their assigned position by deforming the image according to the principle of minimal surface curvature.

2.1.7.2 **Absolute referencing using high resolution satellite imagery**

Absolute referencing fits the datasets into a global spatial context. We performed absolute referencing based on an orthorectified and pan sharpened GeoEye satellite image with a panchromatic resolution of 41cm (GeoEye 2009). Unfortunately, due to the big contrast in resolution, only a few features from the panorama could be identified on the satellite imagery. The rectified datasets, which were produced this way, can be used for qualitative visualization, but is insufficiently accurate for quantitative measurements.

2.1.8 **Visualization for web interface**

For fast visualization and web presentation we exported our georeferenced panora-

mas as a zoomify image. Zoomify Expressä is a free software that creates several downscaled images of the input image (pyramids) and divides those together with the full resolution image into 256x256 pixel tiles (Zoomify).
A flash script embedded in HTML arranges and displays the tiles, allowing panning and zooming of the picture in a web browser with very little loading time.
A sample for the web Interface is available at http://www-users.rwth-aachen.de/max.arndt/JabalShamsMerge.htm .

2.2 **Macroscopic Age relationship determination**

182 relative vein age relationship observations were made at 90 locations throughout the outcrop. Age relationships were only recorded at locations where at least one unambiguous criterion for the chronological order was present (Chapter 2.2.1.). Drill plugs were taken at some intersections, where the age relationship of the veins was not clear in order to clarify them afterwards using microstructural investigation methods.

2.2.1 **Criteria for temporal relations**

Unambiguous criteria for the determination of the relative age of veins at outcrop scale are either offset or clearly distinguishable cements at vein intersections. Offset can be either real shear offset at mixed mode veins (Figure 18 b) or offset at a pure dilating vein that crosscuts an older vein at an acute angle (Figure vein 18 a).
The cement of the veins was only regarded as a criteria if a distinct color and/or texture contrast was observable (Figure vein 18 c) and a mimic effect (Holland et al. 2009b) could be excluded.

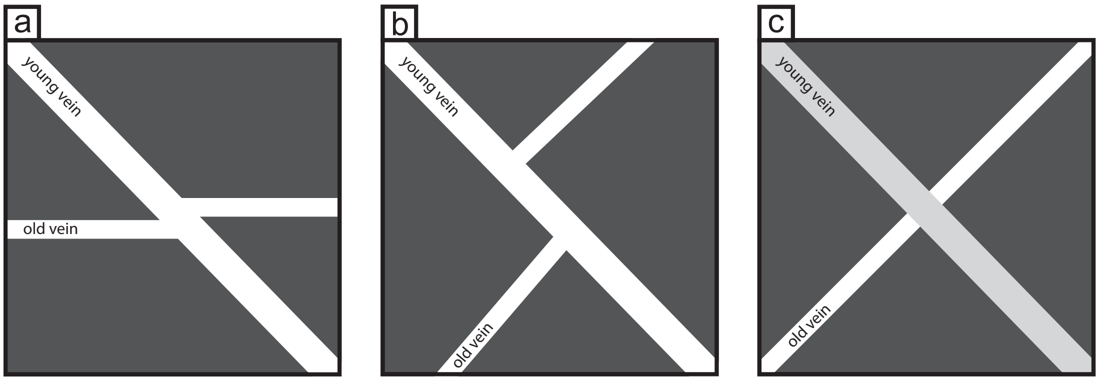

Figure 18: Criteria for the temporal relationships of veins can be either offset (a and b) or a heterogeneity in the vein fills (c). In (a) a younger vein that crosscuts an older vein at a high angle. Thus it shows no shear component, the older vein displaces the younger one by pure dilatational opening. (b) A younger veins displaces an older vein sinistrally. Since the veins are orthogonal to each other, the displacement has to be a shear displacement. (c) The temporal relation between the 2 veins can be established because the cement of the two veins is clearly distinguishable. The darker vein crosscuts the white vein and is therefore younger.

2.2.2 Chosen database attributes

Beyond measureable criteria each vein that was sampled or incorporated in an AR Observation was given attributes to characterize the vein in terms of its texture, geometry and appearance.

Quantitative attributes are:

- Length [cm]: the distance from one vein tip to the other along the vein
- Aperture [mm]: the amount of dilatational opening of the vein.
- Offset [mm], (sinistral or dextral): the amount of shear offset that the vein displaces an older vein with.
- Strike direction [°]

The non-quantitative attributes are:

- Color: overall color impression of the vein. Commonly white, grey or light brown (see Figure 19)
- Blocky: the calcite crystals show an equidimensional shape and grain sizes of at least several millimeters, so that crystal faces are visible with the naked eye.
- Flakes: The vein incorporates flakes of hostrock material visible with the naked eye.
- Brown stripes: elongated bodies of brown or reddish material occur in the vein OR the vein shows areas of brownish staining of the calcite (see Figure 20).
- straight: the vein shows no sinuosity at all and has straight contacts to the hostrock.

- curving: the vein shows a high sinuosity or significantly changes its strike direction.
- jumps: subparallel segments of a vein are connected by a segment with a comparable Aperture but a significantly different strike direction.
- Bundle: the whole vein is made up of several smaller veins with close spacing that intersect each other frequently.
- Splay: a vein (not a bundle!) splays up to several smaller veins and reunites.
- Tip splay: A vein splays up into several smaller veins at one or both of the vein tips.
- Stack: 2 or more veins align and remain parallel. The interface of the veins is still identifiable.
- Chainsaw: one or both vein walls show a chainsaw like zigzag pattern
- En-echelon (sinistral or dextral): the vein is part of a en-echelon set
- Hostrock bridges (sinistral or dextral): The vein is interrupted by sigmoidal hostrock bridges. In contrast to en-echelon veins, the strike direction of the set and the segments are the same.

The following figures are meant for illustrating the attributes. For more detailed observations refer to chapter 3.

Figure 19: A light brown vein with blocky calcite (•) crosscuts several older veins (e.g. ••) that belong to dextral en-echelon arrays. The naming of the veins is according to chapter 2.2.3. The observation ID (here: AR-086) and the strike directions of the veins of interests are written on the outcrop surface. Each picture contains either a compass or a North arrow card for scale and to show North direction.

Figure 20: vein •• shows a dextral offset of 40mm at the younger vein •. Brown stripes are visible in vein • at the bottom of the picture.

Figure 21: several parallel veins that crosscut and touch each other in numerous locations form a 173° striking bundle. The vein bundle also contains several host rock flakes.

Figure 22: In this age relationship observation, vein •• curves from an East-West strike direction to 118° strike. It displaces the straight and white vein •••.

Figure 23: Vein • shows "jumps" to the right at several locations and proceeds parallel to the initial strike direction after every jump. In contrast to dilatant jogs the aperture of the vein does not change significantly in between the segments.

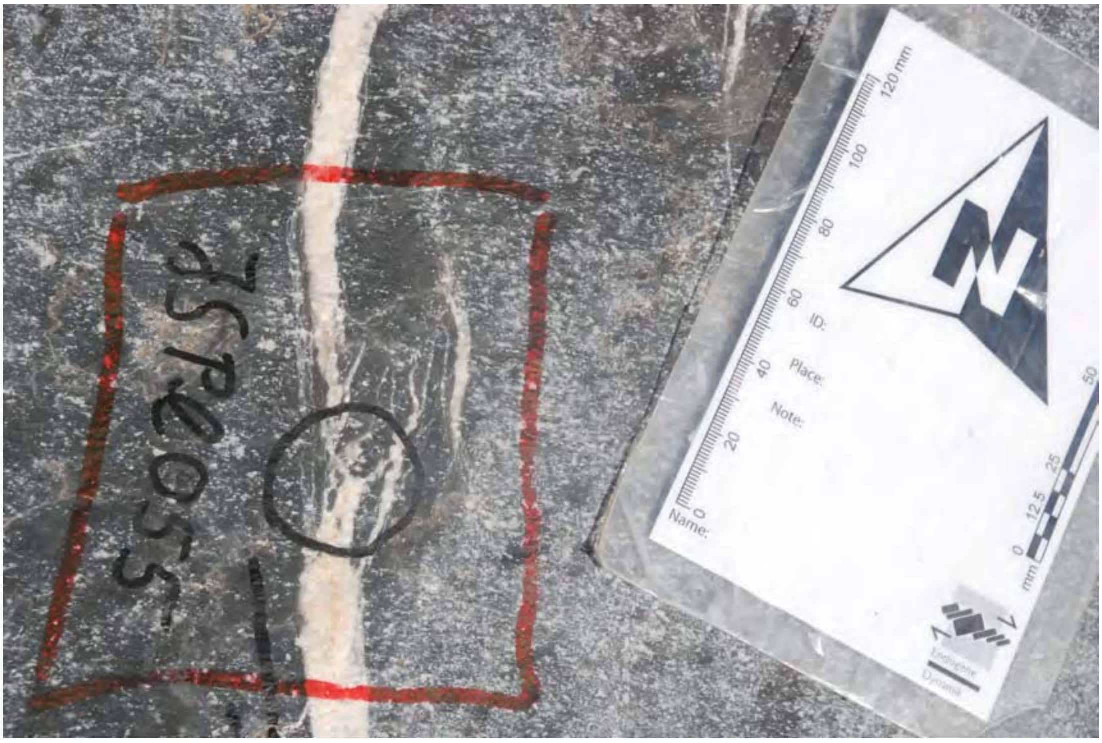

Figure 24: example for a splay within a vein. The vein splits up into several smaller veins but then proceeds with unchanged aperture and strike direction (here: 10 mm, 156°). Splays in which veins terminate are called tip splays.

Figure 25: a North south striking vein aligns a 131° striking vein, forming a stack of veins. The aperture of the stack is approximately the sum of the aperture of the single veins and the boundary between the veins stays distinguishable in the stack.

Figure 26: the highly lobate shape of the southern vein/host rock interface of this 125° striking vein gives it the attribute of a "chainsaw" vein. In this case only one wall of the vein shows a chainsaw pattern. At some veins it also appears on both vein/host rock interfaces.

2.2.3 **Nomenclature (point system)**

All age relationship observations were documented with one or more photos. The relative timing of the involved veins is not always obvious in the outcrop and occasionally not determinable on the photos.

The nomenclature of the veins in each Age relationship observation was therefore based on their relative age: the youngest vein was marked with one dot (•), the next older vein with two dots (••), and so on.

Every photo also contains the Observation/location ID (JS-AR-001 – JS-AR-90) so that every vein on a photo is directly identifiable in the dataset.

2.3 Rock sampling

110 rock samples were taken for microstructural and geochemical analysis.

Taking well-aimed samples from such a polished outcrop, without unproportionally destroying it, is only possible by drilling plugs out of the rock.

Our sampling setup consists of 3 parts: a drill, a power supply and a water-cooling unit.

The drill is a Bosch Power Tool (Type GSB 20-2 RE) equipped with a 35mm diamond impregnated hollow drill bit. A hand pump provides cooling water over an adaptor directly into the inside of the hollow drill bit at a constant rate. Besides the cooling, the water is necessary to wash away the crushed material so that the hollow drill does not get stuck.

A Honda 2000 Watt inverter Generator powers the setup.

A two man crew is able to operate the Rock sampling setup. However it is too unwieldy for hikes or difficult terrain and a source for cooling water should be nearby.

Figure 27: Taking rock plugs from the outcrop: One person operates the drilling machine while the other maintains a steady flow of cooling water with the pump. The generator in the background provides the electricity.

Figure 28: 110 Rock plugs and several hand pieces are prepared for their journey to Germany.

2.4 **Thin section preparation**

110 Thin sections were manufactured from the drill plugs to microstructurally investigate the sampled veins.

The thin section preparation were prepared following this workflow:

1. Determination of the thin section plane. All sections were prepared parallel to bedding.
2. Formatting of the plugs. The samples are cut to fit the object plate
3. The lower side of the section is polished with silicon carbide powder of decreasing grain size (320, 500, 800, 1200 grit) dispersed in a lubricant.
4. The section is glued onto the object plate with an epoxy resin and cut at a thickness of approximately 0,5mm.
5. The section is ground down with a cup wheel.
6. An Identification number and the North arrow are engraved into the object plate
7. The top of the section is polished with silicon carbide powder according to step 3 down to a thickness of ~30µm (or thinner). The thickness of the thin section is checked via the interference color of the calcite.

2.5 **Stable isotope measurements**

2.5.1 **Mass spectrometer and Kiel device**

The stable isotope measurements were carried out in December 2009 at the Research School of Earth Sciences at ANU Canberra. The device used for measuring the Carbon isotope ratios and Oxygen isotope ratios was a Finnigan MAT251 mass spectrometer attached to a carbonate reaction chamber (KIEL Device).

Figure 29: Photo of the mass spectrometer lab. The Kiel device is located in the left of the picture. The electronics of the mass spectrometer are located in the cabinet on the right. You can see the mass spectrometer in the middle of the photo. (Photo courtesy: Paul Stenhouse)

In the Kiel carbonate device, the samples react one at a time with 105% phosphoric acid at a temperature of 90° C for 13 minutes. The gaseous reaction products are transferred to the Mass spectrometer, where they are analyzed. After several corrections according to the method of Santrock (Santrock et al. 1985) and normalization to the standards NBS-18 and NBS-19 (Friedman et al. 1982), the Isotope ratios are presented in δ 18O PDB and δ 13C PDB (Cali 1997). To maintain comparability with previous work we converted δ 18O PDB to δ 18O SMOW by using the following conversion after Coplen (1988) :

$$\delta^{18}O_{SMOW} = 1,03091 * \delta^{18}O_{PDB} + 30,91$$

2.5.1.1 **Sample preparation**

The material for the stable isotope analysis is taken from 1mm – 3mm thick slivers of the drill plugs. The slivers are cut from the face of the plug, which was used for the thin section, so that the sampling volume for isotope analysis can be related to an area on the corresponding thin section. After the crystals or fragments of host rock are broken out with a hammer and a small chisel, the exact location of each sample is marked on a printout of the thin section overview image. To avoid contamination, the workplace and the tools are cleaned with ethanol before the next sample is treated.

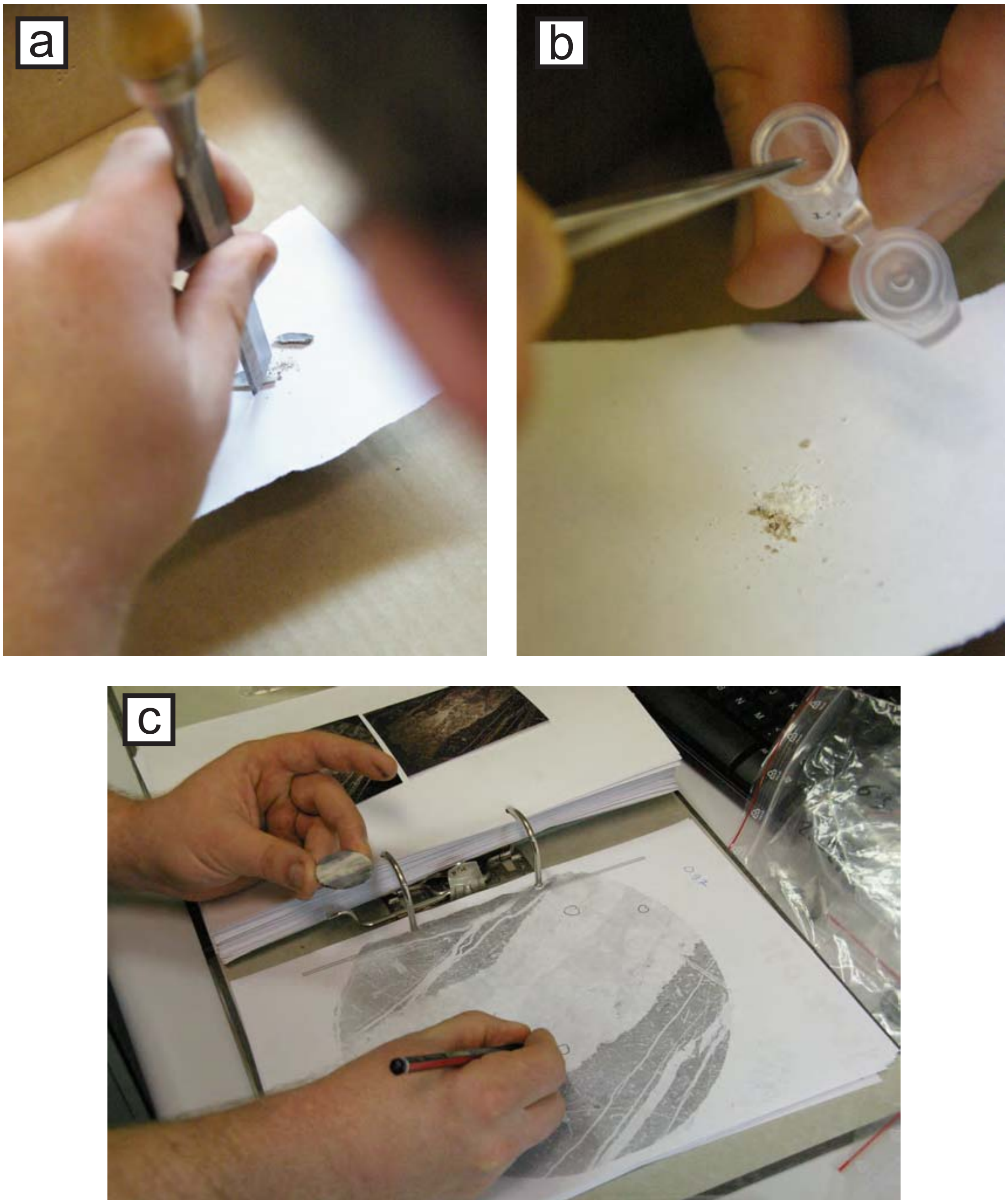

Figure 30: a) Material from the region of interest is carefully separated from the sliver with a broad bladed chisel and the put into sealable plastic containers (b). The exact area of the sampled region is documented on a large print out of the thin section (c).

After hand grinding the samples in an agate mortar, 200µg ± 20µg of the rock powder is weighed and put into thimbles for the reaction in the kiel device and the automated measurement.
After each grinding and weighing the tools as well as the workplace are cleaned with ethanol to avoid contamination. The prepared thimbles are stored in a container in an oven at 80º C to be protected against contamination by dust or moisture.

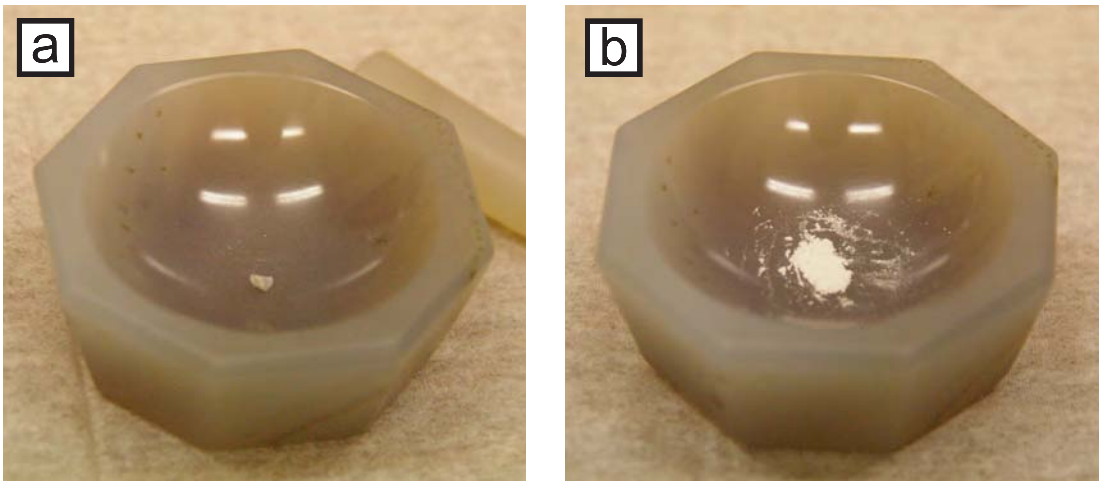

Figure 31: The samples are ground one by one to a fine powder with a carefully cleaned agate mortar. The finer the powder is grinded, the better it reacts with the phosphoric acid in the kiel device. Too small grain size however makes the weighing tedious.

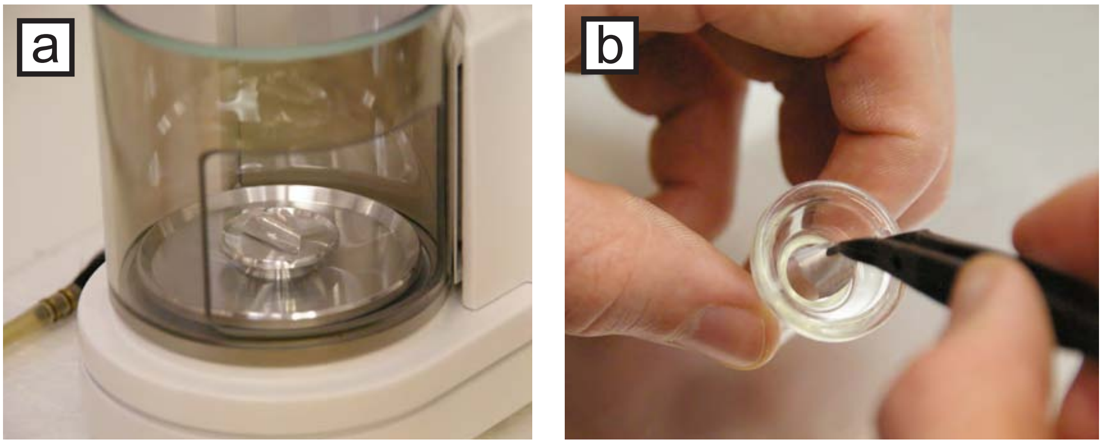

Figure 32: 200µg ± 20µg of each sample are weighed (a) and put into the reaction thimbles (b). Natural enemies of a weigher are vibration, air movement and static buildup.

2.5.1.2 **Measure procedure**

The thimbles that contain the sample material are loaded into a carousel that can than be placed in the kiel device. Depending on whether the kiel device is prepared for a day run or a night run the loading of the carousel differs:

For a day run it contains 6 samples as well as two NBS-19 standards. For a night run 20 samples, one NBS-18 and three NBS-19 are loaded. The ID of the samples as well as their exact weight is programmed into the run script and documented in the lab book.

Figure 33: Look into the Kiel device. The thimbles are placed in a carousel. For reaction and measurement they get picked up with a vacuum plunger. The Kiel device is partly located inside an oven that maintains a constant temperature of 90º C.

2.6 Integration of multi scale imagery and isotope geochemistry data

The referenced high-resolution imagery of the outcrop provides the base map to allocate observations made on outcrop scale and micro scale as well as the sampling spots for stable isotope measurements.

The dataset contains the following kinds of imagery:

- Detail photographs:

Photographs that were taken manually on the outcrop to document age relationship observations (79 images) and sampling sites (62 images). The resolution changes depending on focal length and distance to the surface. For Resolution bandwidth please refer to chapter 3.2.1

- Thin section overview images

Thin section overview images were taken with a digital camera from the screen of a Universalsichtgeraet after Kraus/Lanooy (Kraus 1988) which is able to display the full extent of a thin section in plane polarized and cross polarized light. The dataset comprises overview pictures of 80 thin sections, each in crossed polarized transmitted light and plane polarized transmitted light.

To bridge the gap in resolution, the detail images were rectified on the Panorama first. The detail photographs were usually adjusted to the panorama using the spline deformation to achieve a good fit. This is necessary since the detail images are usually not taken from the same direction as the panorama tiles, which produces a perspective distortion and a parallax error, depending on the deviation in shooting angle and the topography (see also chapter 2.1.5.1.3).

On the base of the rectified plug site detail photographs the thin section overview images can be located. The scale of the overview image is known, since the plug always has a diameter of 35mm. The micro scale images are rescaled and oriented with north up and then placed on the according position in the rectified detail image. Since they are taken from some cm depth, visible structures on the thin sections do not always perfectly match the visible structures on the outcrop surface.

The location of each individual stable isotope analysis was then marked on the according referenced thin section image (See chapter 2.5.1).

3 Observation and results (Max Arndt)

3.1 Gigapixel Outcrop Panorama

3.1.1 Resolution bandwidth and dimensions

The stitched outcrop panorama image provides the base map and a large amount of visual information at the same time with a NS – extent of 41.5 m while the EW extent is 50.5 m. The entire image consists of $1.21 \cdot 10^9$ pixels (see table subdivision resolution and stiching errors). The Outcrop Panorama is divided into northern and a southern domain. Both are each subdivided again (see figure 13 in chapter 2.1.6.2). Table subdivision resolution and stitching errors present which resolution and errors (RMS error, originating from stitching; see chapter 2.1.5.1) of the sub-sets. The reciprocal RMS-value aka stitching quality may drop at topographic features (please see chapter 2.1.5.1). According to the varying pixel resolution (pixel size) across the different subsets, the minimum thickness for identifiable veins changes. We were able to identify veins that have an aperture occupying at least two pixels. This is obviously dependent on image contrast and the shape of the vein-host rock interface. A sharp interface enhances the identification of veins, so does a good color contrast between vein cement and host rock.

sub-set	image size (pixel)	pixel size (mm)	RMS
North 1	20452 * 18421	0.90	6.26
North 2	19968 * 19038	1.13	6.69
South 1	10506 * 9618	1.59	9.64
South 2	20134 * 10543	1.46	10.36
South 3	12120 * 11442	1.93	8.09

Table 2: subdivision resolution and stitching errors

3.1.2 Distribution of observations

3.1.2.1 Vein overprinting

Figure 34 displays the distribution of age relationship investigation sites. Note the sites are well distributed over the entire area covering all parts of the outcrop and have been documented with detail photographs (see also chapter 2.6). Hence we regard the distribution as representative for the pavement with a high confidence. The criteria to determine vein-overprinting relationships at these sites have been explained in chapter 2.2.

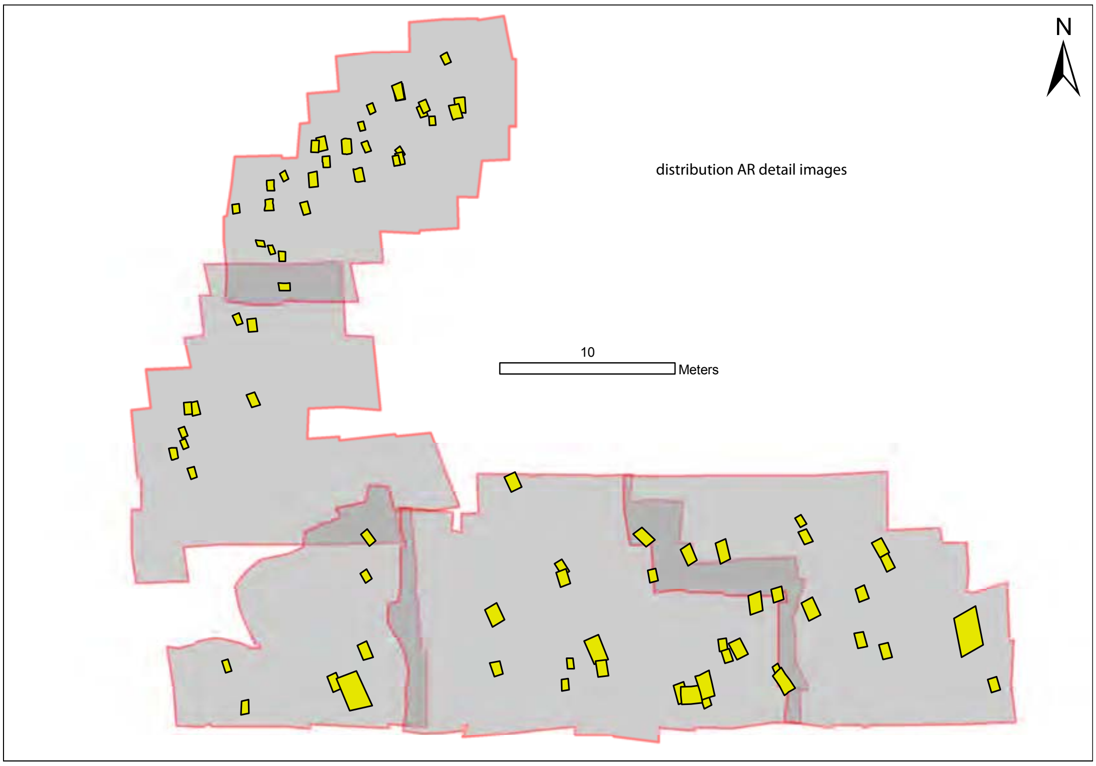

Figure 34: The figure displays the spatial distribution of detail images (yellow areas) that document a vein overprinting site. The outcrop panorama is grey outlined in red.

3.1.2.2 **Thin sections**

Microstructures have been investigated by transmitted light microscopy on thin sections that have been prepared parallel to bedding (chapter 2.4). On selected spots we took core samples from the outcrop. These sites have been chosen preferentially where calcite veins where visible. Hence the distribution of plug sites (core samples) is restricted to veins. Since we decided to differentiate between age relationship investigation, lateral vein investigation and special feature investigation, the distribution of microstructures aka thin sections is less good distributed as the age relationship investigation sites, but more concentrated on dedicated areas. Figure 35 shows the distribution of spots where core samples have been taken and thin sections have been prepared.

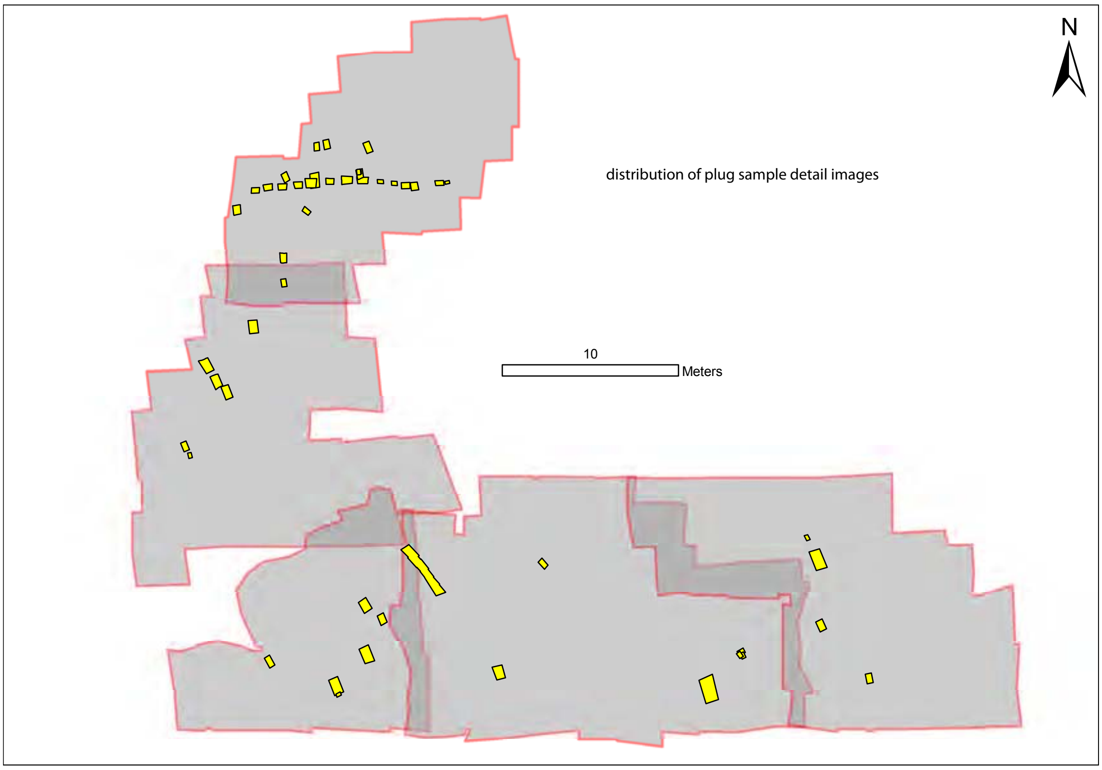

Figure 35: The figure displays the spatial distribution of taken plug samples and thin section locations respectively. The outcrop panorama is grey outlined in red. Each sample site (symbolized with yellow rectangles) has been documented with a detail image. These images have been rectified on the outcrop panorama. On these detail images we were able to allocate overview thin section images.

3.1.2.3 **Stable isotopes**

To measure stable isotopes of oxygen and carbon we took cut-off slices of the core samples (chapter 2.5.2) that were as close as possible with the thin section layer. By carefully separating crystal or host rock matter from the slices we were able to find the exact measurement location in the thin section. This enables a precise location of stable isotopes in selected thin section images, while the distribution of stable isotope measurements is restricted to core sample spots. We can present high-resolution data of over 100 measurements on a 40 by 50 meter outcrop (see figure 36).

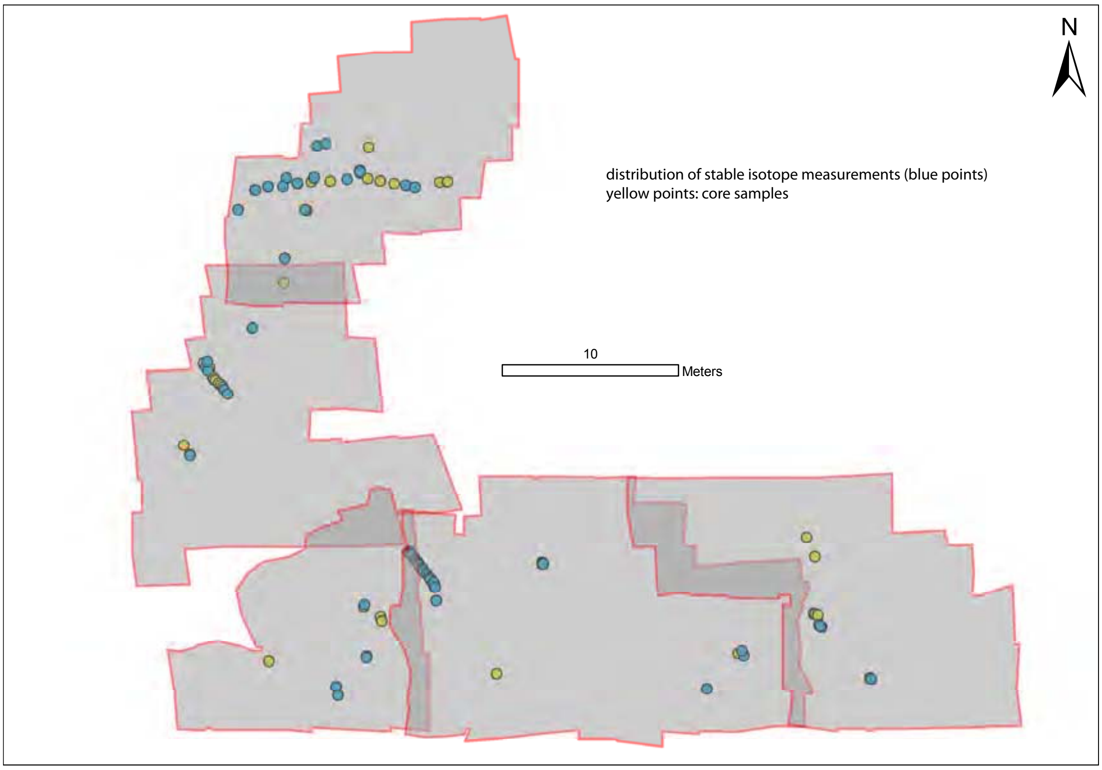

Figure 36: The figure displays the spatial distribution of stable isotope measurements (blue circles) that are confined to plug samples (yellow circles). The outcrop panorama is grey outlined in red. Each plug sample site been documented with a detail image. These images have been rectified on the outcrop panorama. On these detail images we have been able to rectify overview images of the thin sections. Stable isotope measurements are allocated at the accurate position on the thin sections overview image.

3.1.3 **Observable structures**

3.1.3.1 **Vein interaction**

3.1.3.1.1 **Bundles**

Bundles, meaning massive vein bands running sub-parallel along each other eventually cross cutting or aligning each other (anastomosing pattern) can be observed on the Mega stitch. Figure 37 shows two examples of vein bundles. Bundles are abundant on the northern part of the pavement, while the southern part mostly lacks bundles.

Figure 37: Scene from the outcrop panorama showing two bundles with an anastomosing pattern.

3.1.3.1.2 **Alignments**

Aligning veins is a common feature that can be observed on this scale. When a vein is suddenly deflected to another direction creating a Y-junction with another vein, we call it aligning. Other matching terms are bypassing (referred to highway junctions) or vein stacking (figure 38). Vein alignment can be observed on the entire outcrop.

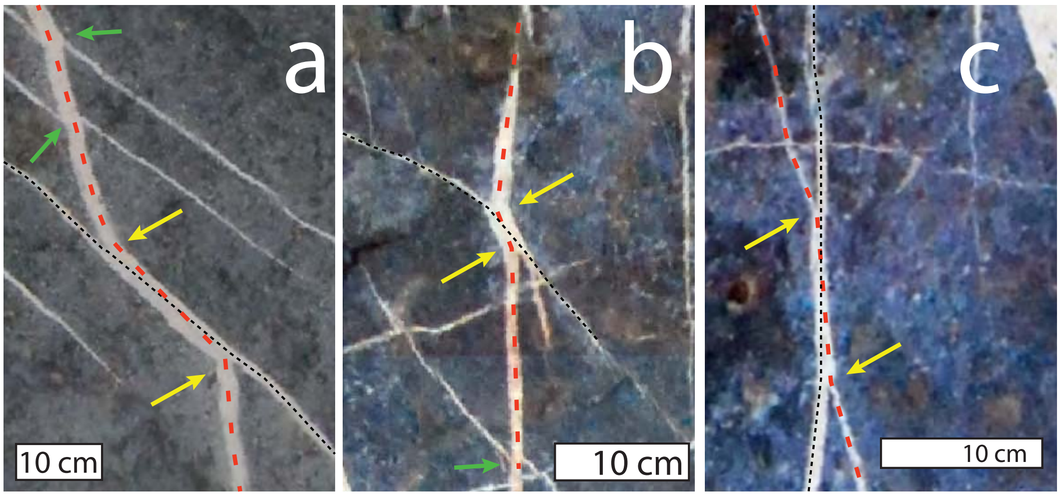

Figure 38: Examples of vein aligning. The figure shows scenes from the outcrop panorama. Image a shows a very nice example how a vein (traced with red dashed line) is deflected by another vein (black dashed line) and it's going back to its original course eventually. The deflection points are marked with yellow arrows. Note: the same aligning vein cross cuts other veins in the upper part of the image (green arrows). Though these are parallel to the black dashed vein and comparably thick, no aligning is visible. Image b shows an alignment of a relative thick vein with another but thinner vein. Deflection points are marked with yellow arrows. The same thick vein (red dashed) directly cross cuts a vein in the lower part of the image (green arrow). Image c shows another example for vein alignment. The red dashed vein is deflected by the black dashed one and joins its original strike eventually. Deflection points are marked with yellow arrows.

3.1.3.1.3 **Cross cuts**

The Mega stitch allows the investigation of sites, where veins cross cut each other. Examples are given in figure 39 (see also figure 38). Criteria to determine cross cut relationships has been defined in chapter 2.2.1. The most likely youngest vein (striking EW) in the northern part of the pavement shows both clear offsets and cross cuts without any offset. Orientation analysis of cross cut veins suggests an out-of-plane movement of this particular vein. It can be therefore classified as a shear vein, or incipient fault.

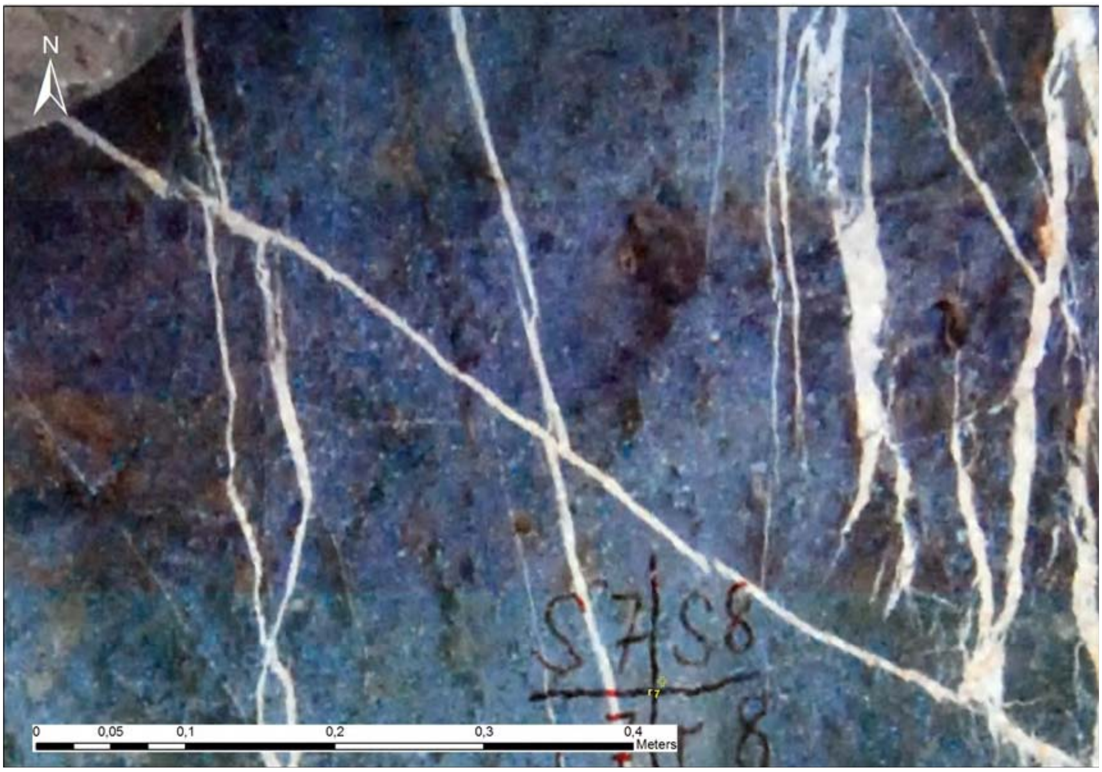

Figure 39: The figure is showing a scene from the outcrop panorama. One can easily identify a vein running from top left to the lower right corner. This vein is cross cutting other veins. Dextral offset indicates in plane movement.

3.1.3.2 Vein shape

One could assume veins being a tabular or lenticular shaped body showing a linear shaped outcrop disregarding it's cutting plane with the outcrop's surface. Some veins outcropping at the Discotheque pavement show a non-linear shaped outcrop with a certain sinuosity. We call these features curving however they may have formed. Figure 40 shows examples for non-linear shaped veins as they can be observed on the outcrop panorama. Note: we tried to make this classification for solitary veins. Hence this chapter is not concerned about vein shapes affected by mechanical anisotropies as other veins.

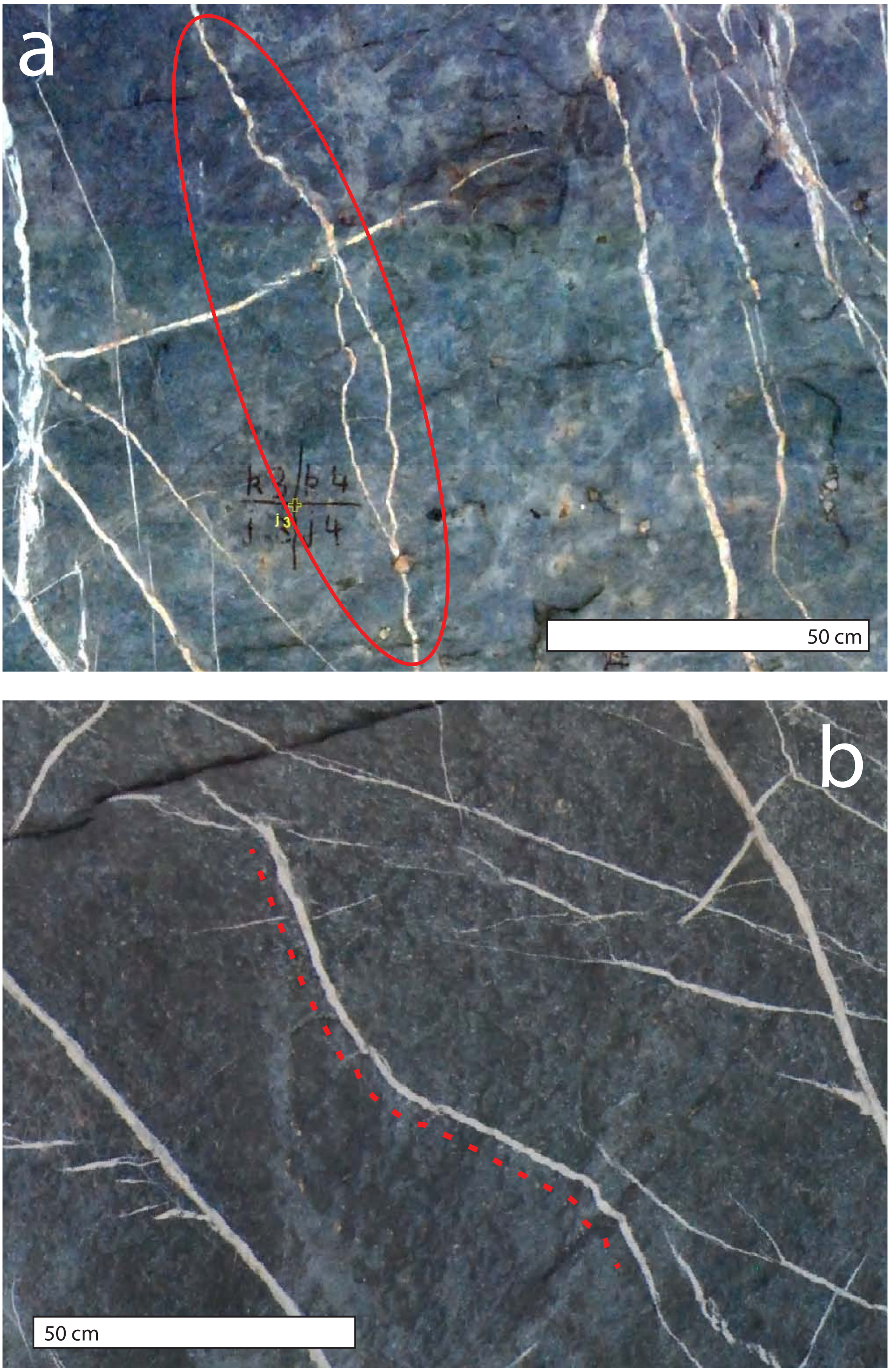

Figure 40: The figure presents two examples of a non-linear shaped vein. Image a shows a curving vein, that splits up in two still curved shaped veins and the reunion of both. Image b shows another example of a thicker vein that has a curved outcrop shape as well but not as sinuous (and a greater wavelength e.g. compared to aperture) as the one in image a.

3.1.3.3 **Major strike directions and vein sets**

By visual analysis we found three dominating strike directions (see figure 41). The first dominant strike direction is oriented around 160° (see green set in figure 41) and shows wide apertures regularly caused by stacking and refracturing. We found bundles with anastomosing patterns running along this strike as well. The second apparent set strikes along 117° being more isolated veins with thin apertures and a more linear course than set (1). The third prominent set shows a general strike around 83° with shorter length as both other sets and showing small apertures. Vein courses are also more linear than the first set. Note: from this visual analysis we were not able to establish a consistent relative age model. Please see chapter 3.2.3 for further details. The majority of the veins on the outcrop show a mode I mode opening (extensional fractures).

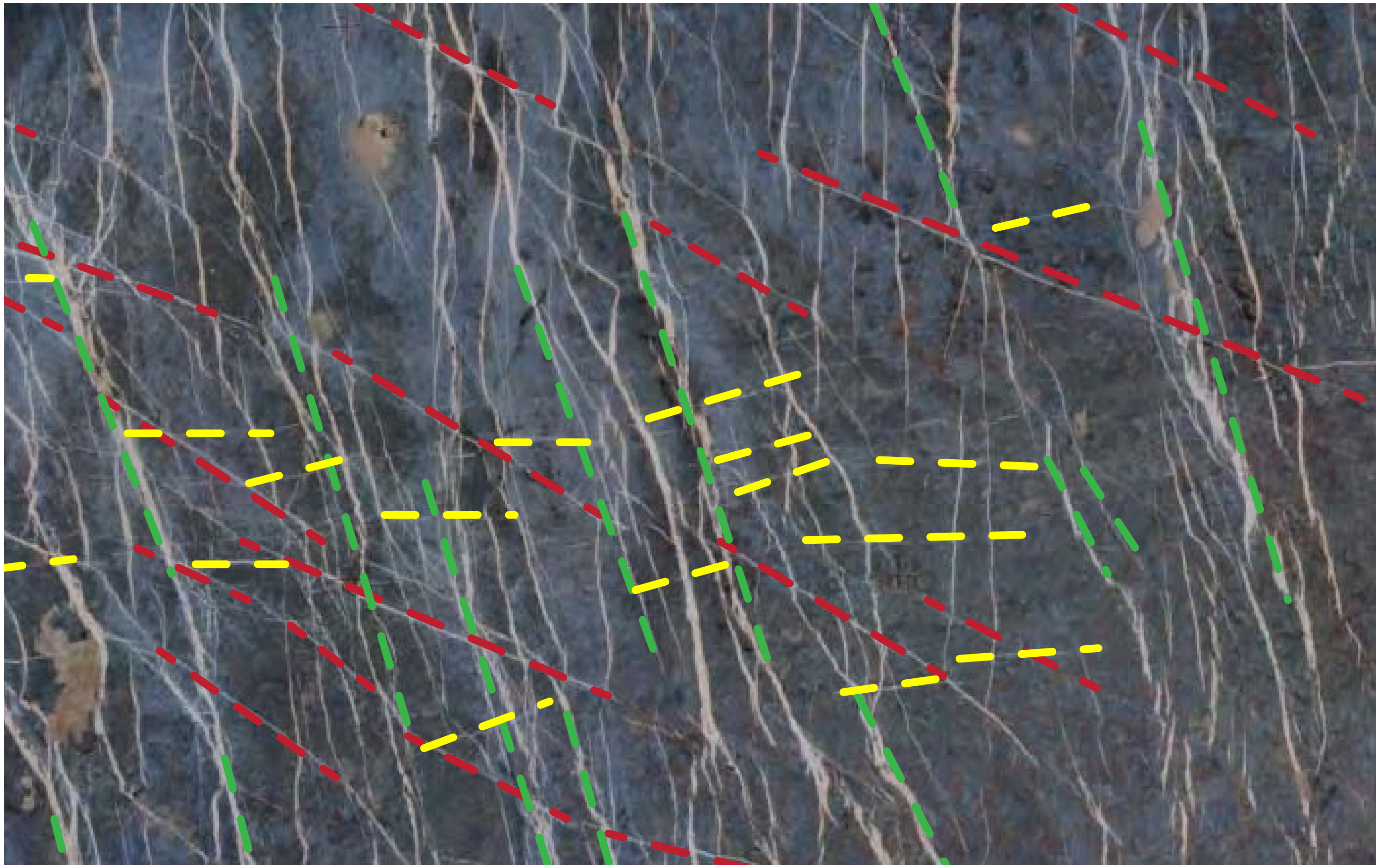

Sets (in ° CW from N)

(1)	(2)	(3)
117,7	157,6	93,2
112,2	158,3	94,1
120,7	158,1	90,5
117,7	163,4	83,1
117,5	162,7	90,0
121,2	164,3	75,6
120,6	165,5	90,0
104,4	165,8	90,0
117,5	154,0	90,0
127,6	160,4	76,8
126,1	162,3	92,4
113,0	152,6	73,5
110,7	152,3	75,0
115,2	146,5	72,0
123,3	162,9	88,7
116,7	158,0	74,3
109,3		84,5
114,6		82,5
		74,3
		70,0
		79,0
		93,5

159,04

Figure 41: representative visual analysis of a part of the outcrop panorama. We measured the bulk strike direction of three apparent sets. The average directions are show in the sketch in the lower right corner.

3.1.3.4 En echelon veins

En-echelon veins are prominent features mainly in the southern parts of the panorama. There exist at least one dextral and one sinistral set (figure en-echelons). Note: in the southern part of the panorama, topography has a strong influx on stitch quality. Please refer to methods chapter (2.1.5.1). The en echelon veins indicated a hybrid mode opening.

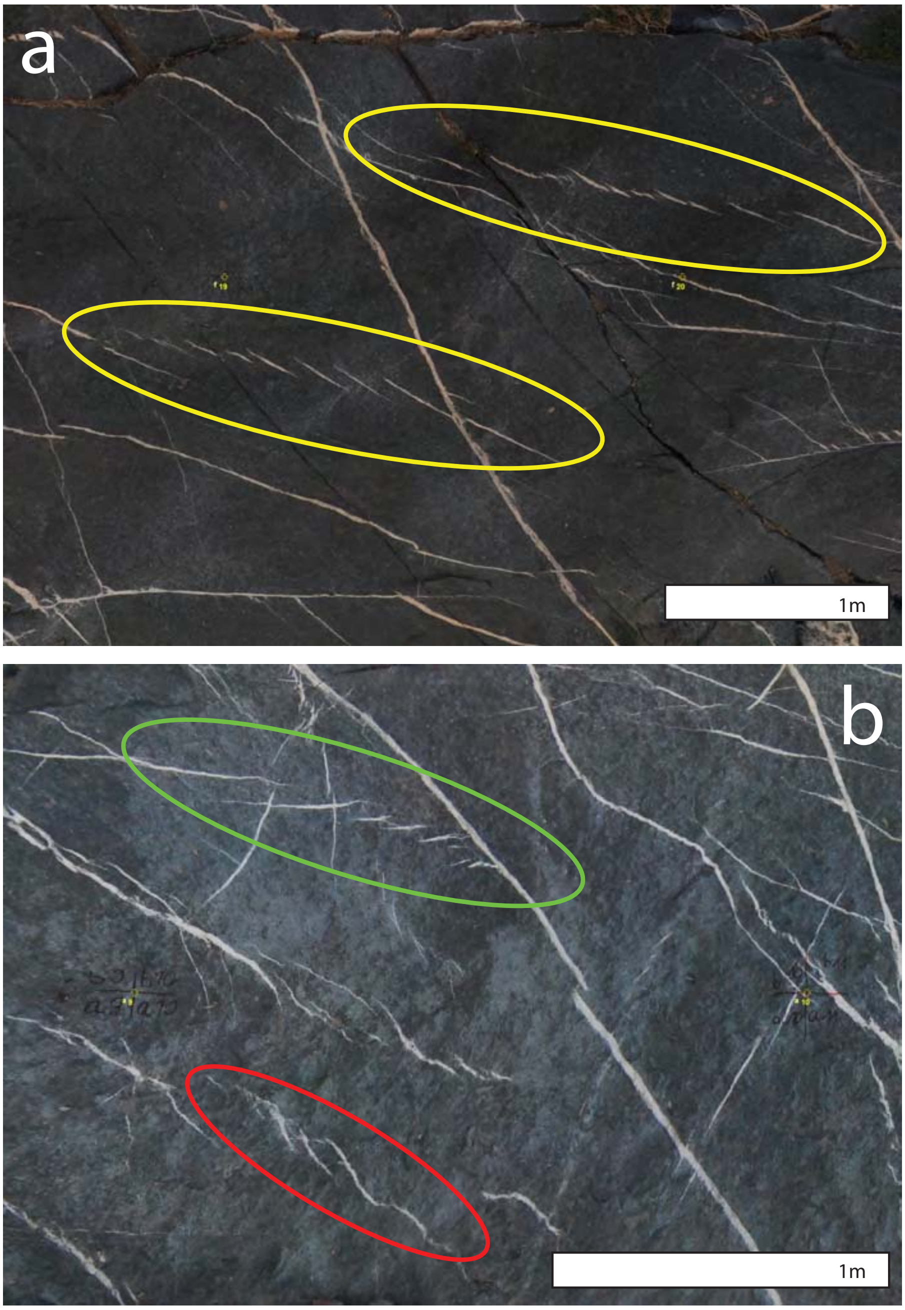

Figure 42: Figure is showing outcropping en echelon veins on the outcrop panorama. There exist at least one sinistral and one dextral set. Left stepping dextral set can bee seen in image a (yellow ellipses). Both one right stepping sinistral (green ellipse) and a left stepping dextral set (red ellipse) can be seen in image b.

3.2 Detail image scale

3.2.1 Resolution bandwidth and dimensions

We took numerous detail images to document structures, measurements and observations in detail. The photographs were taken to capture the object in question appropriately. Hence the capture angle and the distance to ground are varying from site to site. Hence image areas differ from 0.5 square meters and a pixel size of 0.28 mm to image sizes of 0.2 square meters where one pixel is 0.15mm wide. The first case means veins can be identified with a minimum aperture of 0.5 mm, while the letter case allows a identification with a minimum aperture of 0.3 mm. Both values depend strongly on image contrast. Note: the pixel resolution was measured after images have been adjusted and rectified to fit the Mega stitch base map.

3.2.2 Vein texture

The overall vein texture that has been observed at meso scale is blocky. We have not found any indicators for stretched crystals or even fibrous vein texture. In thick veins (aperture > 1 cm) single calcite crystals can be identified, due to their grain size.

Figure 43: The figure shows a planned plug samples site (JS-PL-064). The vein's texture can be roughly seen to appear blocky with grain sizes up to 1 mm.

3.2.3 Age relationships

Systematic notation of overprinting relationships with the defined criteria (see chapter 2.2.1) do not suggest a common relative order of vein sets. As one can see in figure 44 no vein strike direction can be found that is not overprinted by another vein strike direction. If so, than one would find a vein strike direction on the y-axis, where no data point matches its y-value. This would indicate that this strike direction is a candidate for being the youngest vein generation, if veins of this strike direction actually exist. However a lot of data points exist in the 80°-100° corridor of the x-axis crossing with the 150°-20° corridor on the y-axis. Nevertheless visualization of overprinting relationships suggest a mutual behavior.

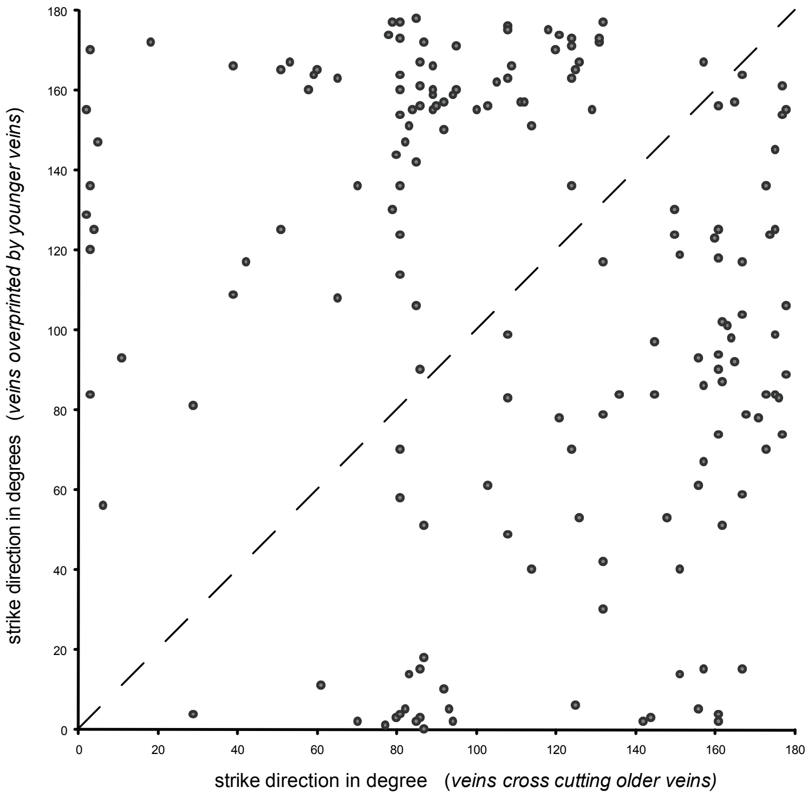

Figure 44: The upper image shows an example of an overprinting site, that was investigated. The notation has been explained in chapter 2.2. The lower plot presents the collected data from all investigation sites. Each point represents one overprinting relationship based on strike directions. Strike direction of the relative younger vein are noted on the horizontal axis, while strike directions for overprinted (relative older veins) are noted on the vertical axis.

3.2.4 **Chain saw structures**

The common understanding of opening of veins draws a clear picture about the shape of the vein-host rock interface. A peculiar structure dragged our attention to this matter. The so-called chainsaw structures, where the vein-host rock interface is showing an undulating or even fuzzy shape that does not match the opposite interface's shape can be identified on detail image scale. Figure 45 shows some example of these structures caused by the interference of stylolites with the vein.

Figure 45: The image shows a site of planned plug samples (JS-PL-031,32&33) to investigate the chainsaw structures visible on the detail image. The left vein-host rock interface is undulating while the right one does not show this behavior.

3.3 Microstructures

3.3.1 Resolution bandwidth

The majority of taken core samples where taken perpendicular to bedding and the diameter of the drill bit is 35mm. Hence the thin section's diameter matches 35 mm. After the images (overview images taken with Universalsichtgeraet after Lanooy & Kraus (Kraus 1988)) were adjusted and rectified by supporting detailed outcrop images the spatial resolution is 12 µm. Further microscopic imagery can be hanged in easily providing a spatial resolution according to the microscopes optical magnification (lens and ocular).

3.3.2 General carbonate rock classification

Following Dunham's classification for limestones (Dunham 1962) a general rock description would match the Wackestone type, since depositional texture is recognizable and original components are not bound together during deposition. The limestone is mud-supported (Micrite, grain size <20µm) with components more than 10%. Components are mostly Calcite and Quartz bearing fossils or fossil fragments. Bigger components are usually recrystallized (e.g. Aragonite → Calcite during diagenesis) with sparse Sparite (figure carbonate rock classification a). A detailed look on the components in the limestone host rock is beyond the scope of this thesis. A porosity was not recognizable under the microsope.

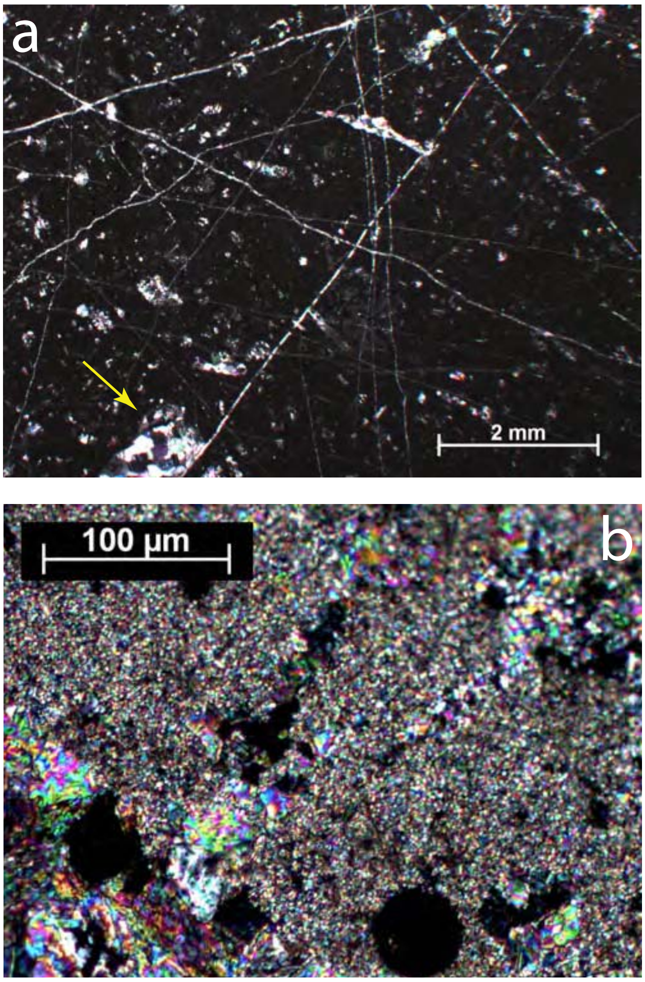

Figure 46: The limestones at the Discotheque pavement can be classified as Wackestone after Dunham (Dunham 1962). Image a shows a typical micrograph of the bulk limestone (sample JS-PL-003). The rock is mud supported, which is shown in detail on image b from sample JS-PL-035. A bulk mud (Micrite) grain size is less than 10 µm. Note the fossil in image (a) that is filled with sparse Sparite (yellow arrow). Both images are taken under crossed polarized light.

3.3.3 **Veins at microscopic scale**

We divided calcite veins at microscopic scale by their aperture:

(1) Thick veins (> 5mm) show a blocky texture showing mostly inequigranular polygonal grain aggregate shapes (figure 47). Most of theses veins do provide implications on their growth process (see chapter 3.3.5 crack-seal textures). Thick veins usually show an undulating or even fuzzy interface to the host rock that may due to interference with smaller (parallel) veins at the interface and/or crack sealing processes (chapter 3.3.5 crack-seal textures) as well as stylolite interaction (see chapter 3.3.9 stylolites and interaction with veins). The calcite veins contain minor amounts of Quartz.

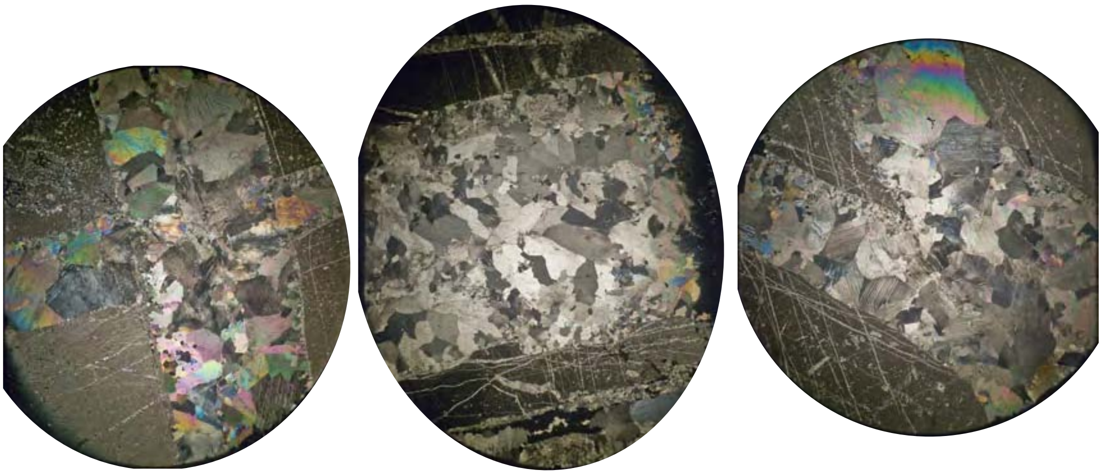

JS-PL-004 JS-PL-024 JS-PL-059

Figure 47: The figure presents 3 thin section overviews to emphasize the dimensions of thick veins at microscopic scale. Note the blocky texture showing mostly seriate polygonal grain aggregate shapes. All images were taken under crossed polarized light. Diameter of all images is 35mm.

(2) Intermediate veins (range: 100 µm – 2 mm) show an inequigranular polygonal grain aggregate shape (figure 48). Their host rock interfaces are usually sharp, if not affected by stylolithes. Veins of this aperture show in minor cases elongate crystal shapes (figure 48).

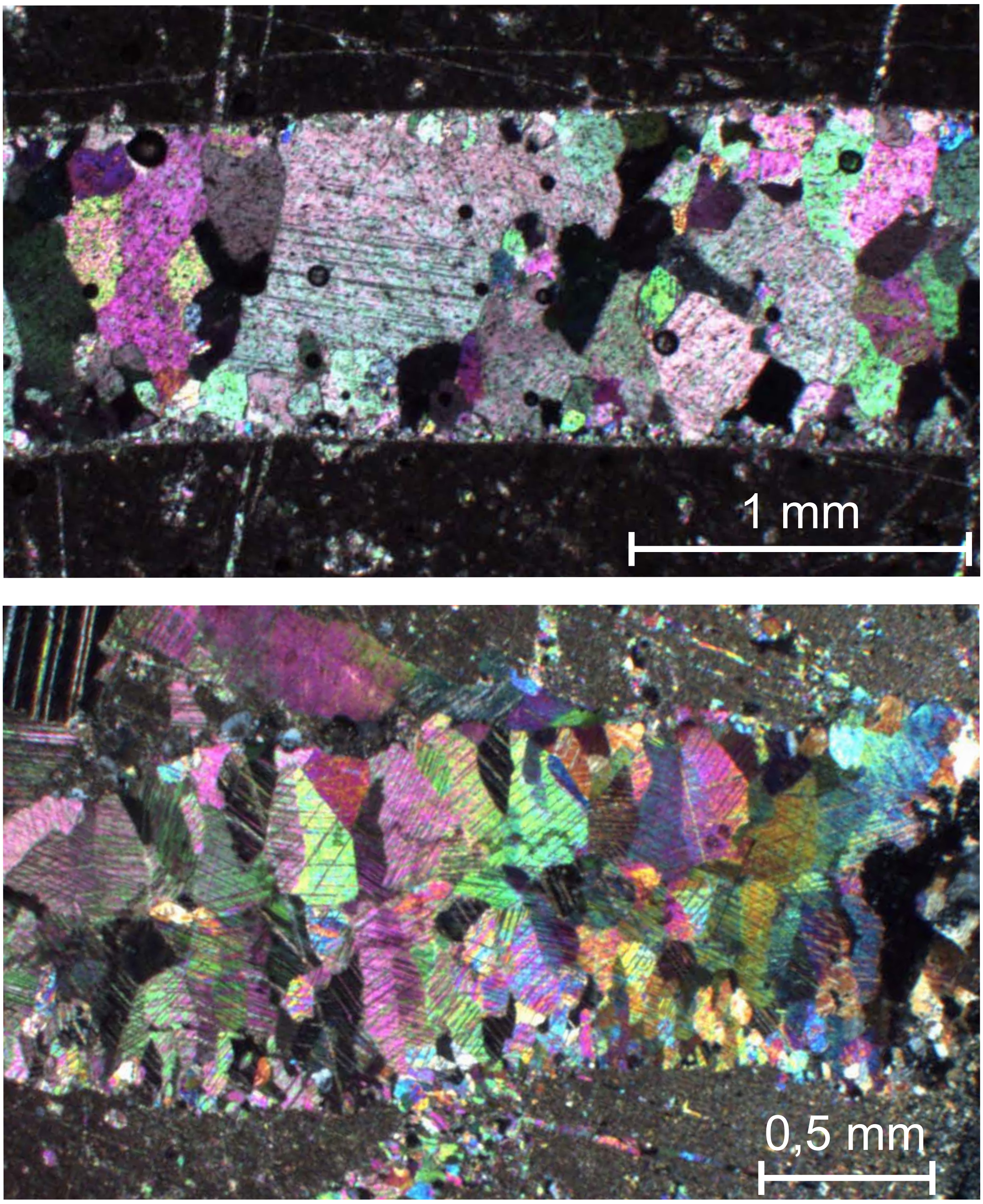

Figure 48: Typical intermediate vein, which can be observed at microscopic scale. The upper image shows a vein with an inequigranular polygonal grain aggregate. The vein texture can be described as blocky. The lower image presents an intermediate vein with a more equigranular polygonal grain aggregate. Crystals show elongated shapes.

(3) Veinlets (<100 µm) are usually showing very little information about their grain aggregate shape. If one structure can be found throughout the entire collection of thin sections, it is the presence of these micro veins. There is no single thin section without any micro vein. Even thin sections we have taken distal to macroscopic veins (intended to investigate the host rock's carbonate rock classification e.g. JS-PL-077) show plenty micro veins. Since we assume them to be ubiquitous (figure 49).

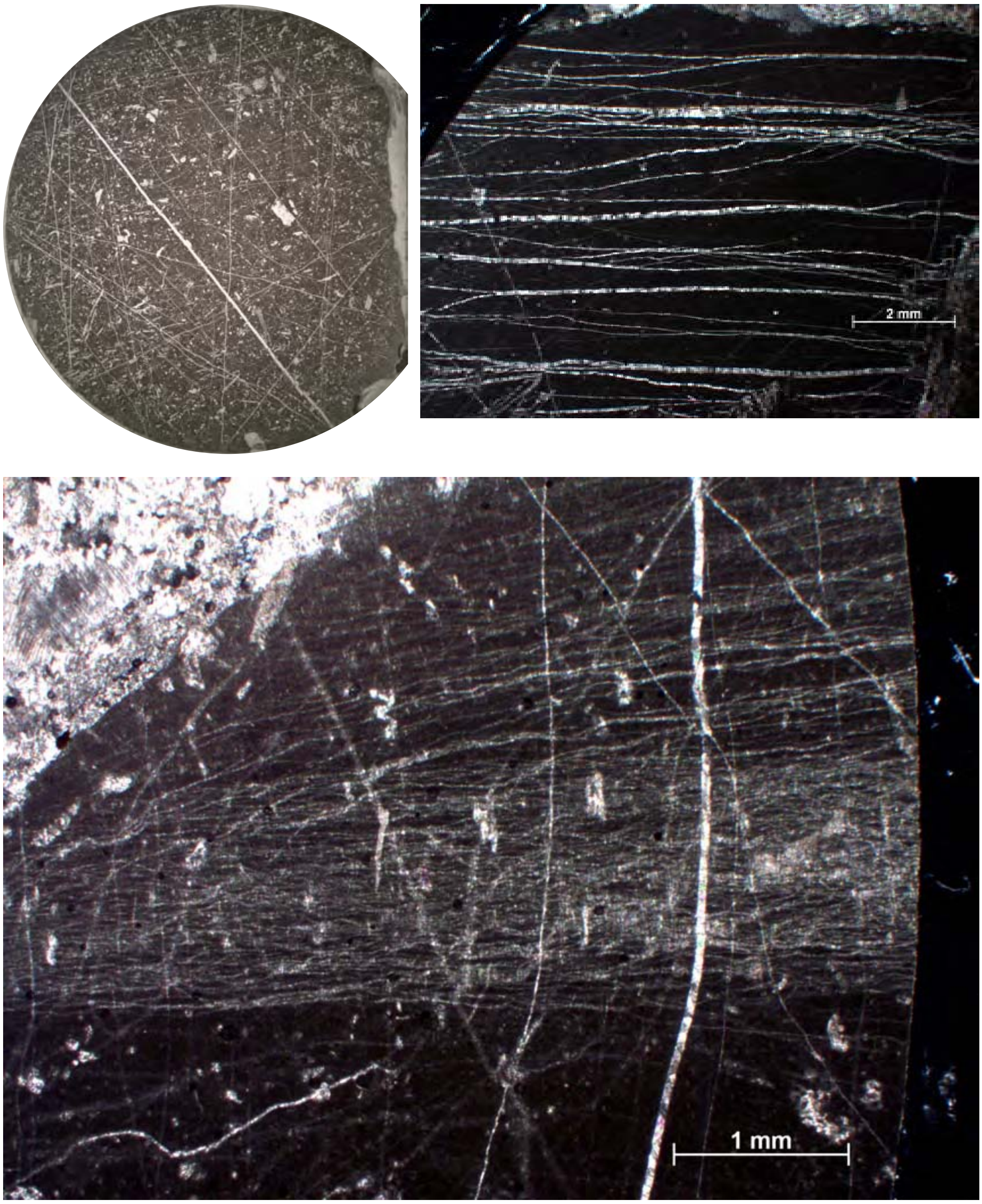

Figure 49: Top left: Overview image (plane polarized light, diameter: 35mm) of JS-PL-077. This sample was taken distal to macroscopic visible veins, but it still contains plenty veinlets. Top right: array of veinlets in sample JS-PL-081 (crossed polarized light). Bottom: Massive swarm of veinlets running from the left to the right in the image (crossed polarized light).

3.3.4 Veins overprinting veins

Cross cutting relationships are a difficult matter at microscopic scale. We have observed cross cutting veins that share the same crystals (figure 50). This matter of fact was also commonly observed if crystallized fossils are cut by veins: there is clear evidence that fossil crystals fossils started to grow again after they have been fractured (epitaxial growth, figure 50). In most cases, where we intentionally sampled to solve unclear overprinting relationships, there is no unambiguous solution. We observed cross cutting veins that show several phases of cracking and sealing (see chapter crack seal) that produced a pattern of cyclic overprinting. Identifying which vein part overprints another is even more difficult (e.g. JS-PL-009; figure 51).

As already mentioned in chapter 3.3.4 young veins (named juvenile) are oriented along the crystal lattices of existing calcite crystals. Since these have mostly developed deformation twins (chapter 3.3.4) the crack path is ladder-shaped (figure 52).

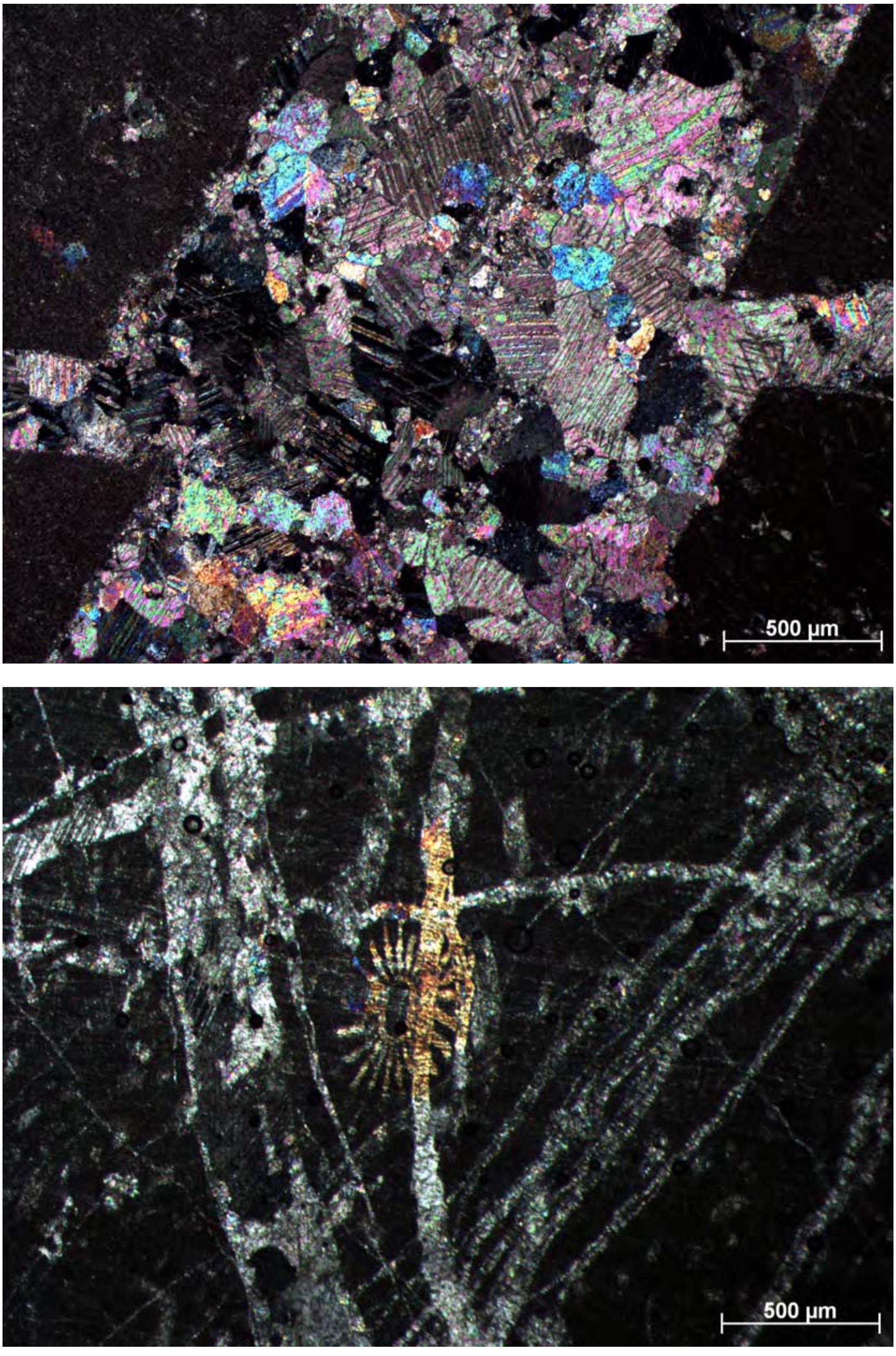

Figure 50: Figure shows lateral crystal growth not only in cross cutting veins (upper image), but also occurring at crossed cut Quartz fossils (lower image). Both images are taken under crossed polarized light.

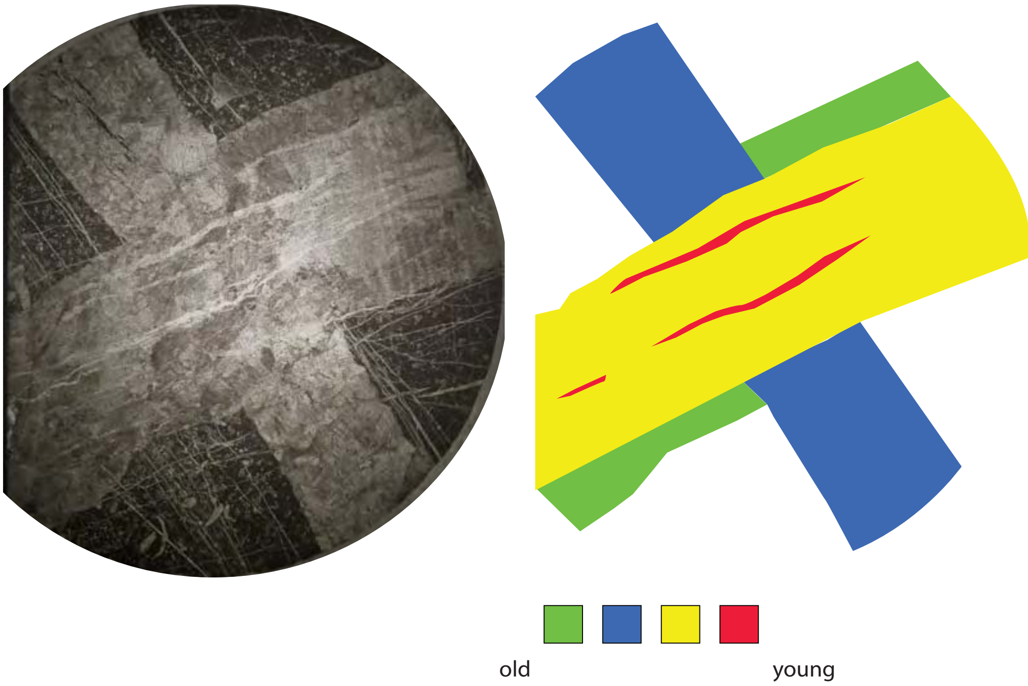

Figure 51: The sample JS-PL-009 shows a cyclic overprinting relationship. The micrograph was taken under plan polarized light. Diameter is 35mm. On the right a conceptional model for the overprinting relationships.

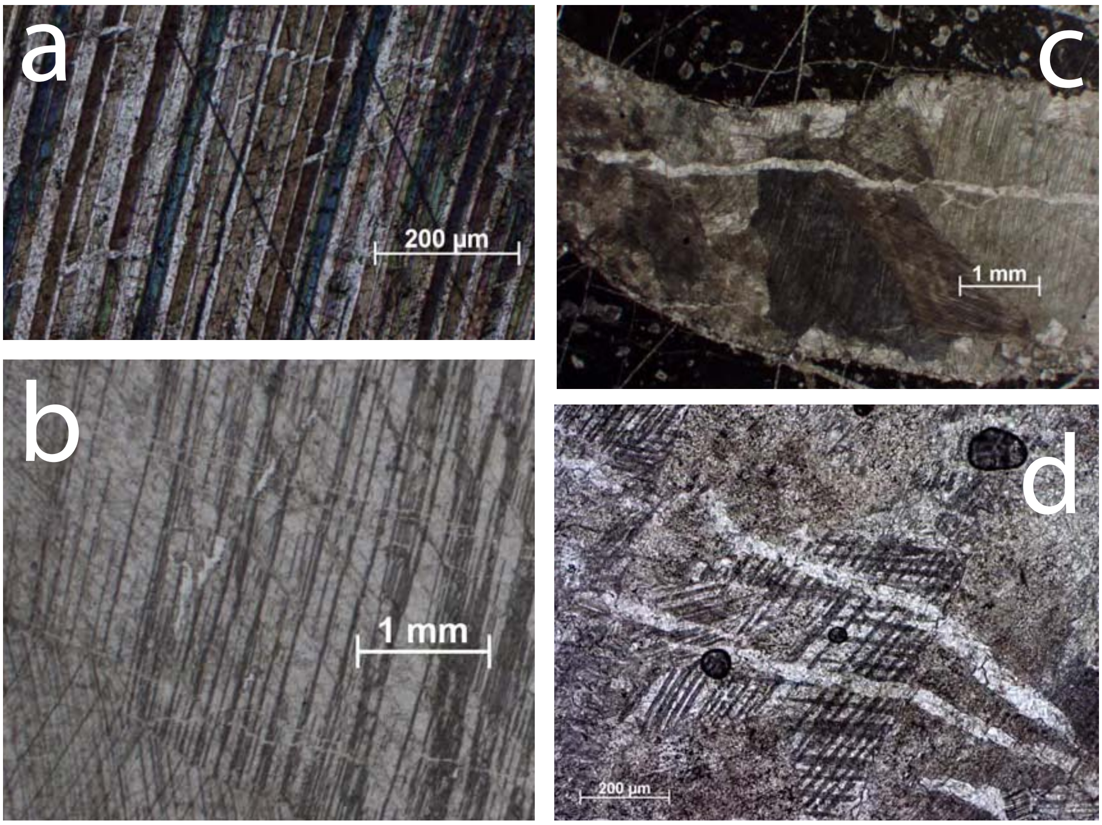

Figure 52: Micrograph plate illustrating veinlets in veins. a: new veinlets are following crystal lattices, which are decorated by deformation twins (XPL). b: veinlet cutting through deformation twins (PPL). c: a thick vein is penetrated by a small vein, which cement color is brighter (PPL). d: veinlets lacking deformation twins cut through calcite crystals decorated by deformation twins (PPL).

3.3.5 Crack-Seal textures

Intermediate to thick veins show different ways of crack-seal textures. Lateral thickness variations of intermediate veins provide the opportunity to investigate different crack seal textures. This does not mean one massive vein is getting thinner instantaneously but it splits up in two or - more often - in several branches (splays) merging eventually together to form a single massive vein again. After merge the individual veins usually share the same crystals (lateral growth or epitaxial growth, see chapter 3.3.4). Identification of crack and seal events can be deduced from counting branches at merging locations. Crack seal patterns can be observed in thick veins as well. Some but not all calcite crystals contain host rock inclusions, which are parallel to the vein host rock interface. The inclusions are evenly spaced and have a elongate shape (flakes; figure 54). These so-called flake swarms are confined to single coarse-grained crystals. Host rock inclusions may contain fossils that are distorting the inclusion's regular shape and spacing (figure 54).

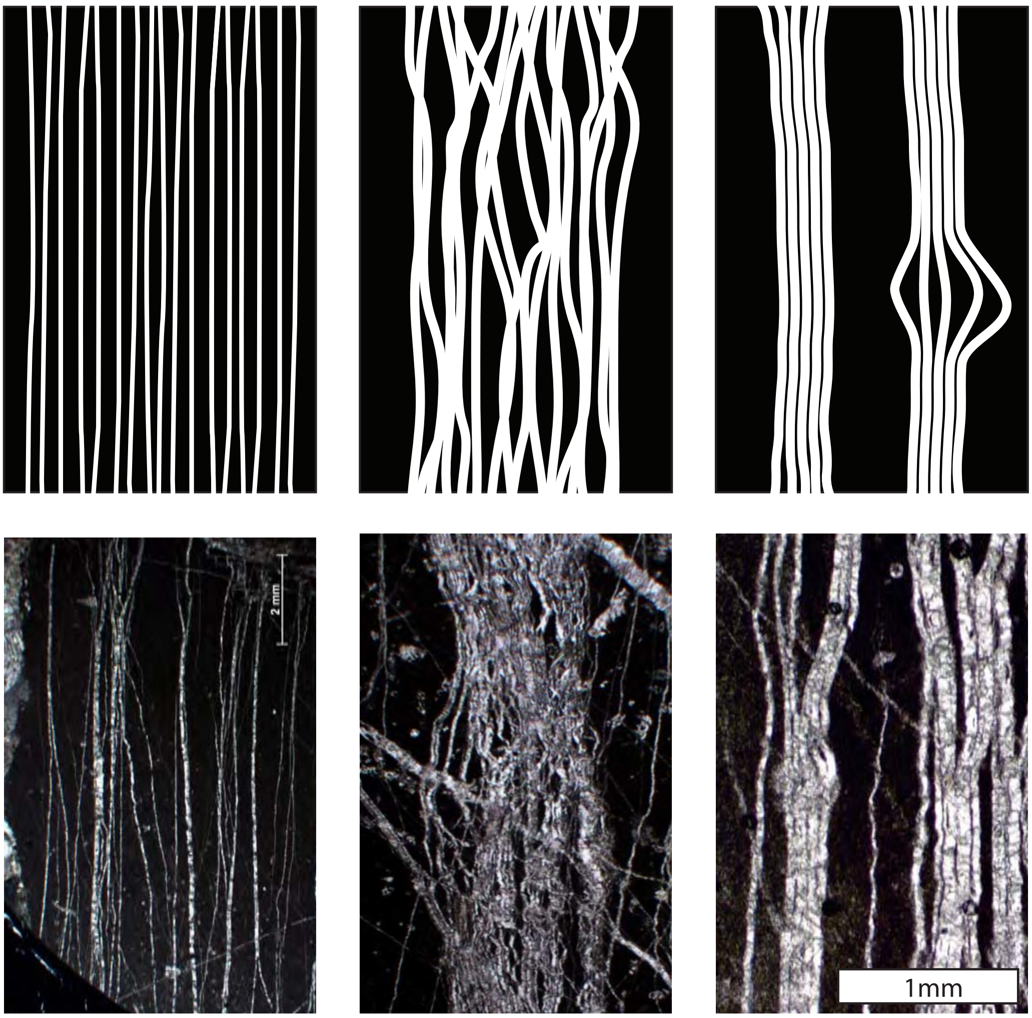

Figure 53: Different patterns of closely spaced healed fractures. The left set illustrates a parallel vein array (micrograph: XPL). The bundle-style is illustrated by the middle set (micrograph: XPL), while the right set shows the geometry for aligned vein with persistent host rock inclusions (micrograph: PPL).

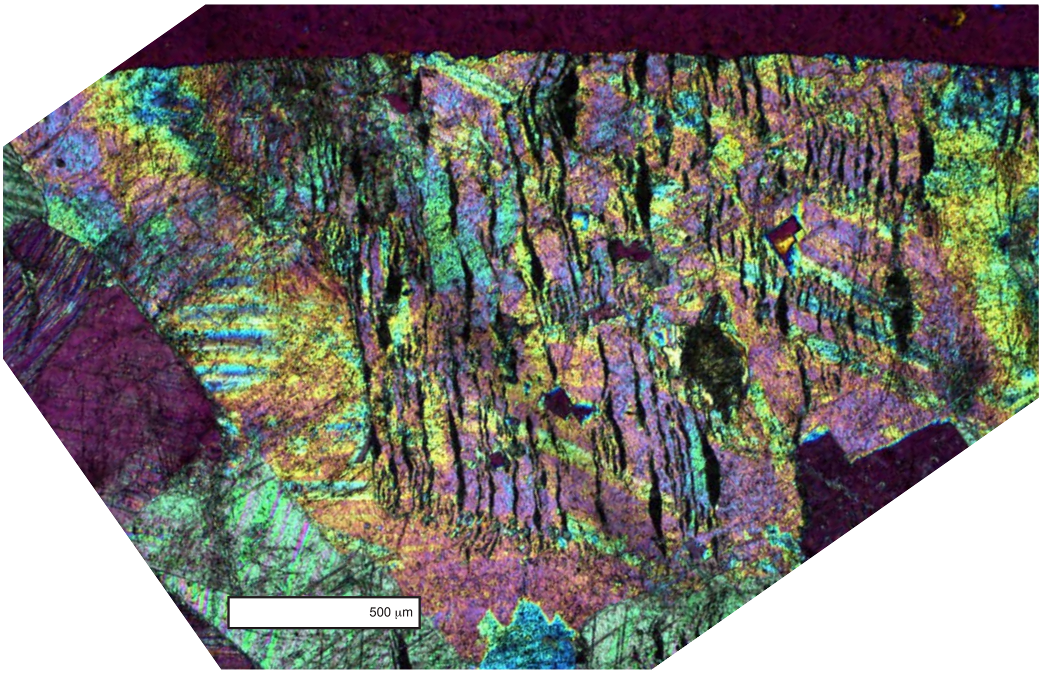

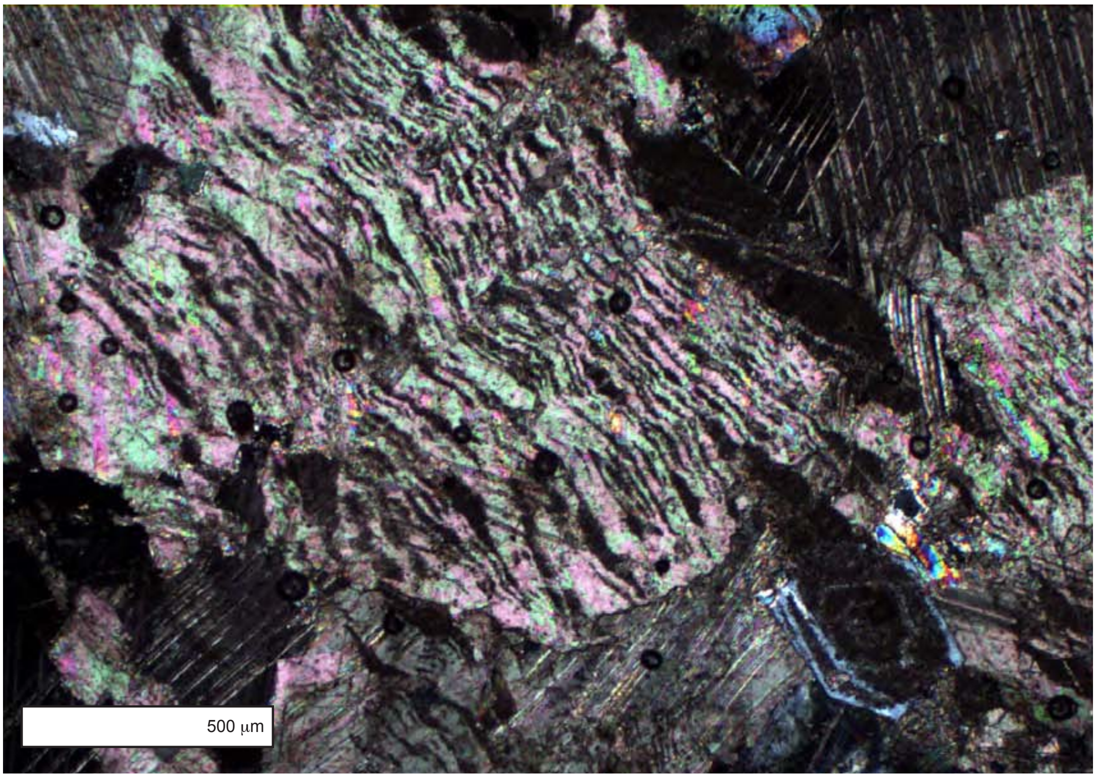

Figure 54: Sub parallel oriented elongated hostrock inclusions that are confined to a single crystal. The flake swarms are parallel to vein-hostrock interface. Both images are taken under crossed polarized light. The crystals do also contain bigger massive host rock inclusion as well as entire Qz-fossils with still persistent pressure shadows (lower right corner of the lower image).

3.3.6 Vein arrays and bundles

We differentiated grouped micro veins by their group's shape and their orientation to each other. If we observed straight veinlets evenly and parallel oriented to each other we name them arrays (figure 53). The veins of an array are mostly isolated from each other. A different fashion is represented by vein bundles with curve-shaped branches, that are oriented sub-parallel to each other creating an anastomosing pattern (figure 53). We figured a transition from arrays over bundles and splays to crack seal texture (chapter 3.3.5)(see figure 53).

3.3.7 Vein interaction structures

The last three chapters present a lot of examples of how veins have interfered with each other. Here we discuss a number of additional examples, which are similar to structures observed on broader scale (chapter 3.1, 3.2). Apart from the bundles mentioned in the last chapter we observed alignment (chapter 3.1.3.1.2) and en-echelon veins (chapter 3.1.3.4), but also veins with a curvature (see 55).

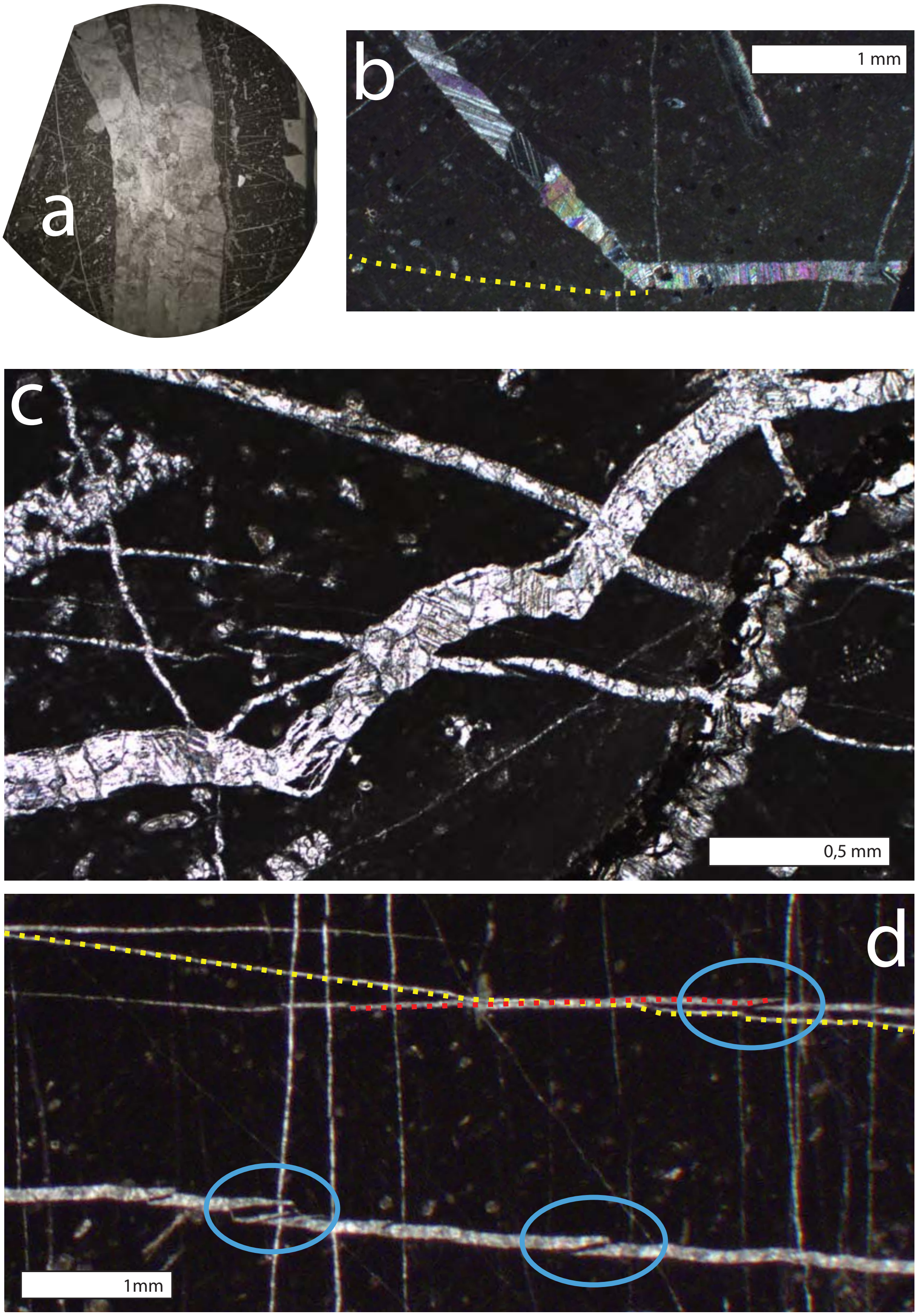

Figure 55: a: overview of thin section JS-PL-001 (PPL). One can clearly see how a vein from the top left corner joins another vein building together a vein stack. b: a intermediate vein is deflected by a very thin veinlet, which has been sketched with a yellow dashed line. Note: two other veins are offset dextrally, but one cannot tell, whether the older (yellow dashed) or the deviated younger vein created this offset (micrograph: XPL). c: curved intermediate vein with splay features (micrograph: PPL). d: example for alignment and en echelon. Host rock bridges in en echelon veins are highlighted by blue ellipses, while the yellow dashed lines track a veinlet that aligns with another vein (red dashed line) (micrograph: PPL).

3.3.8 **Calcite crystal deformation**

The calcite cement crystals do generally show plastic deformation in form of deformation twins. The presence of two intersecting twin orientations (type I and II; Burkhard 1993, Passchier & Trouw 2005) is very common. In minor cases curving of these can be observed (figure 56) which can be classified as types III after Passchier and Trow (Passchier & Trouw 2005) and Burkhard (Burkhard 1993). However we found intermediate veins at various strike directions, which lack deformation twins. They are commonly observed cross cutting other veins (juvenile veins, veins in veins). These so-called juvenile veins have also been observed to follow crystal lattices and deformation twins respectively. They show strike directions predominantly between 60° and 100° (figure 57).

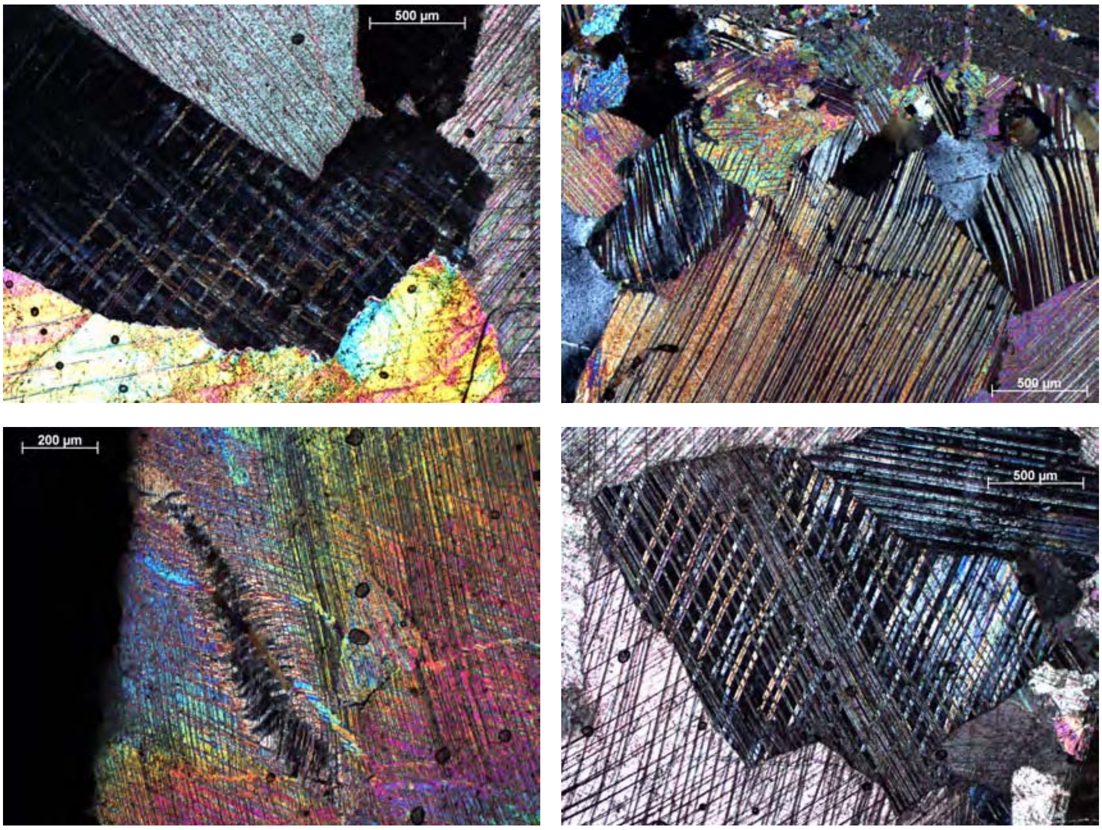

Figure 56: Figure shows deformation twins in calcite crystals of thick veins. Top left and bottom right: Type II twins, top right: mostly type I twins. Bottom left: mostly type I-II twins, but also a nice example for type III twins. Types are according to (Burkhard 1993, Passchier & Trouw 2005).

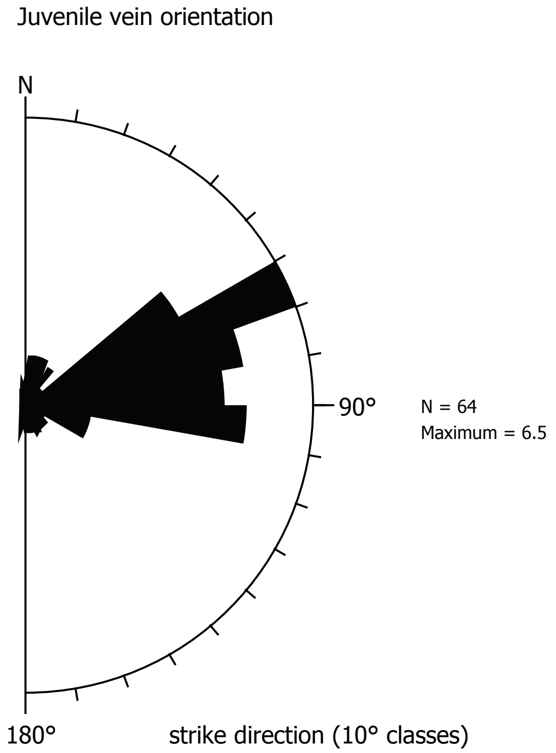

Figure 57: Rose diagram showing the strike distribution of juvenile veins. See text.

3.3.9 **Stylolites and interaction with veins**

Stylolites, which can be found in almost every thin section, show a complex age relationship with microscopic veins. They are cross cut by veins as well as overprinting existing veins. From our field observations we know that stylolithes show various orientations (see figure 58). We have observed accumulations of non-calcareous matter as opaque minerals, detrital Quartz as well as Quartz fossils (figure 58). As we have mentioned earlier stylolites to interact with veins. Fuzzy vein boundaries are usually caused by stylolites that have dissolved the veins partly. This observation corresponds to the chain saw structures observed on detail image scale (chapter 3.2.4). Some thin sections do provide evidence that stylolites have dissolved major parts of existing veins (JS-PL-048).

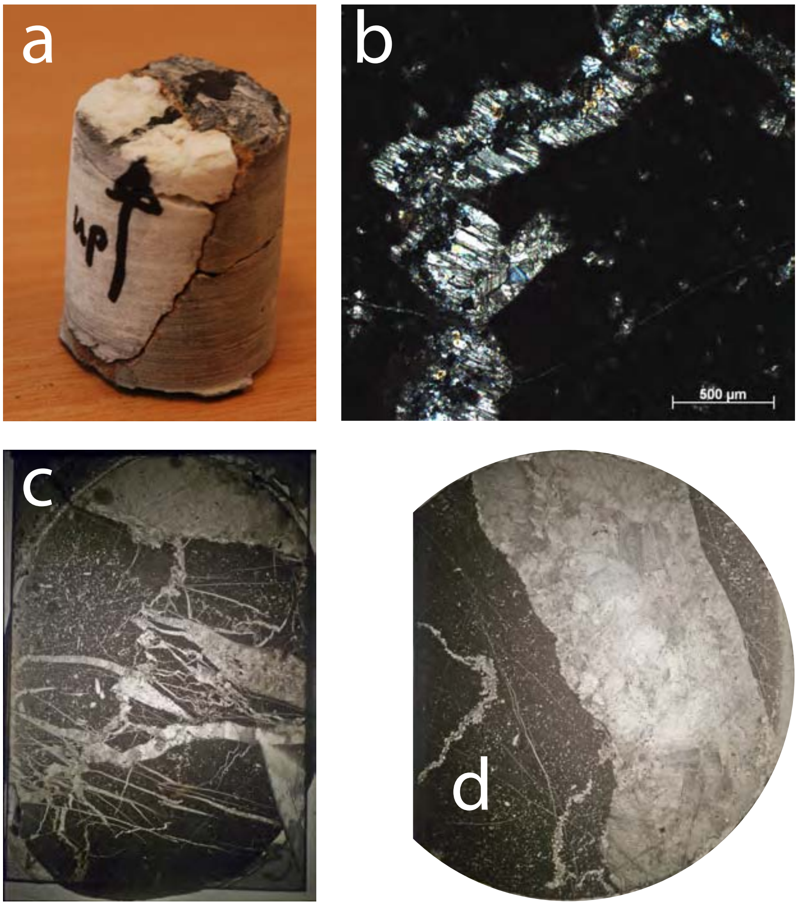

Figure 58: a: An oblique oriented stylolite has affected the interface between a vein and the host rock. The sample actually cracked along the seam. Plug (diameter 35 mm) has been taken perpendicular to bedding. b: Qz-pressure fringes at a stylolite (XPL). c: overview image of JS-PL-048 shows massive pressure solution). One can see remnants of veins that are almost completely dissolved (height of image 4 cm, PPL. d: example for chain saw structures at microscopic scale. The vein-host rock interfaces to not fit to each other. A stylolite has started to dissolve the vein from the left side.

3.3.10 **Pressure shadows**

Some microscopic fossils show a pressure shadow. Most of them are Qz-bearing and they are even preserved around fossils that are encased in veins that are showing a crack-seal texture (compare chapter 3.3.6). Some thin sections showed pressure fringes consisting of elongated Qz crystals localized at stylolites. Pressure shadows are three-dimensional objects (ellipsoids). We don't know the orientation of the ellipsoid, but we know that they were all cut parallel to the bedding. However we measured the orientation of the longest axis of the ellipse in the thin sections. Their orientation is dominantly between 30° - 50° (figure 59).

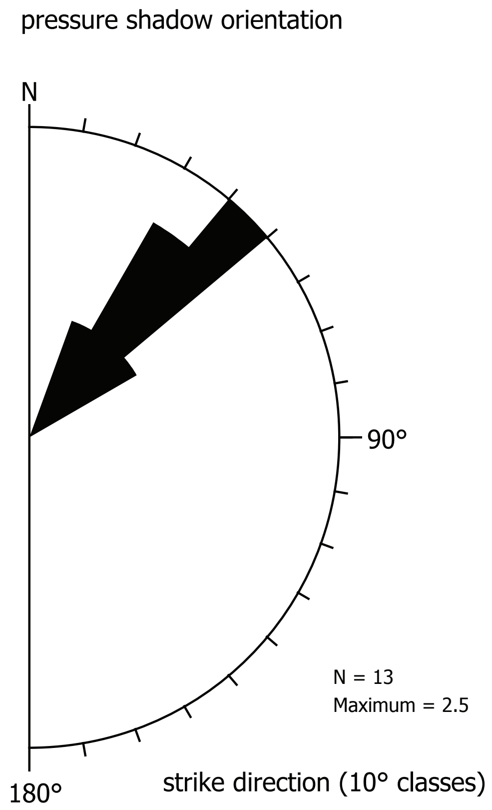

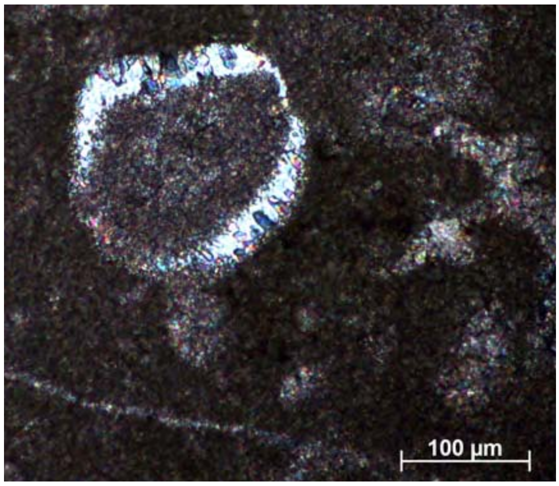

Figure 59: Rose diagram showing the main strike direction of pressure shadows found mainly at Qz-fossils. The strike directions are restricted to bedding parallel orientation. The effective orientation of the pressure shadow ellipsoid is unclear.

3.4 Vein geochemistry

3.4.1 Stable isotope results

We measured stable isotope ratios (δ13CPDB and the δ18OSMOW) of 161 samples. A number of 58 measurements failed due to technical problems of the mass spectrometer. Hence we have valid results for 103 stable isotope measurements (see appendix 8.1).

Figure 60 shows the total data plotting the δ13CPDB versus δ18OSMOW. The Host rock's isotopic signatures show small ranges for both δ18O (1.13 normalized against SMOW, standard mean ocean water) and δ13C (0.79 normalized against PeeDeeBee standard). The calcite vein's isotopic signature is more variable on both oxygen (3.7) and carbon (2.99) scale. Vein δ18OSMOW values are ranging from 22.48 to 26.18 and δ13CPDB values show a significantly high range from -0.84 to 2.15. The veins minimum oxygen values match the host rock values and then show a trend towards heavier atomic ratios. For carbon it is vice versa. Vein maximum values match the host rock signature and trend down towards lighter atomic ratios.

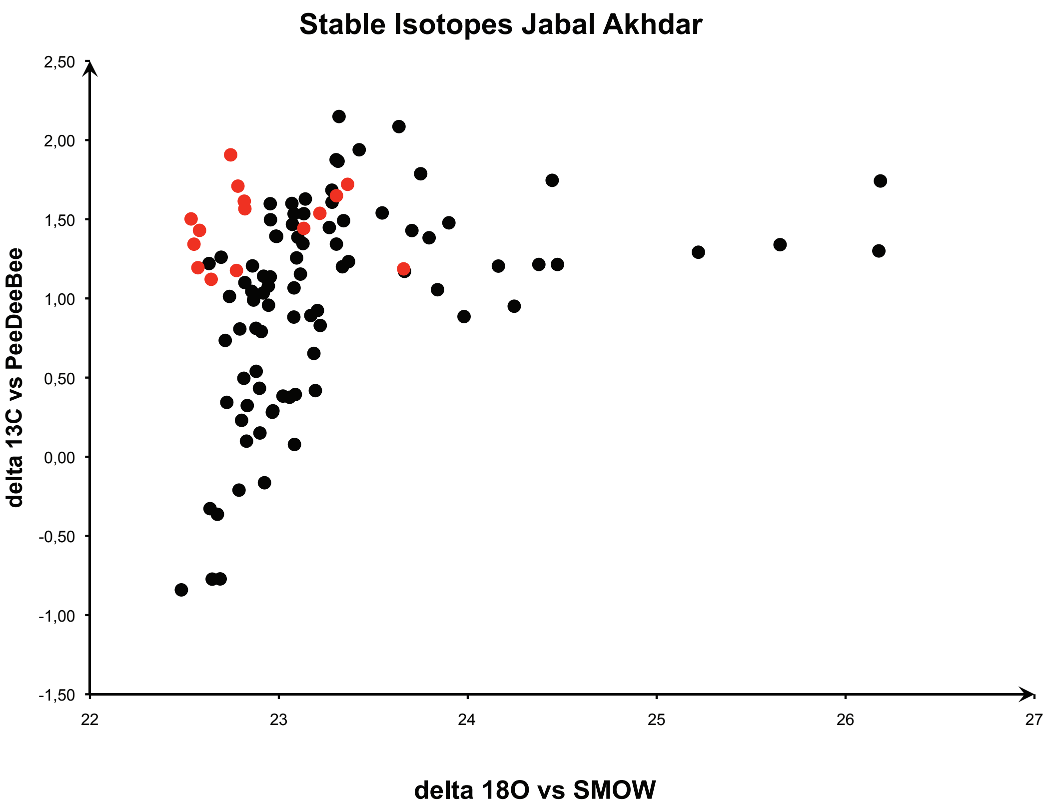

Figure 60: Plot of stable isotopes, δ13C vs. δ18O. See text for explanations.

3.4.2 Comparison with previous studies

Fluid flow and the origin of vein fluids in the Jabal Akhdar Anticline has been investigated in the past on different scales ((Hilgers et al. 2006, Holland & Urai in press) (Please refer to chapter 1.4). The δ18O host rock values are different from the older data (see figure 61). Note: the host rock data in this work has been measured very close to veins (<3,5cm distance to vein). While the previous studies showed a wide range of δ18O in the veins, our dataset does not so. The majority of the veins are in the range 22-24 δ18O normalized on the SMOW standard.

Looking at the δ13C values our data occupy a complete new area on the plot. The data of this work do not match any previous results. A lot of veins show a low δ13C signal with even negative values. The point cloud has a shape of a funnel that is going down (see figure 61 and 60). A similar shape can be identified by combining Hilgers' (Hilgers et al. 2006) and Holland's (Holland & Urai in press) data but at higher δ18O values at 27.

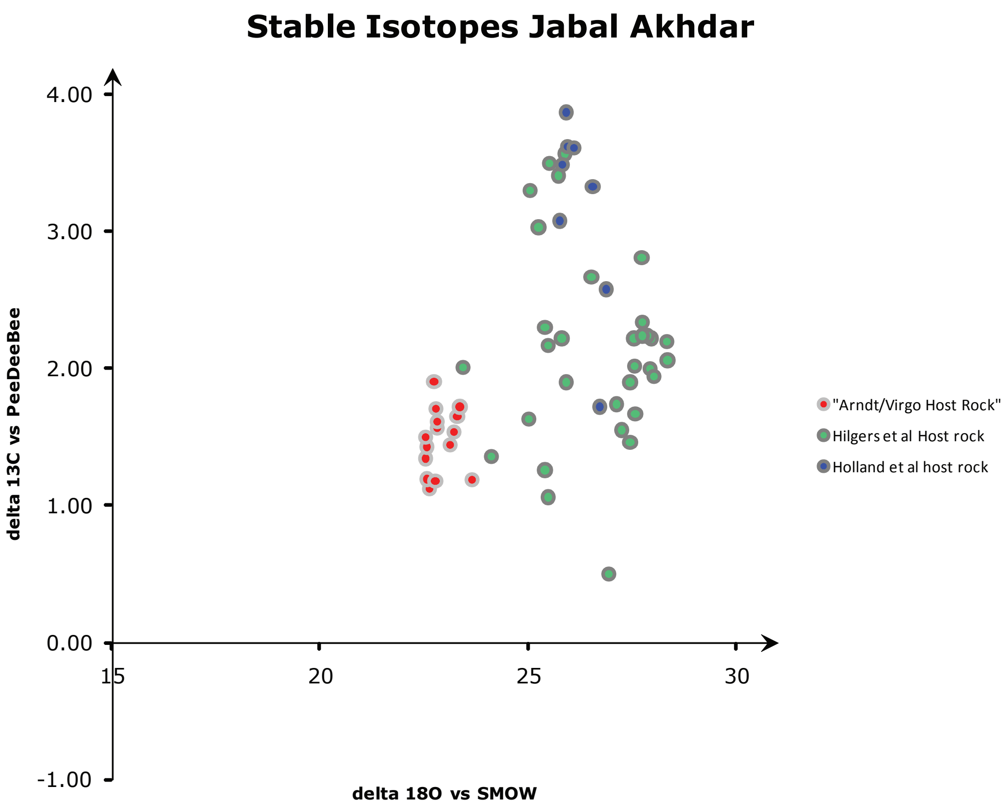

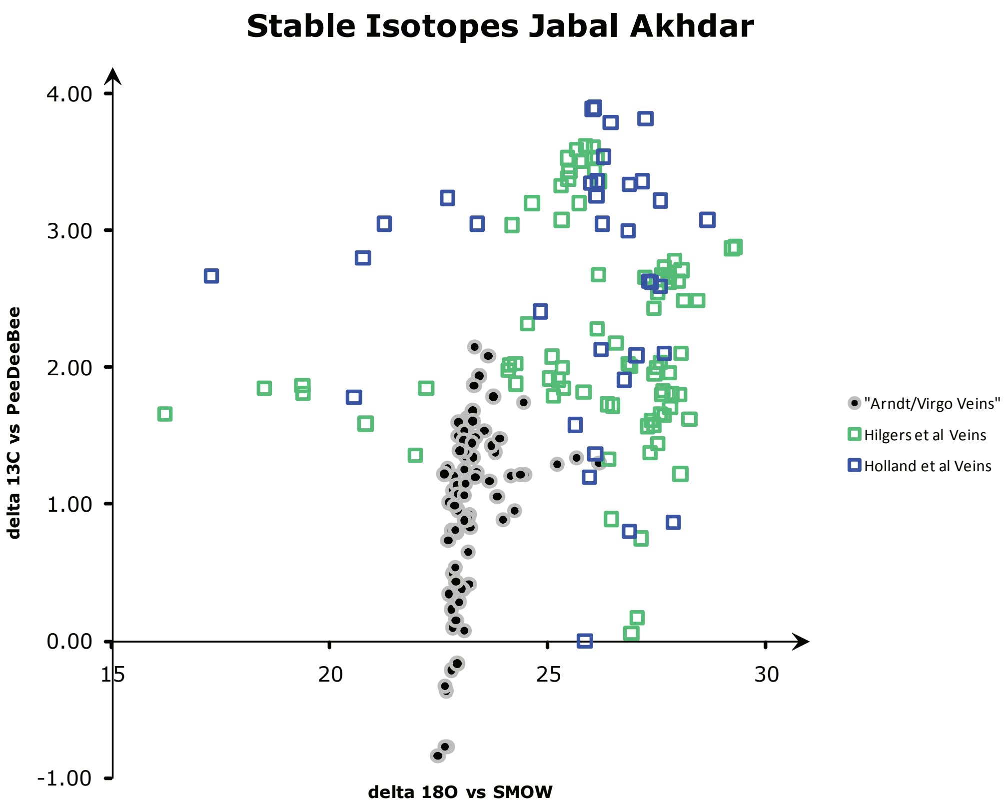

Figure 61: Comparison of stable isotope measurements of this thesis with previous results from Hilgers et al. and Holland and Urai (Hilgers et al. 2006, Holland & Urai in press). For further explanations consult text.

3.4.3 **Trends and clusters**

The spread in δ18O values is produced by a vein which we have sampled laterally, since it was the youngest cross cutting any other vein with an in plane movement. The vein comprises not only pure calcite veins but also red amorphous-opaque material (see figure 62 and figure 71).

A plot of isotropic traces within single samples that were measured both on vein crystals and on host rock does not give a clear image how vein signature relate to host rock signatures (figure 63).

There is no correlation of isotopic signature with vein strike direction (figure 64). Over the entire strike range there is an existing constant signal around 23 for oxygen. In the range between 60°-80° we find higher values above 23. This data is originates from the lateral vein sampling. As already mentioned, there is more variability in carbon for the measured veins. As already observed for oxygen: over the entire strike range a constant signal can be observed, which is approximately 1,25. One might identify the range between 130°-180, where all the lower carbon values are plotting.

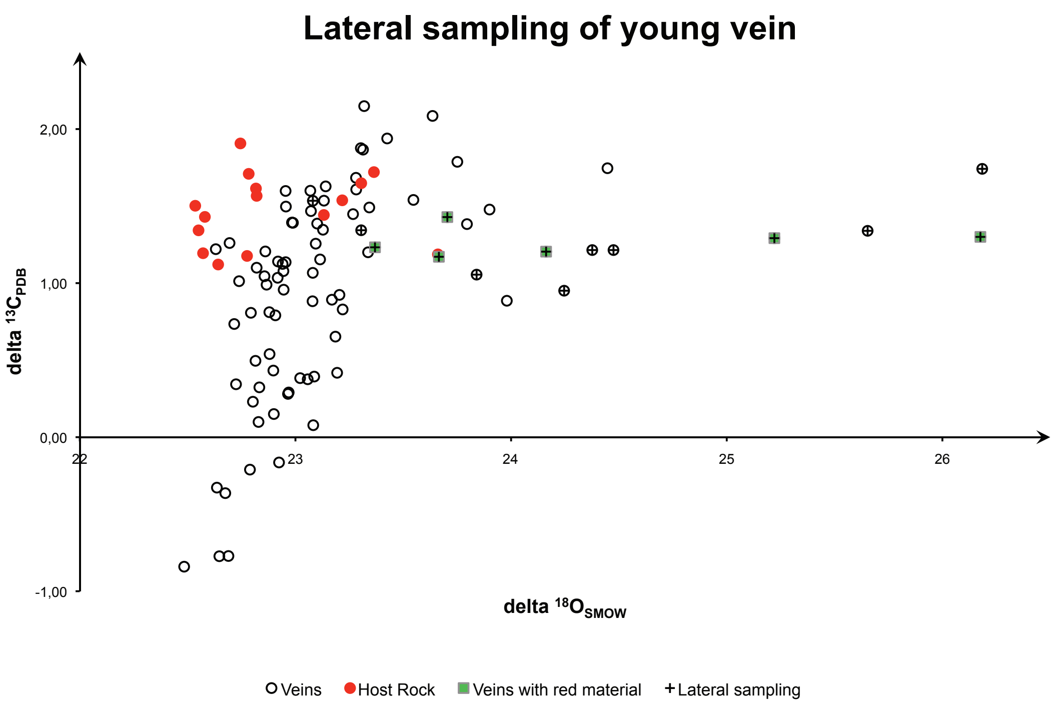

Figure 62: Stable isotope plot focusing on lateral fault vein sampling. The vein contains not only calcite but also red amorphous material, which has been interpreted as ferruginous material. See text for further explanations. See also chapter 3.4.4 and 3.4.5.

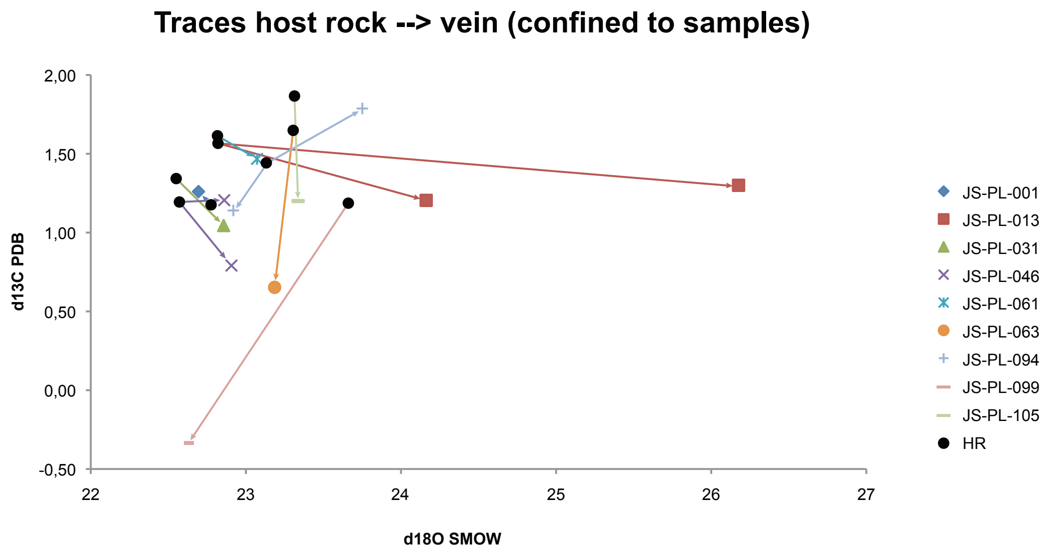

Example: JS-PL-094

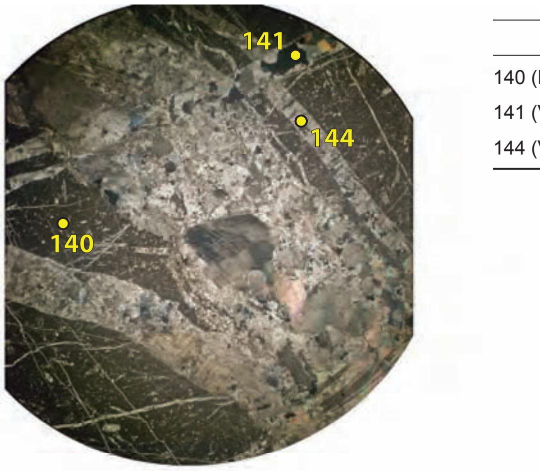

		d18O	d13C
140 (Host rock)	●	23,13	1,44
141 (Vein)	+	23,75	1,79
144 (Vein)	+	22,92	1,14

Figure 63: The stable isotope plots measured veins and host rock originating from the same sample. See further explanations in the text.

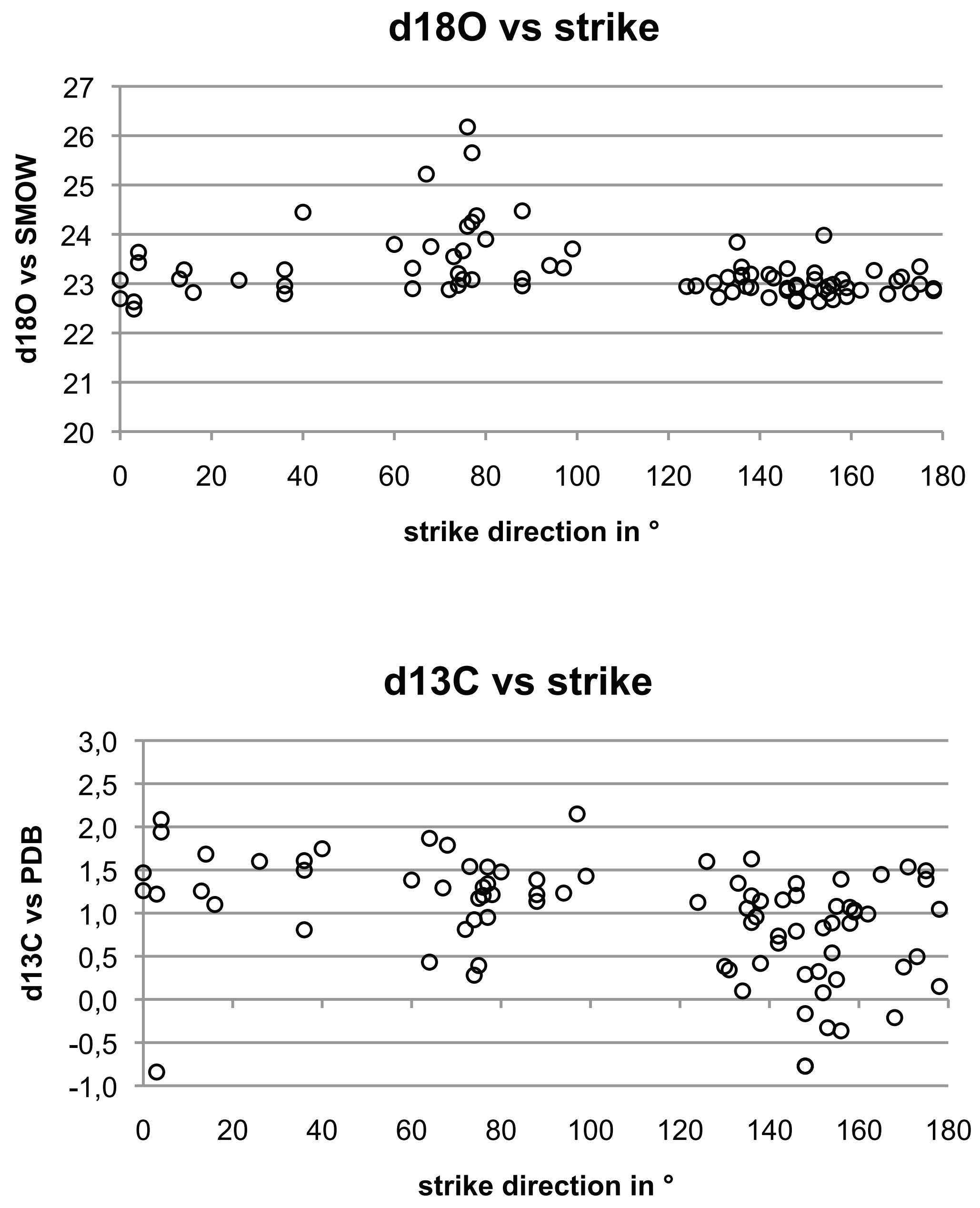

Figure 64: Plots displaying isotope values for d18O (upper plot) and d13C (lower plot) against vein strike direction. See text for further information.

3.4.4 Local variations

We can provide several stable isotope measurements conducted on a single sample. One could assume local isotopic variations being small within a small radius (e.g. 3.5 cm), but our data shows both small isotopic variations and large isotopic variations within a single sample. Some variations span over the entire data variability (JS-PL-013, 014, 016; see figure 65). The samples with a large variation in δ18O originate from a lateral sampling performed on a fault vein in the northern part (see also chapter 3.4.3). Large variations in δ13C can be observed in samples originating from a lateral vein sampling in the southern part of the pavement (JS-PL-091, 094, 096, 104). For further details read chapter 3.4.5. Therefore large isotopic variations in veins cannot only be observed laterally on meter scale, but also locally within a few cm (figure isotope variations).

Please see the sample internal variation figures (Figure 66-70). Cross sectioning of thick veins can show a high variability. A thick vein in sample JS-PL-003 has been measured twice (figure 66). This vein consists of at least two stacked veins caused by alignment that visible on all image scales. While oxygen isotopy changes a little (difference: 0,15), carbon isotopy changes a lot (difference: 2,06). The investigation of sample JS-PL-009 suggest a stable isotopy along the vein (red and yellow spot; figure 66) that is different from the cross cutting vein (blue spot).

Due to technical problems, it was not possible to allocate the samples JS-PL-081, 082, 083 in the dataset. They are marked red in the referring graphs (figure 65).

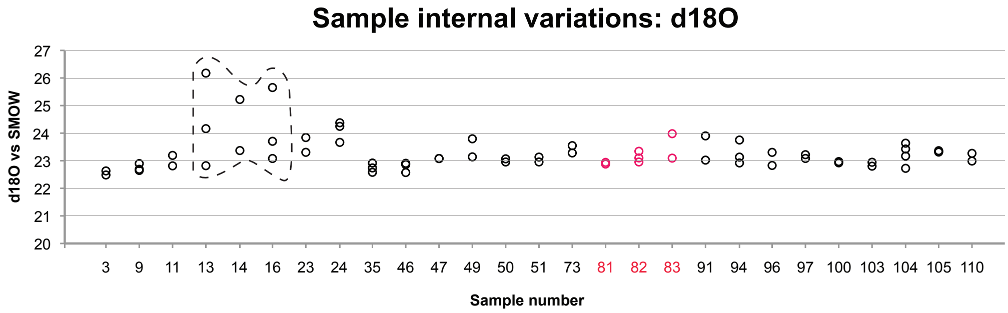

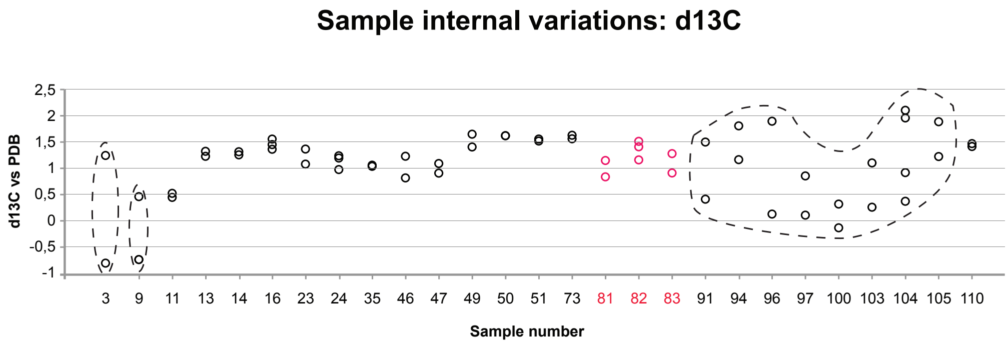

Figure 65: Isotopic variations within single samples. The upper chart shows the variability of d18O. Note the high isotopic variability for samples 13, 14 and 16 (outlined). These originate from a lateral sampling conducted on a fault vein in the northern part of the pavement. See also figure isotopes lateral sampling fault vein. The lower chart shows the variability of d13C values in each sample. Samples 3 and 9 do both show a relative large variability in carbon values. Consult figure sample internal isotope variations (I) 003+009+011+013+014 for a detailed look. Other samples with a large variability (91, 94, 96, 97, 100, 103, 104, 105) are collected from a lateral vein sampling in the southern part of the pavement. Details can bee seen in figure isotopes lateral vein sampling.

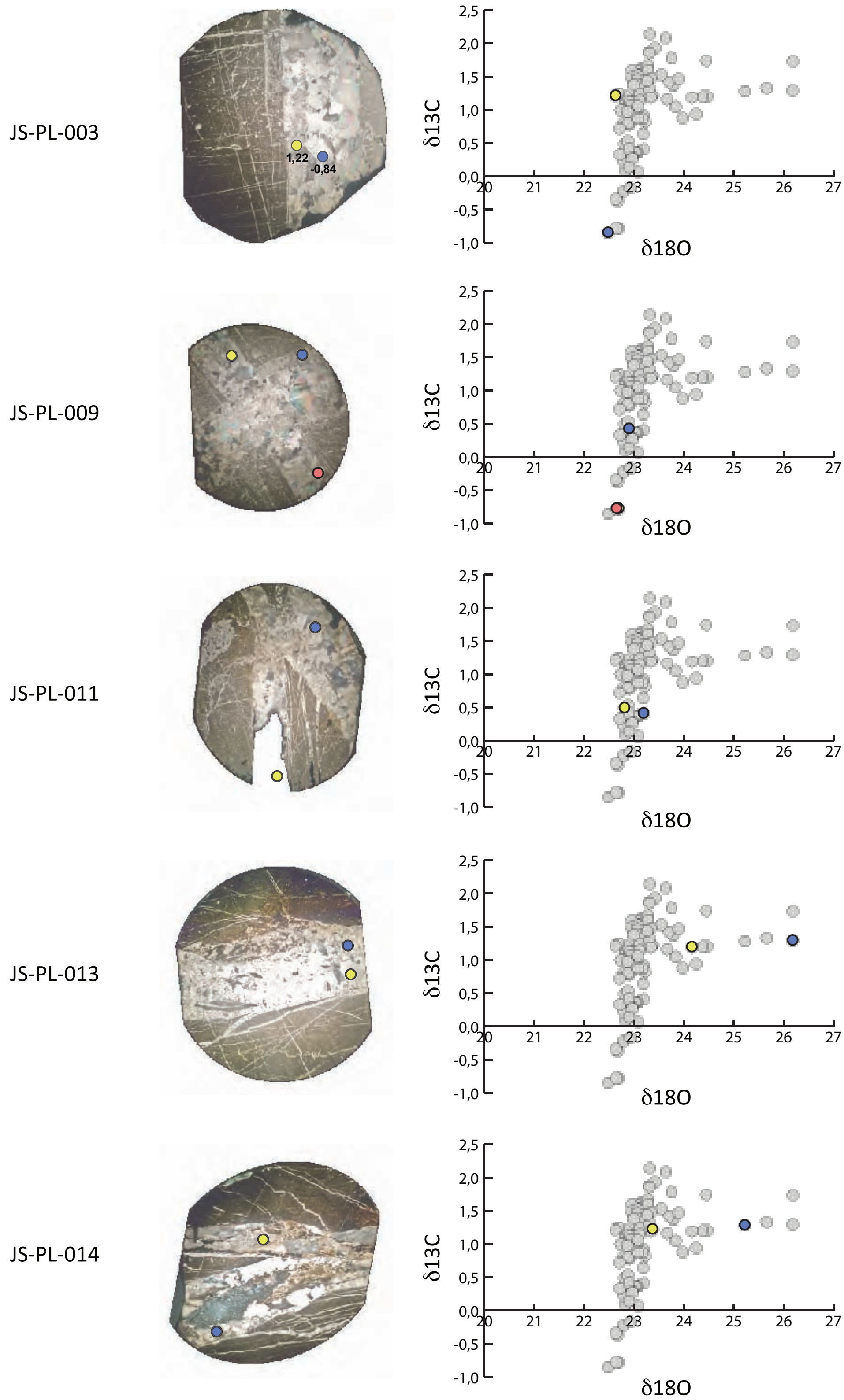

Figure 66: The figure is showing local isotope variations in samples with more than one measurement. Measurement positions are marked with colored dots that refer to the plot on the right side. The overall vein data is plotted gray in the background. Sample JS-PL-003 shows a high difference in d13C across the vein, while JS-PL-013 shows a high variability in oxygen across the vein.

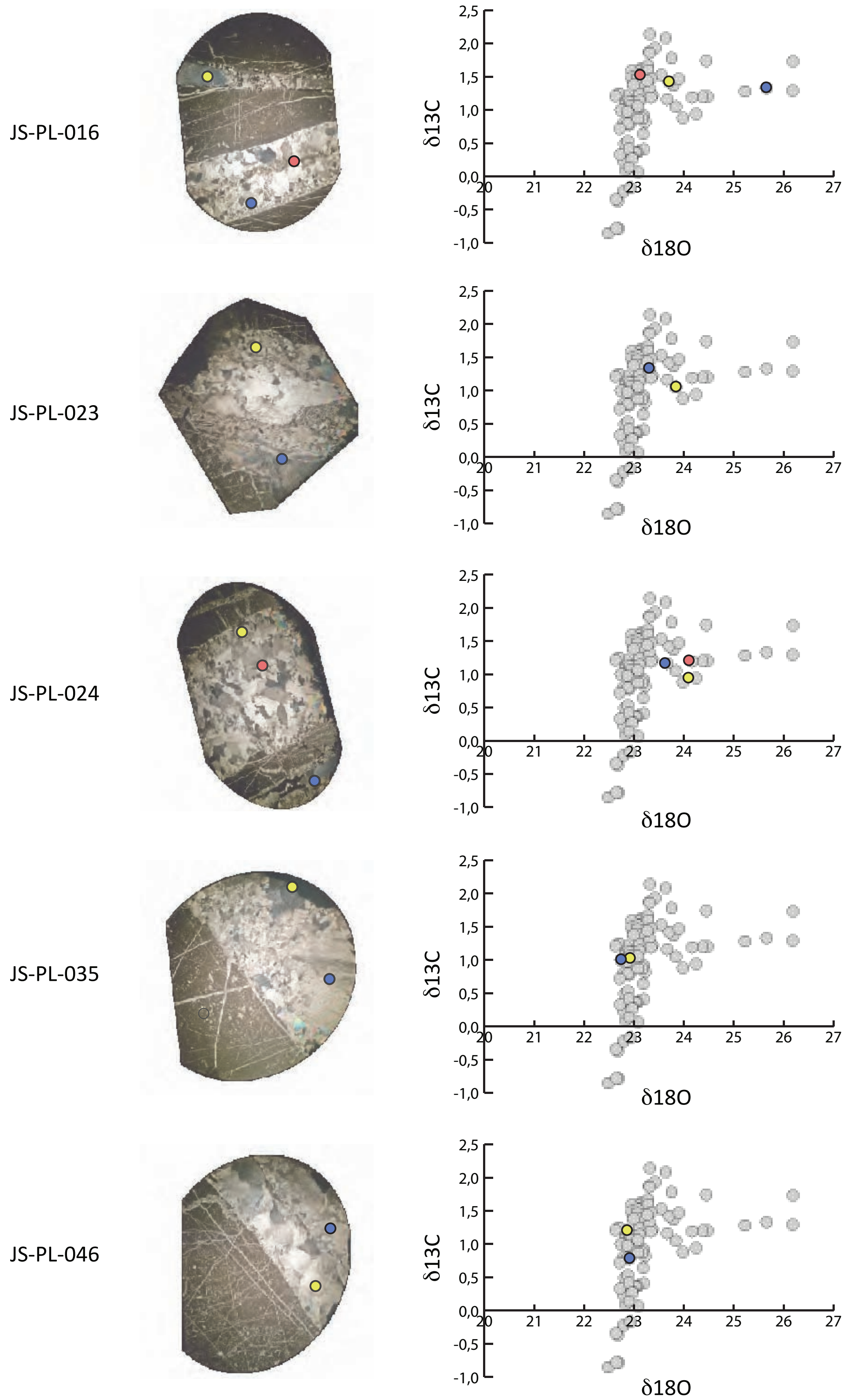

Figure 67: The figure is showing local isotope variations in samples with more than one measurement. Measurement positions are marked with colored dots that refer to the plot on the right side. The overall vein data is plotted gray in the background. Sample JS-PL-016 shows a high variability in oxygen across a vein (blue and red dot), while the other samples do not show a high variable isotopy.

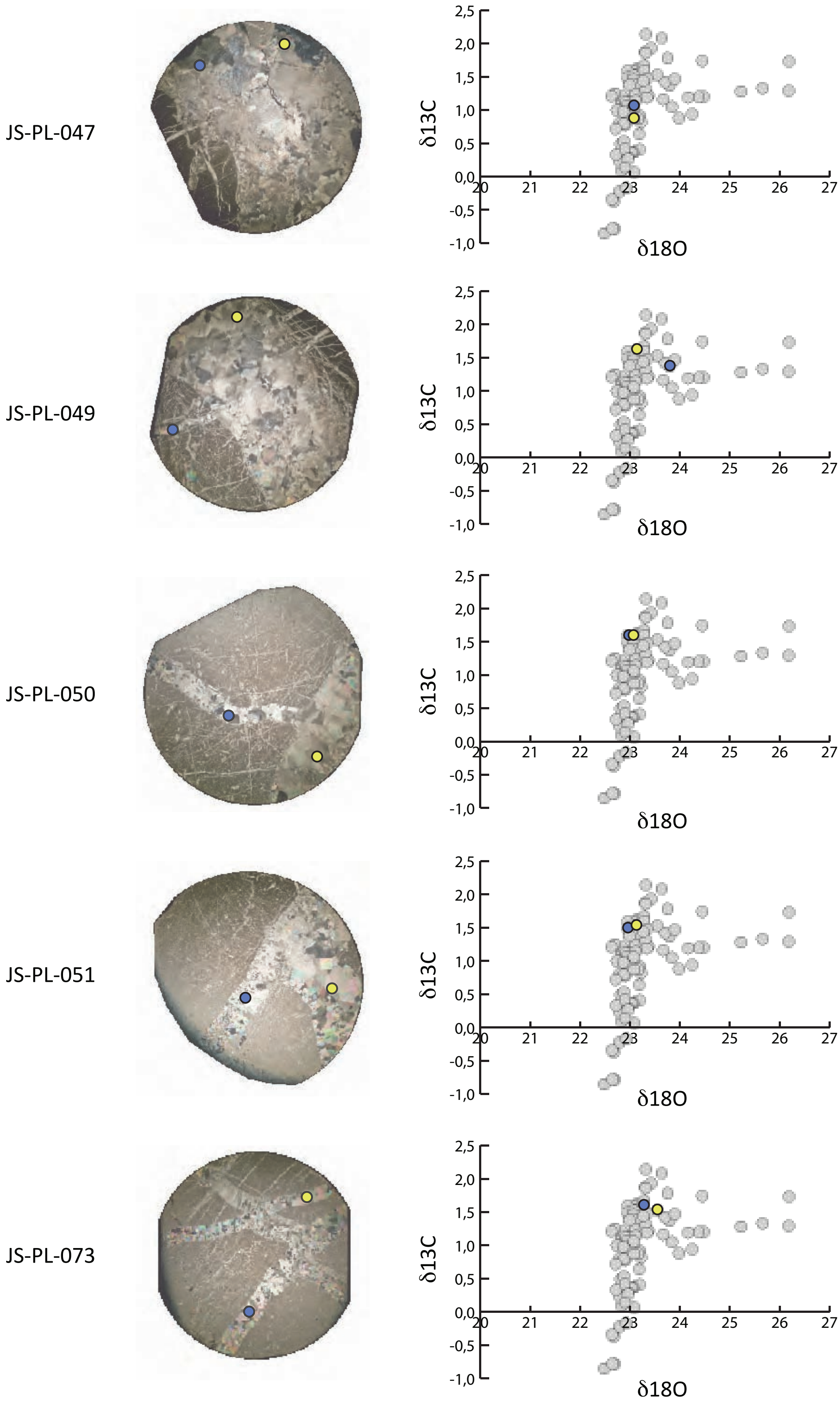

Figure 68: The figure is showing local isotope variations in samples with more than one measurement. Measurement positions are marked with colored dots that refer to the plot on the right side. The overall vein data is plotted gray in the background. All samples do not show a large isotope variability, even if measured in different veins (JS-PL-049, 050, 051, 073).

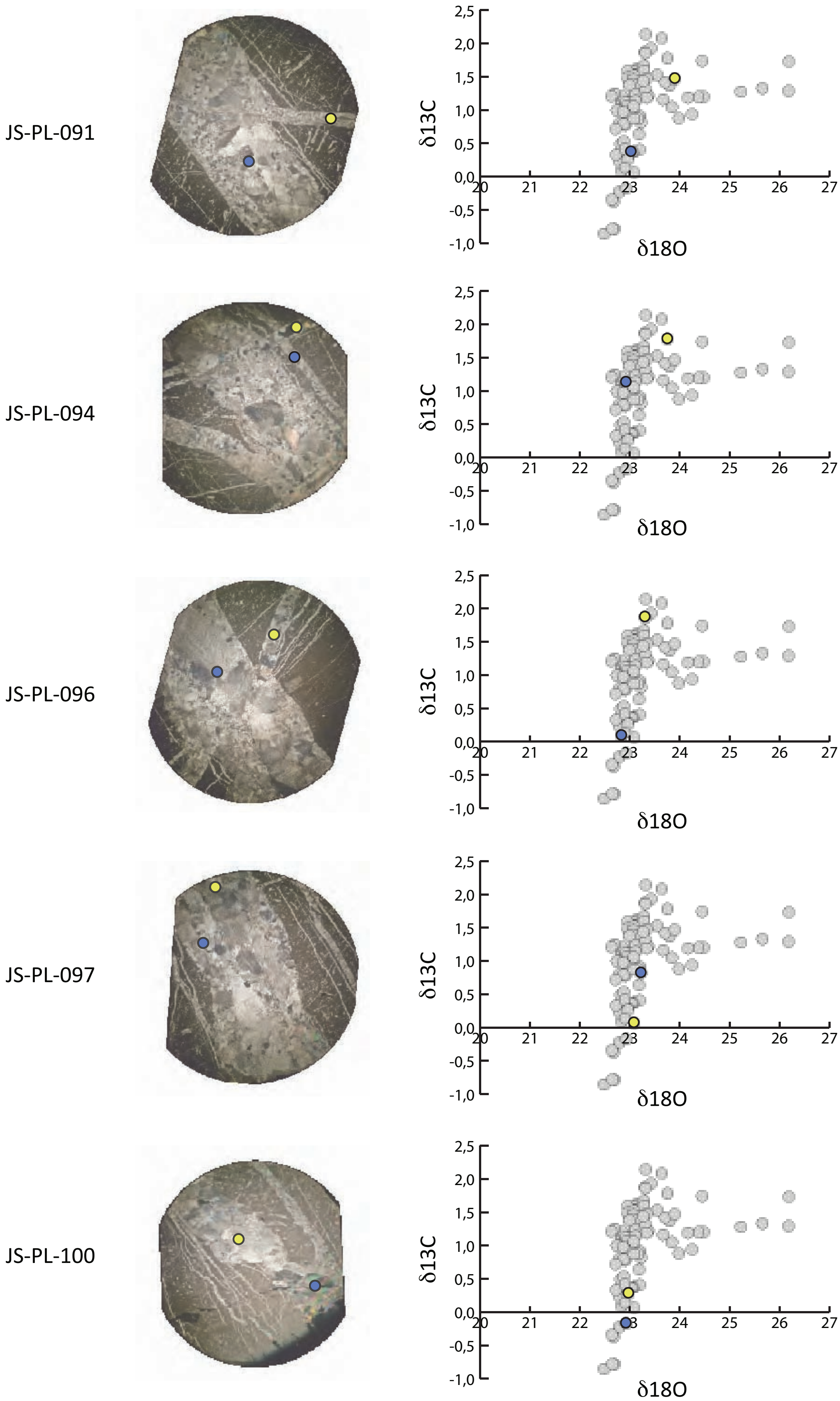

Figure 69: The figure is showing local isotope variations in samples with more than one measurement. Measurement positions are marked with colored dots that refer to the plot on the right side. The overall vein data is plotted gray in the background. In contrast to the observations in figure sample internal isotope variations (III) 047+049+050+051+073 we observed high isotope variability within some samples. In these cases the measured values originate from different veins (JS-PL-091, 094, 096) and is mainly constrained to changes in carbon isotopy.

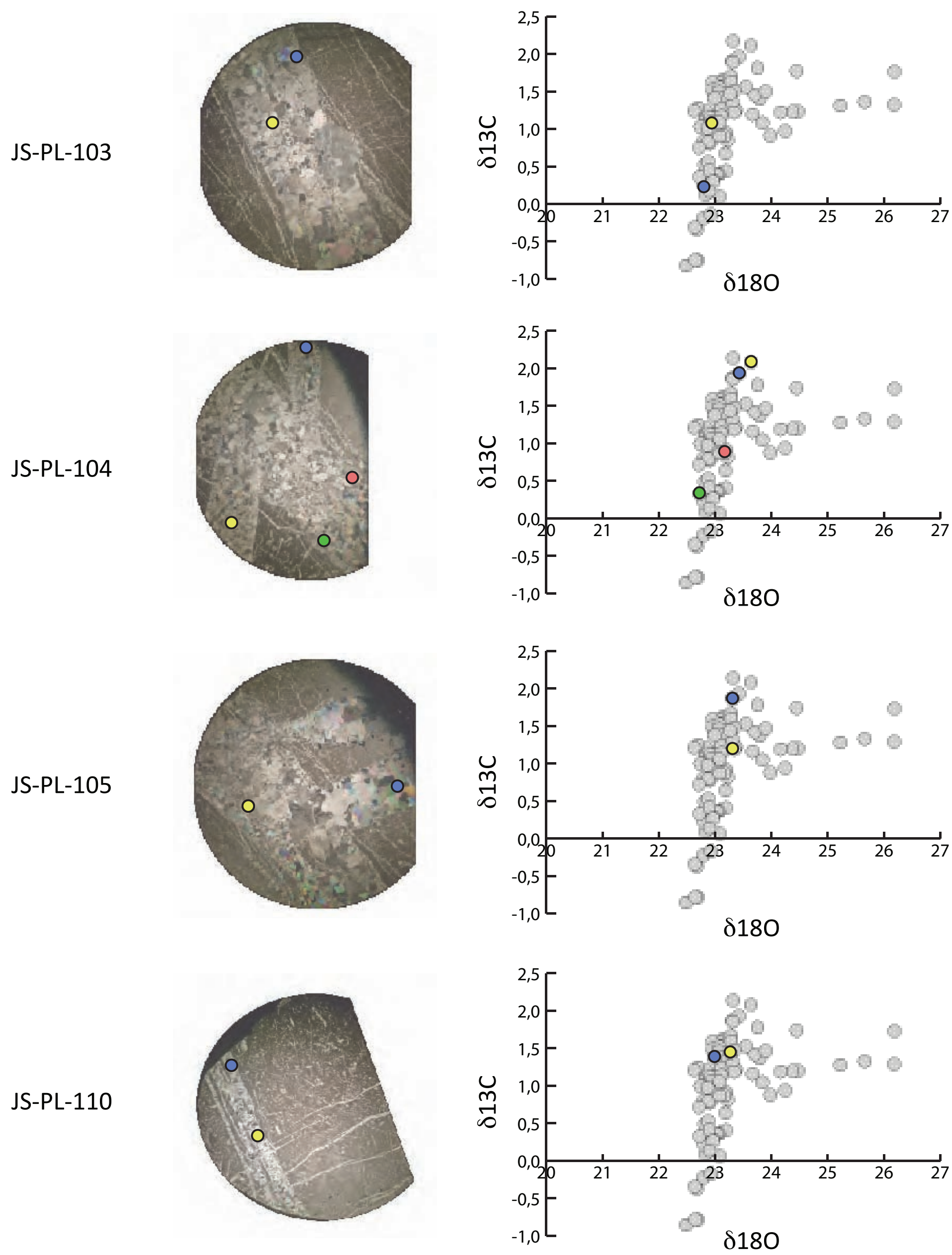

Figure 70: The figure is showing local isotope variations in samples with more than one measurement. Measurement positions are marked with colored dots that refer to the plot on the right side. The overall vein data is plotted gray in the background.

3.4.5 **Vein lateral variations**

Vein lateral observations of isotopic signals reveal highly variable isotope values with distance (figures 71 & 72). We present two detail studies on laterally sampled veins, the first being a fault vein with a vertical offset. This vein cross cut any other vein in the area (figure71). Oxygen isotopy varies a lot lateral along the vein as well and there seems to be no correlation between distance and the isotopy.

The second case is a vein that is sub-perpendicular to bedding (060/86) and can be regarded as typical for the pavement (figure 72). Both isotope ratios for oxygen an carbon are varying along the fault vein and there is no correlation between distance and the isotopy. But an interesting fact is, that the curves do show the same local trends. If oxygen shows increased values, so does the carbon (figure 72).

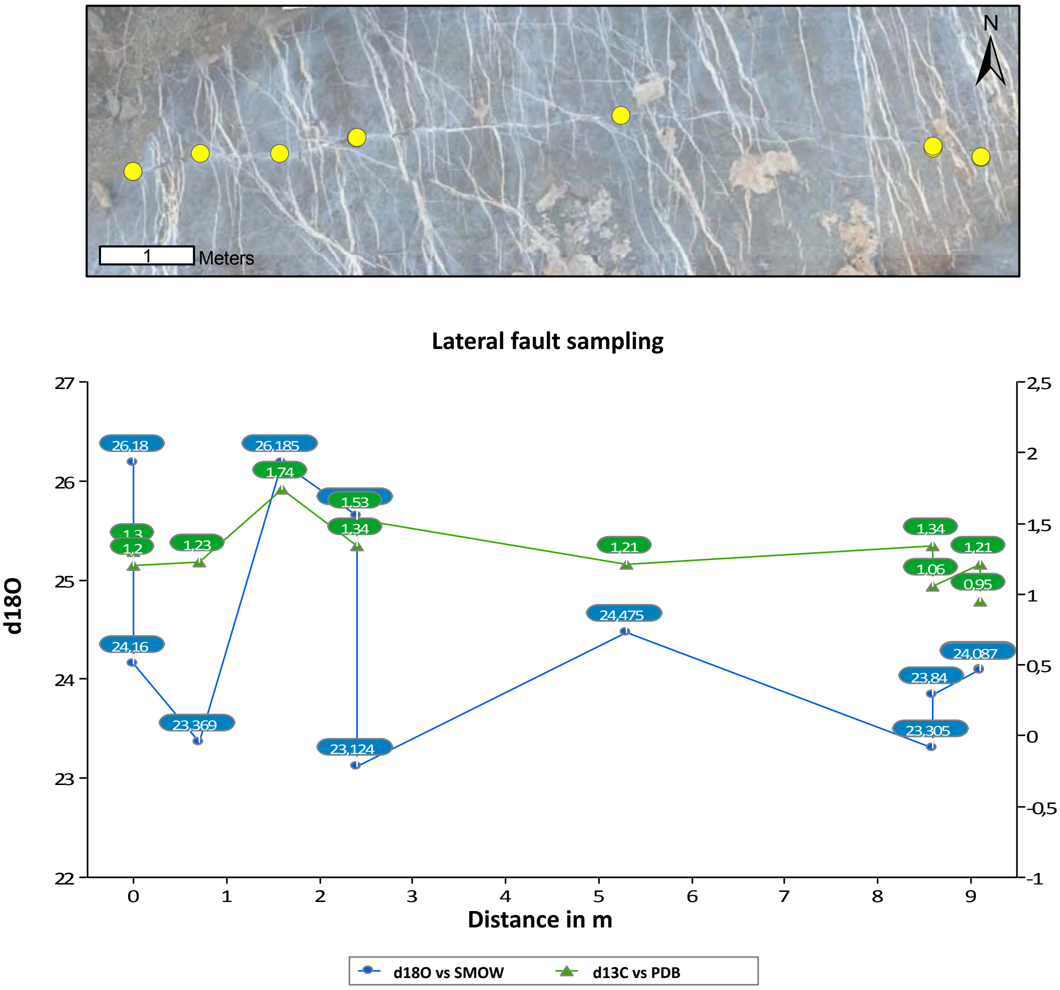

Figure 71: The figure illustrates a lateral sampling of a fault vein in the northern part of the pavement. The positions of isotope measurement are marked on the outcrop panorama. Distance was measured from left to right starting at the first sample point. The plot is showing no correlation of isotopy with distance. The vein shows a high variability in d18O while d13C values are stable.

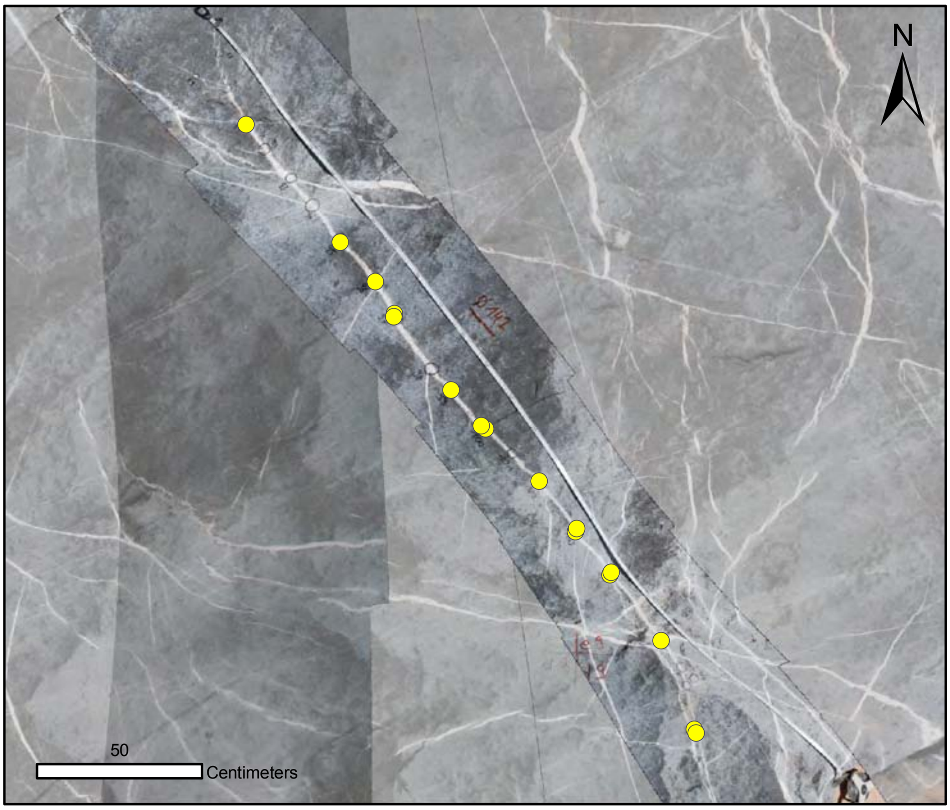

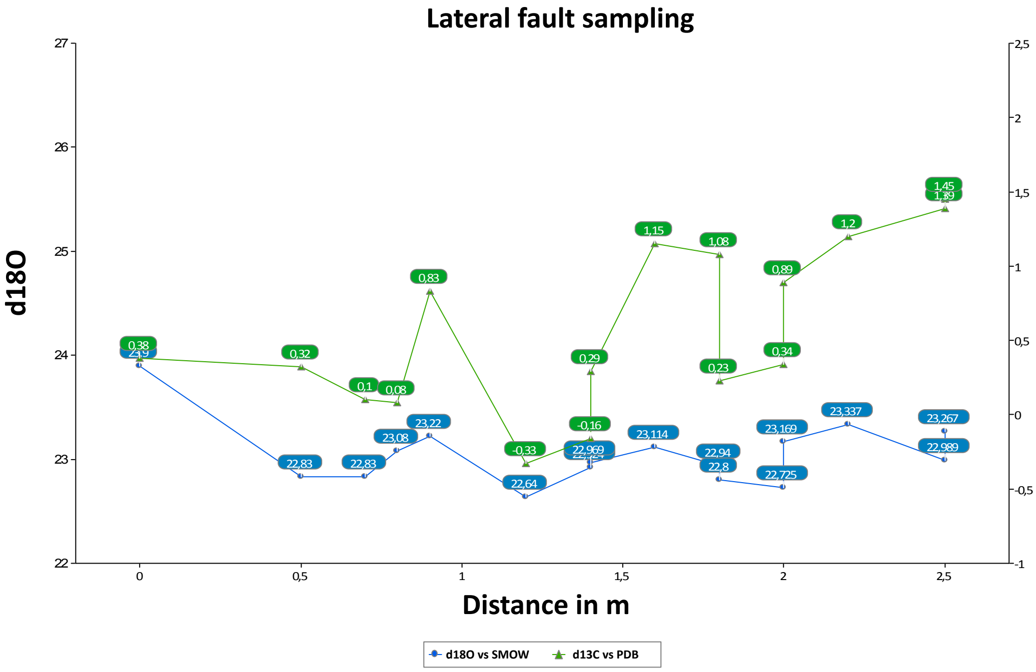

Figure 72: The figure illustrates a lateral isotope analysis of a vein in the southern part of the pavement. The positions of isotope measurement are marked on the outcrop panorama. Distance was measured from left to right starting at the first sample point. The isotopic curves generally show the same shape. If the oxygen slope is negative than the carbon slope is negative as well and the other way around.

4 Synopsis and Outlook

4.1 General achievements (Simon Virgo)

We investigated a polished limestone pavement of the upper Natih A Formation at the Western flank of Jabal Shams, Oman Mountains. Samples were taken at 110 locations over the outcrop for geochemical analysis and microstructural investigation. We present a workflow to capture the entire outcrop as a high-resolution image mosaic that allows us to investigate the complex vein network with millimeter resolution at an extent of tens of meters. It furthermore provides the base for an integrated, georeferenced framework in which observations at outcrop scale as well as microstructural investigation and stable isotope measurements are allocated, bridging the gaps from satellite imagery scale down to micro scale. All qualitative and quantitative data gathered in the field, by stable isotope geochemistry measurements or in microstructure image analysis can not only be statistically analyzed, but also in terms of their spatial distribution.

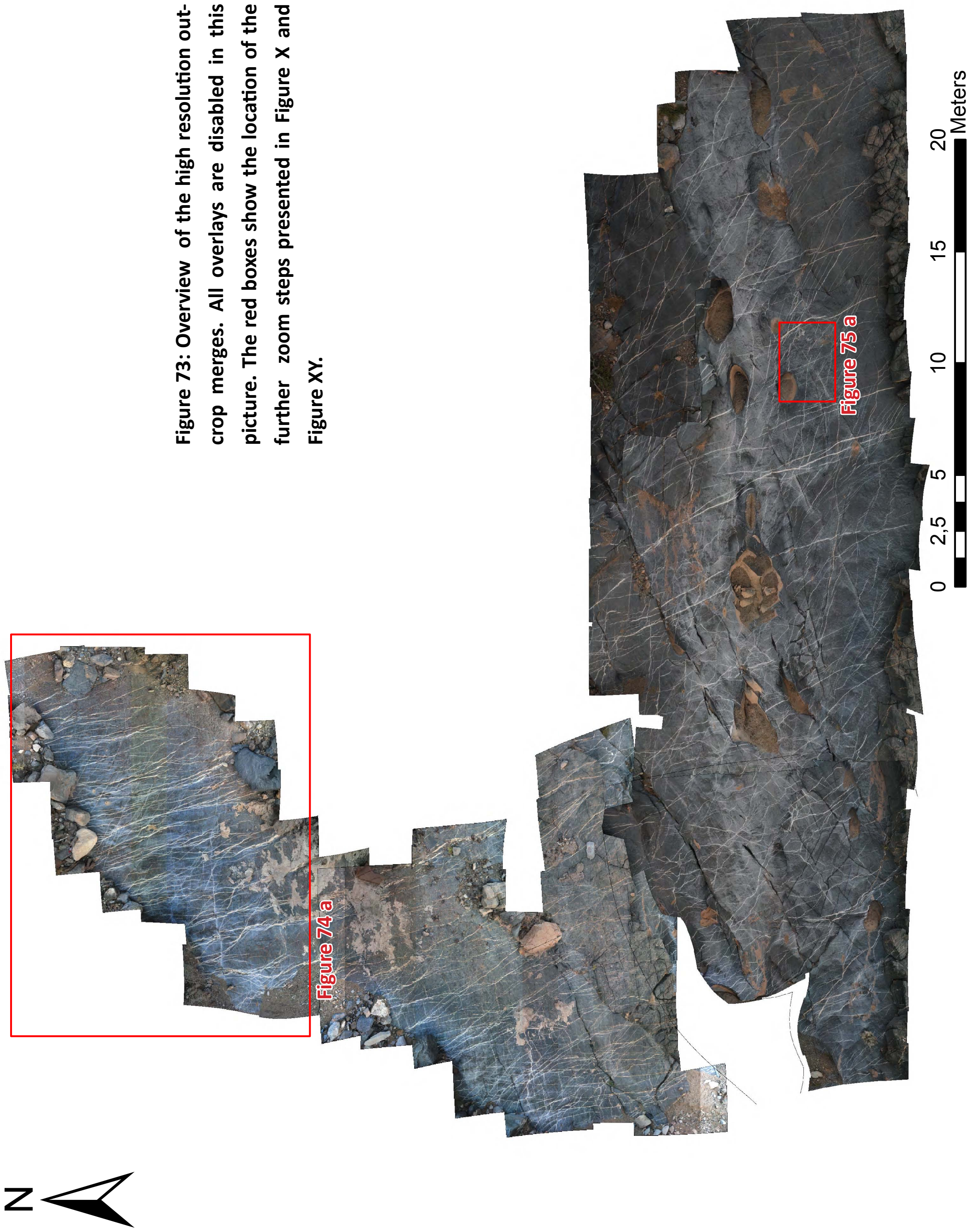

Figure 73: Overview of the high resolution outcrop merges. All overlays are disabled in this picture. The red boxes show the location of the further zoom steps presented in Figure X and Figure XY.

Figure 74a: Zoom at Subset North 1 without overlays. The red box indicates the extent of the next zoom step.

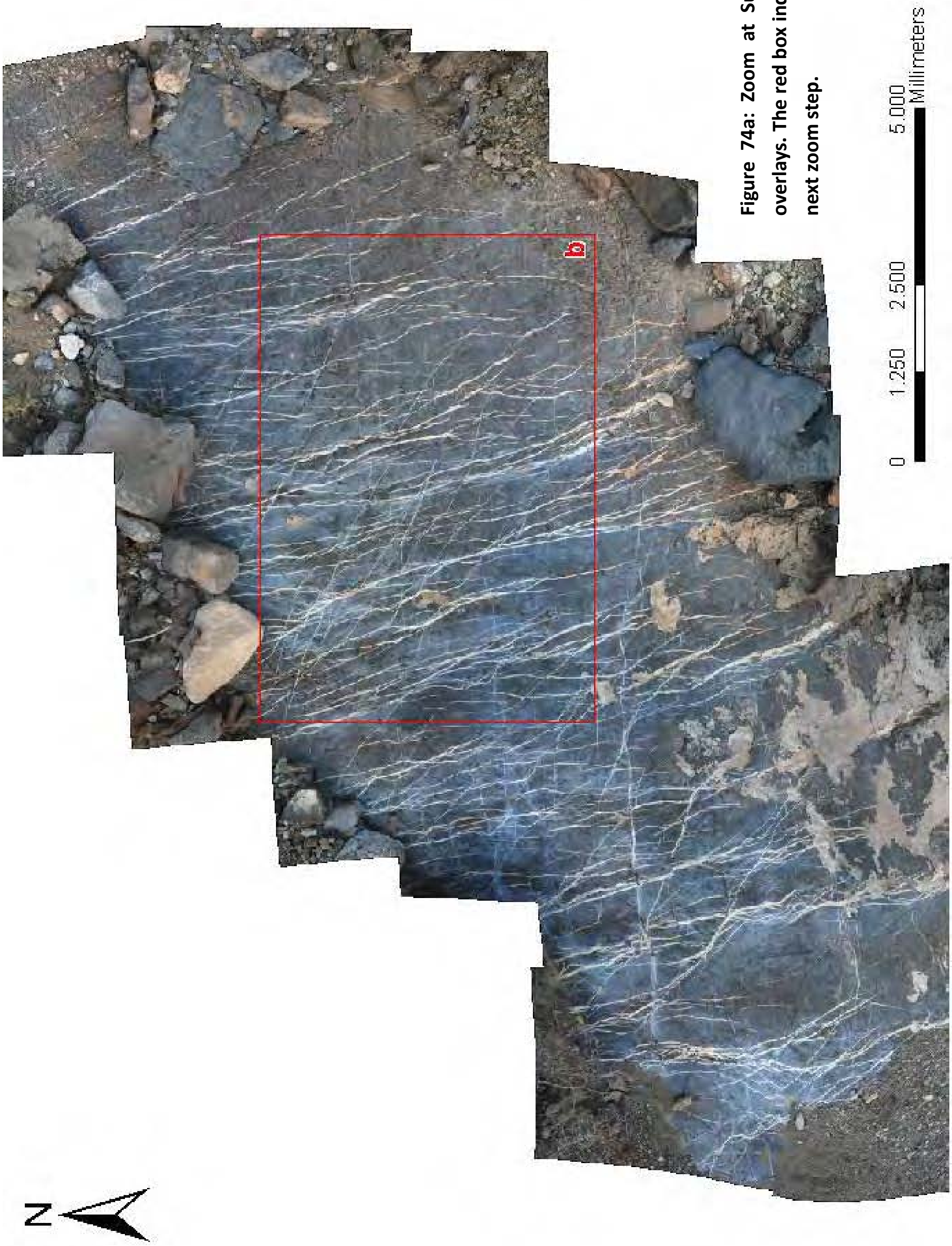

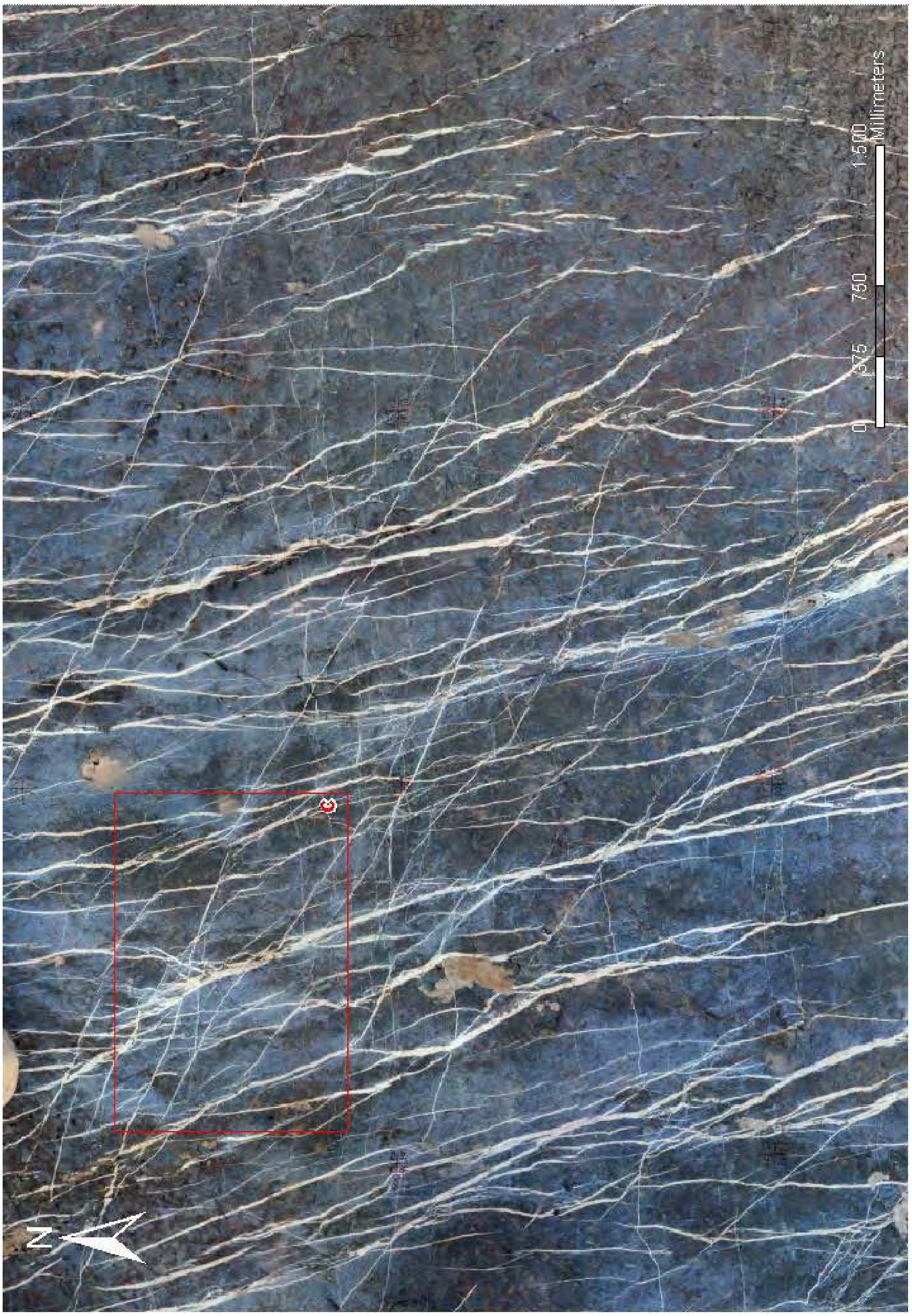

Figure 74b

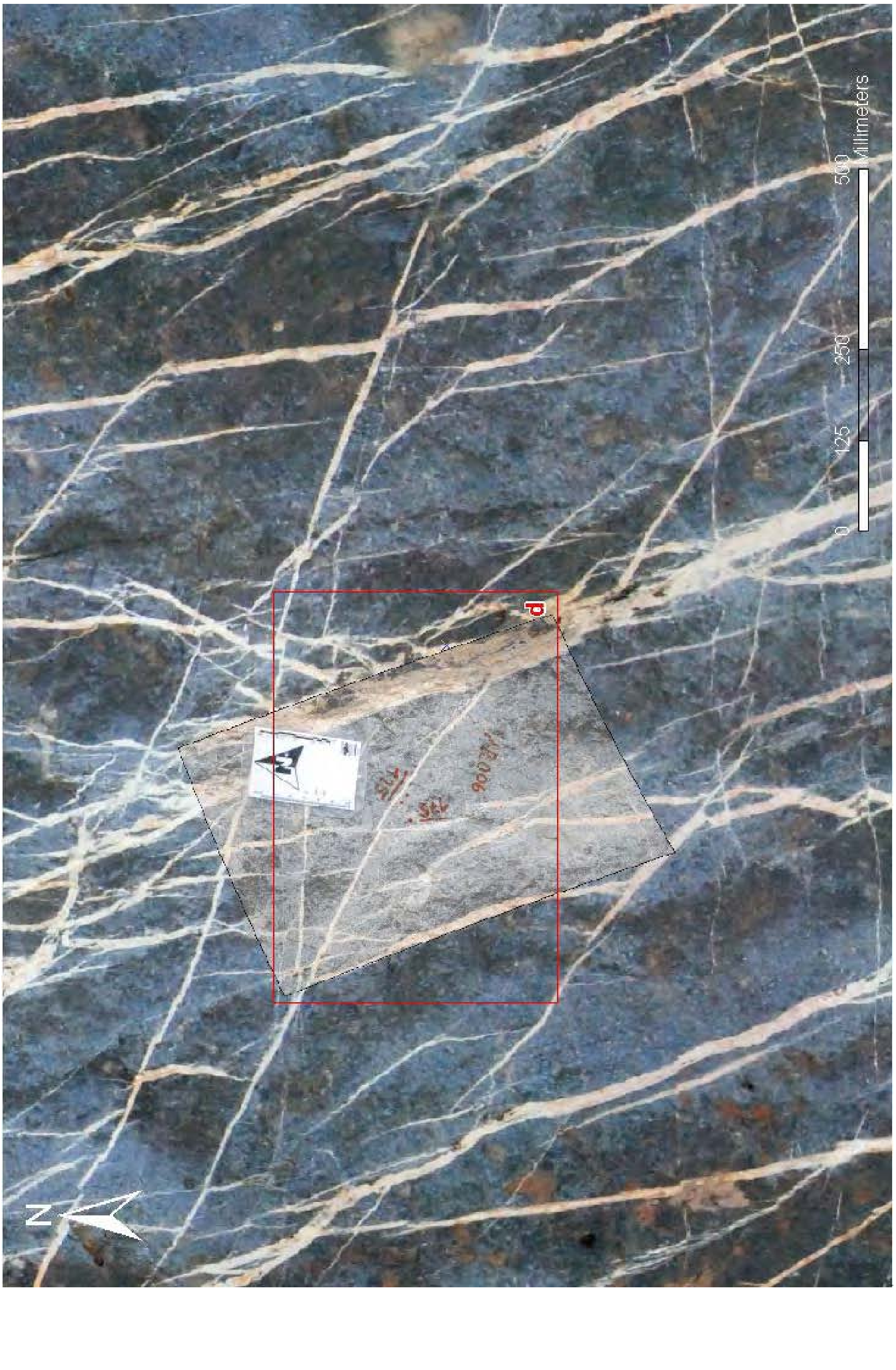

Figure 74c: A Detail image of an age relationship observation is draped on the outcrop that offers an increased resolution in this site.

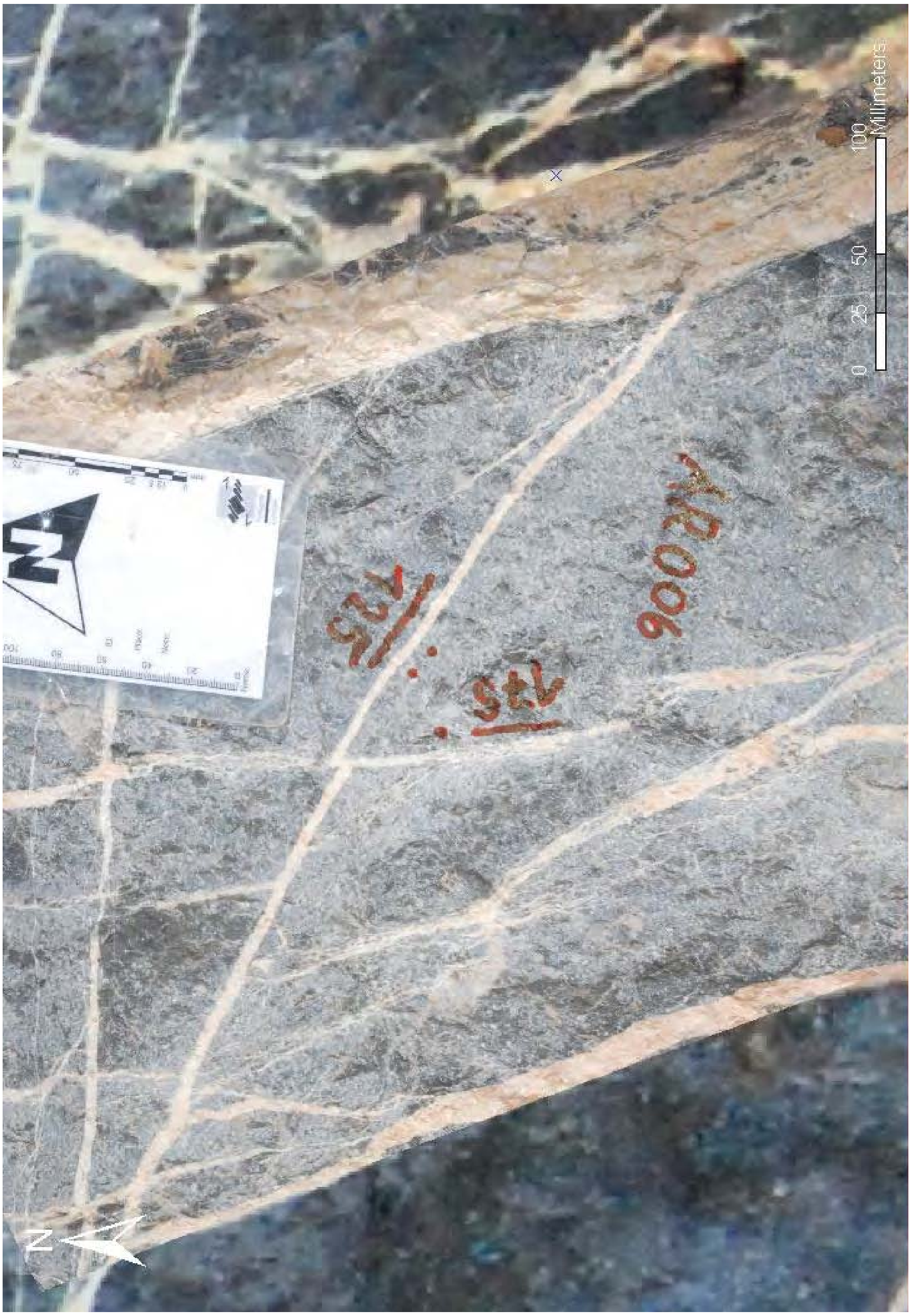

Figure 74d

Figure 75a: Zoom into subset South 2 . Detail images of AR observations and plug sites are overlain. For location see figure XY.

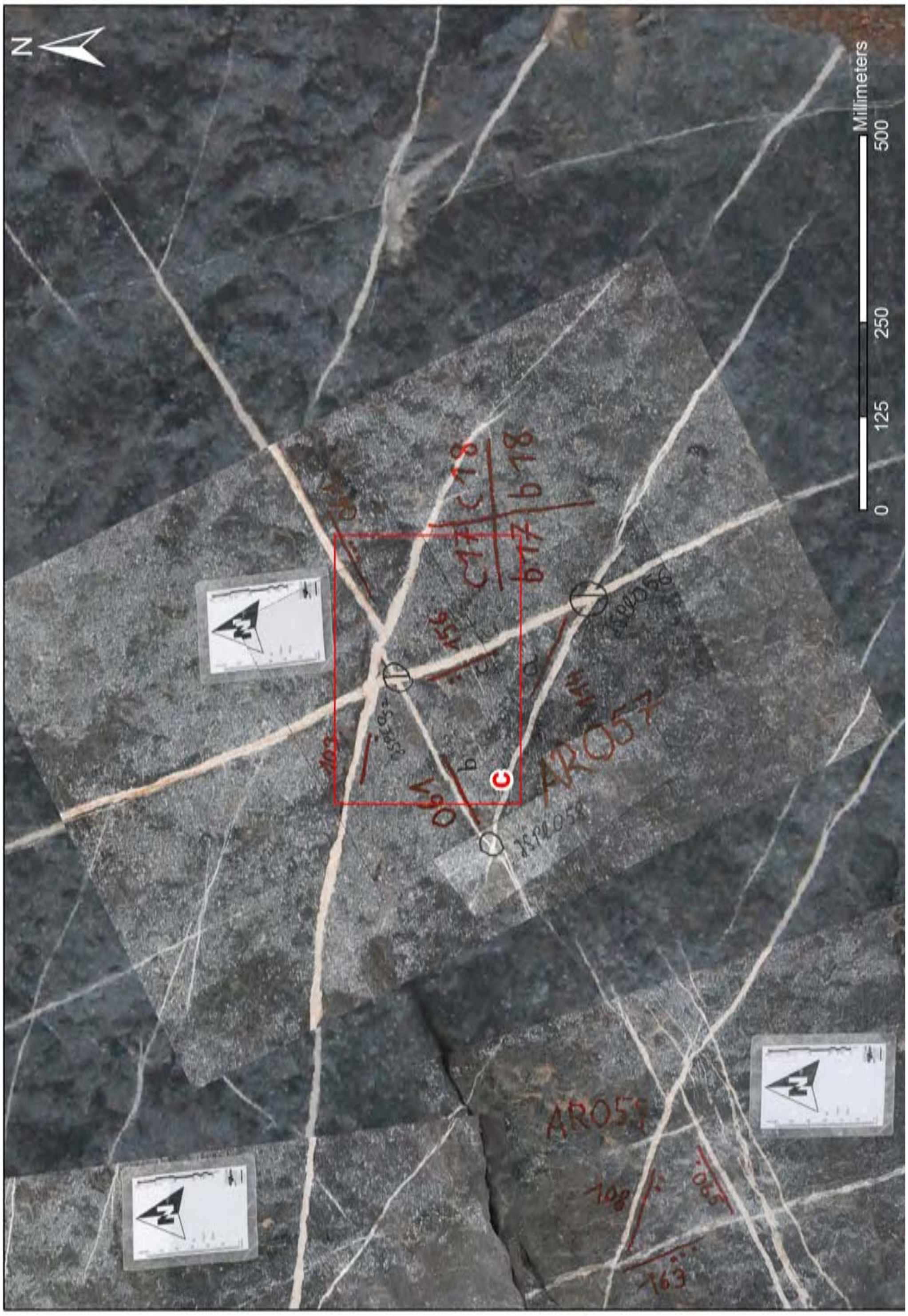

Figure 75b:

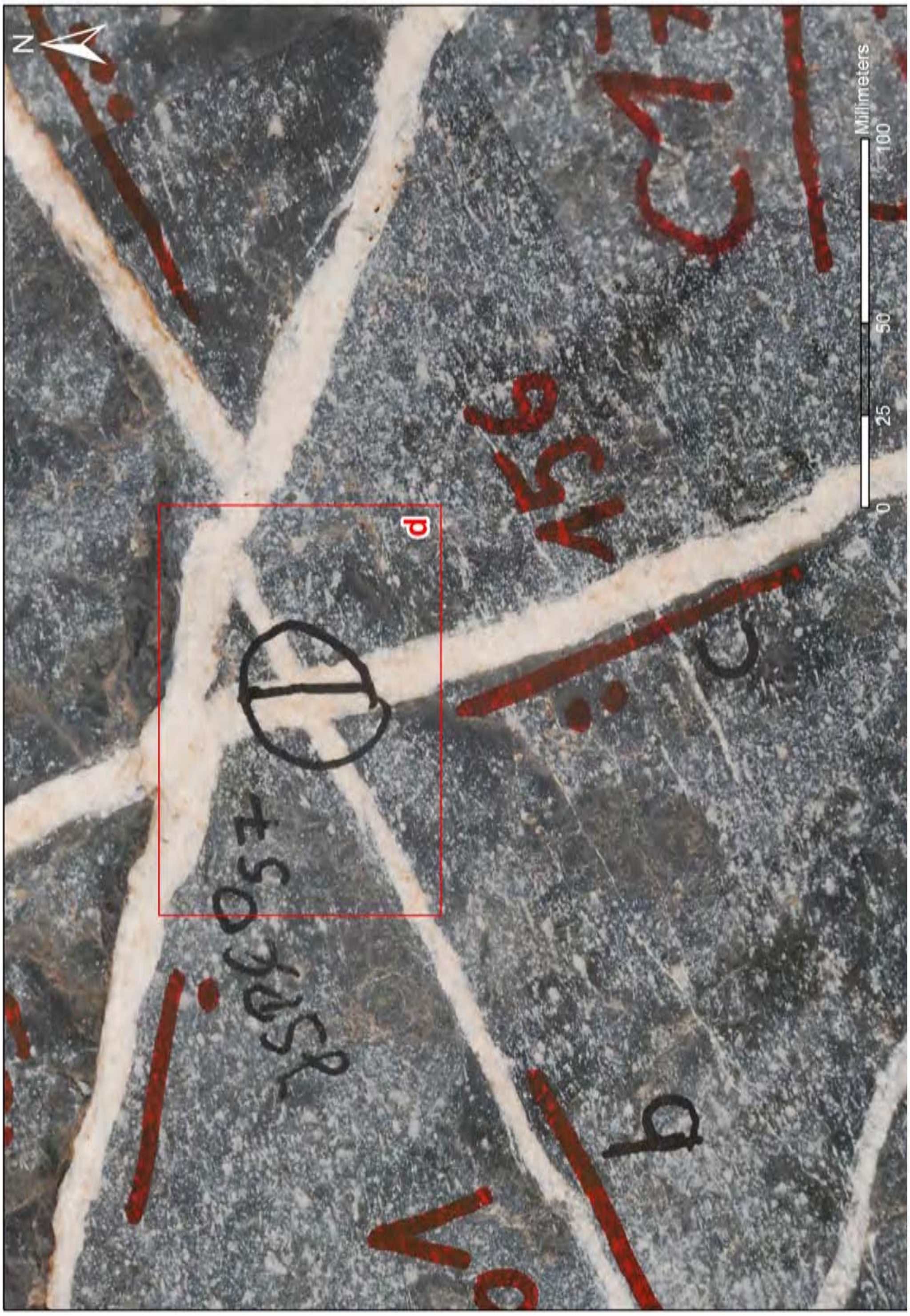

Figure 75c:

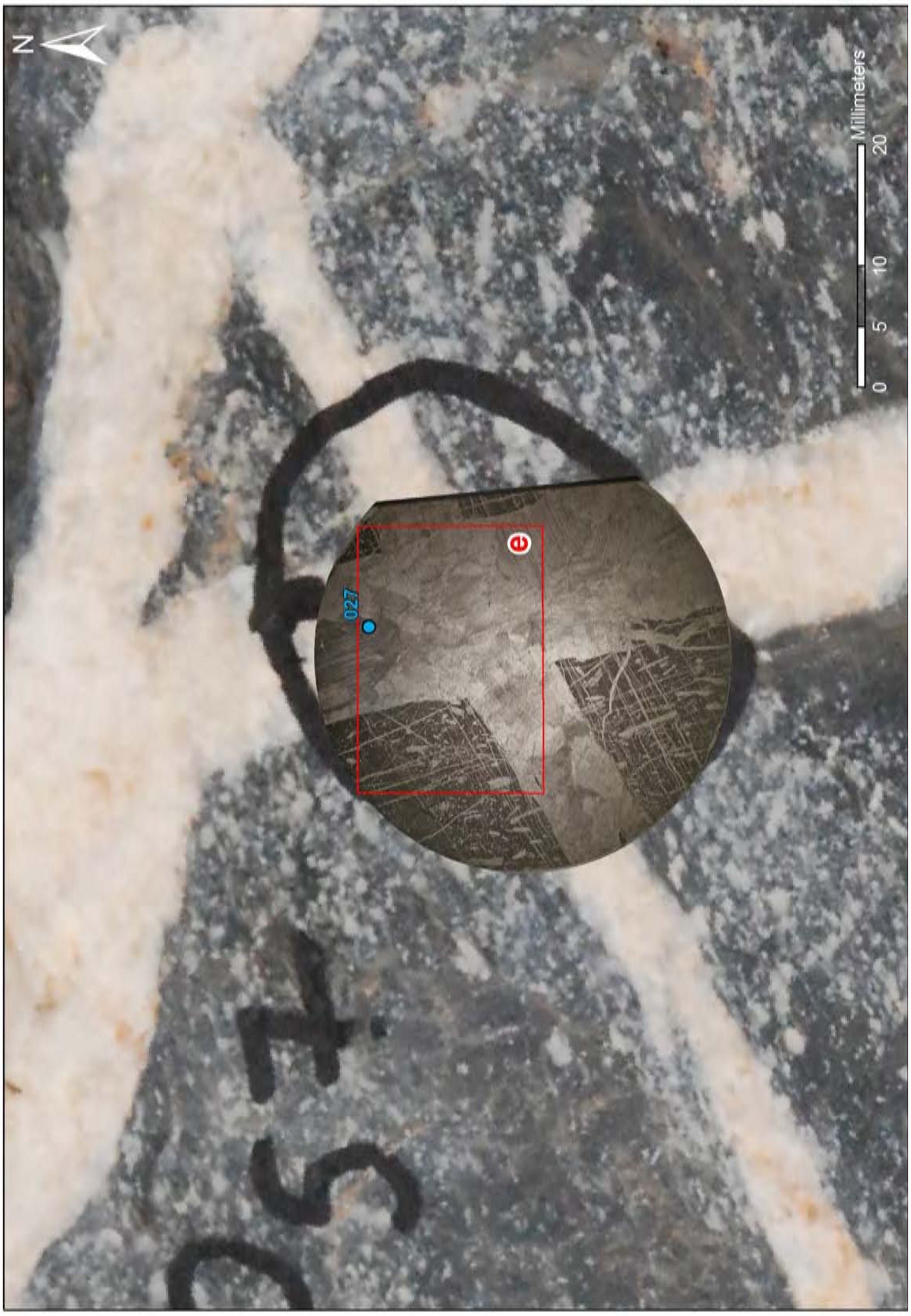

Figure 75d: A thinsection image (plane polarized light) draped on the detail images provides insights into the microstructure at this location

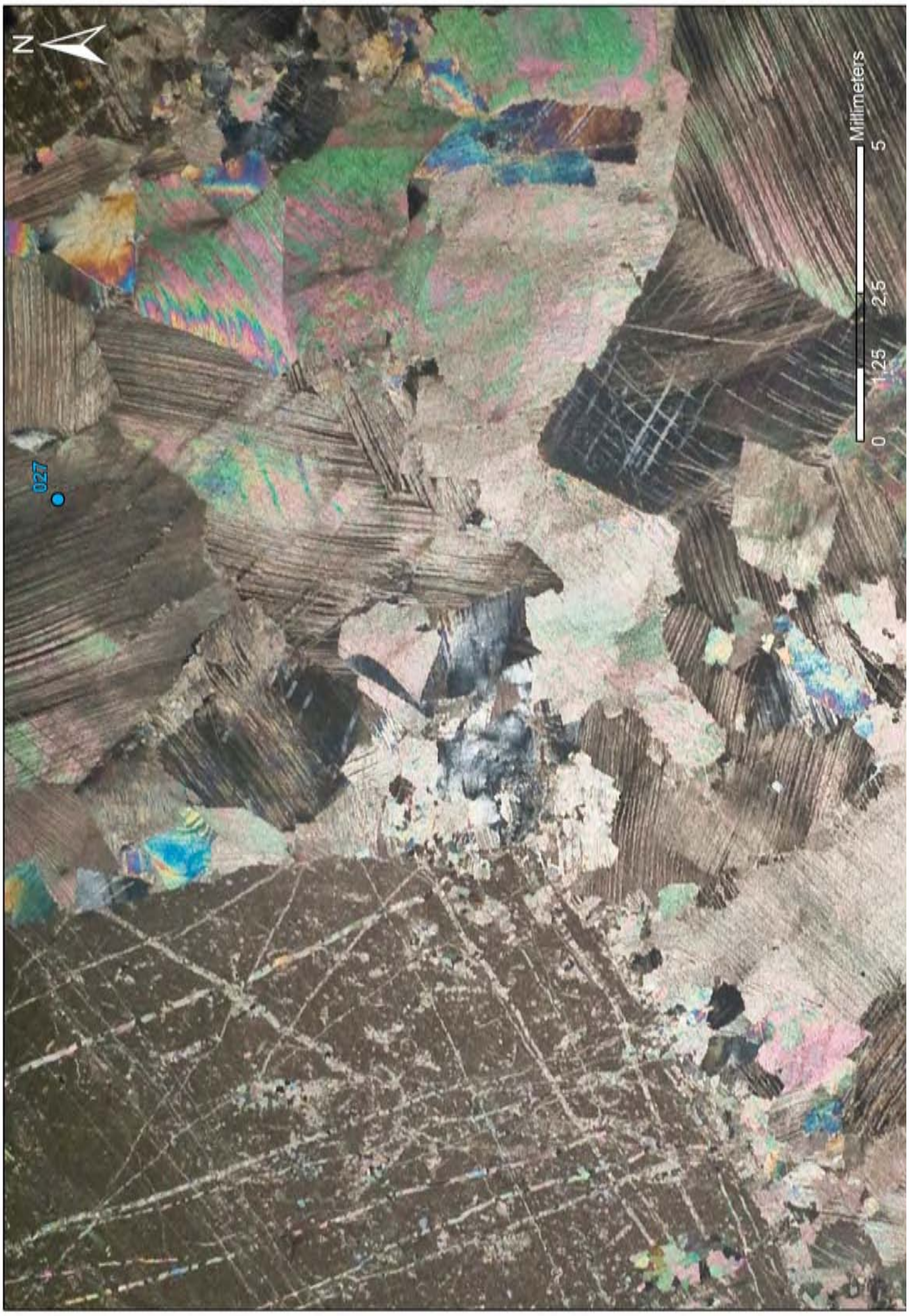

Figure 75e:Zoom into the draped thin section image (crossed polarized light). The blue dot marks the position of a Isotope measurement.

4.2 Evolution of the calcite vein network (Max Arndt & Simon Virgo)

4.2.1 Boundary conditions during the formation of the vein network

Microstructural investigations suggest that each calcite vein visible on meso scale represents not only one fracture event, but several events of fracturing and sealing. The typical vein growth can be described as crack and seal opening indicated by splays and tip splays and most of all by parallel orientated elongated host rock inclusions that are overgrown by single crystals (see Figures: 53 & 54). From these markers an aperture for a single fracture event can be inferred that has the dimension of 100-101µm.

The predominant opening mode throughout the outcrop is mode I dilatant opening. Some veins however show hybrid opening. They usually are part of en-echelon sets.

The formation of mode I dilatational veins necessitates fluid pressure close to lithostatic and low differential stresses (see Figure: 76).

Hybrid veins form in an environment with slightly higher differential stress and lower fluid pressure (see Figure: 76). The state of fluid pressure however must be still close to lithostatic because otherwise the rock would fail in shear fractures without an opening component.

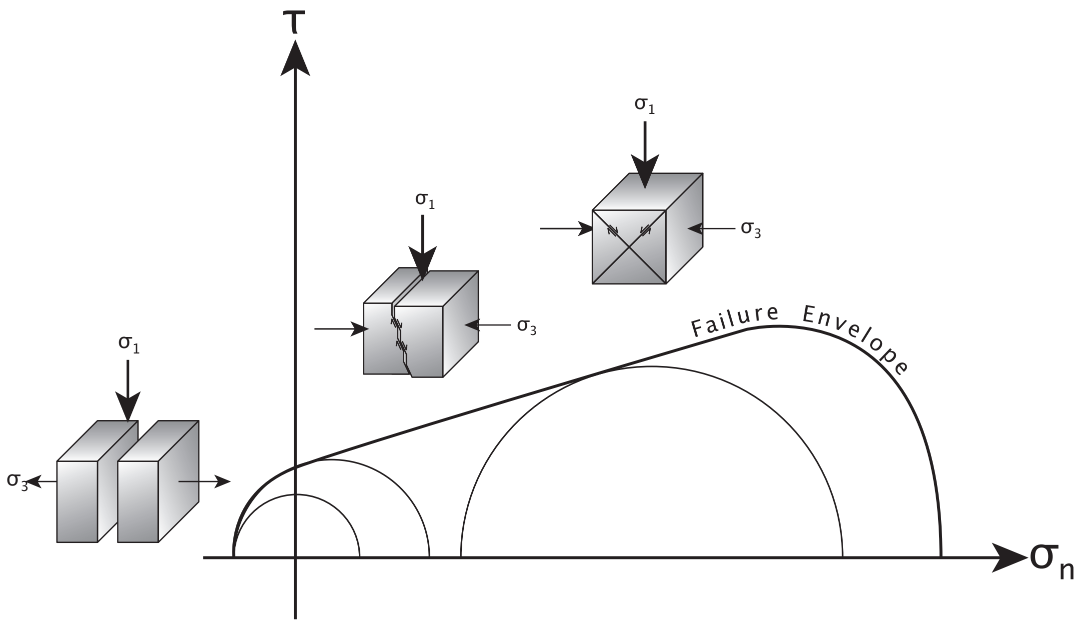

Figure 76: Schematic Mohr-diagram illustrating different stress states for extensional (left), hybrid (center) and shear failure (right).

Veins in the outcrop are always in a steep angle to bedding (close to 90°). Although the strike direction of veins cluster around 160°, 117° and around 80°, veins occur in every intermediate strike direction. This indicates that the orientation of maxi-

mum compressive stress is vertical (σv=σ1) and the direction of minimum compressive stress, as well as the third principal stress direction are horizontal ((σ3≤σ2=σh). The high variability of strike directions show that the stress state was not static but changed in direction during the formation of the vein network.
The mutual age relationships which are observable on micro scale (see Chapter 3.3.5 and Figures therein) and also get reflected in the macroscopic age relationship observations, show that this change in the horizontal stress state occurred several times in the evolution of the vein network.

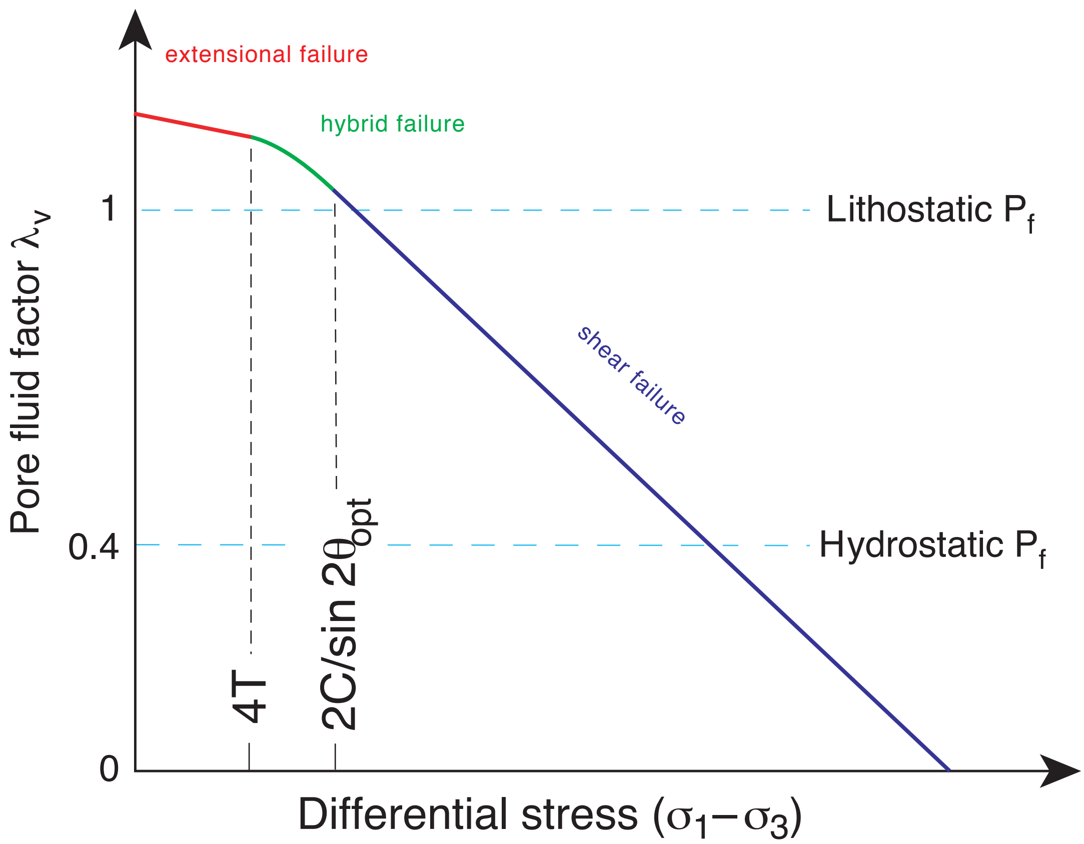

Figure 77: Schematic failure mode diagram in λ-σ space (modified from Cox 2010). Depending on diffential stress and fluid pressures related to overburden stress different failure modes are active. An increase of fluid pressure with constant differential stress will promote extensional failure. A more stress driven path will lead to a shear failure.

A change in the fluid pressure and differential stress state is marked by the shear vein/ incipient fault described in Chapter 3.1.1.1.1: The differential stress is higher than during the formation of the dilatant fractures and hybrid fractures while at the same time the fluid pressure is lower (Figure: 76). σ1 was vertical during the formation of this vein while σ3 was oriented approximately North-South.
A Failure mode diagram in λ-σ space (Cox 2010) can be used alternatively to Mohr diagrams to illustrate the state of stress and fluid pressure that led to the formation

of the 3 different types of veins (Figure 77).
Most veins underwent a certain amount of plastic deformation as indicated by mechanical twinning of the Calcite (see Chapter 3.3.4). The dominating mechanical twins belong to type I and type II twins (Burkhard 1993). Their occurrence and the absence of serrate twin boundaries allow us to roughly estimate the peak temperature of the rock to be around 250°C. Most of the veins already existed when this temperature was reached or were formed at this temperature.
However, one type of veins is lacking mechanical twinning (juvenile veins, see chapter 3.3.4). These veins are therefore younger that the majority of the veins of the network, because they formed after the rock has left the stress and temperature conditions that caused twinning and are accordingly free of deformation twins.
The temporal relationship between the incipient fault and the juvenile veins could not be ultimately clarified.

4.2.2 **Implication on vein growth and vein-vein interaction**

Veins are not only cross cutting each other but also attracted towards each other. This is strongly suggested by observed aligning and stacking of veins. Mechanical strength ratios between host rock, cement and interface as well as the misorientation of an old vein towards the favorable orientation of a new fracture likely are controlling factors. A weak interface and a small angle of a new crack approaching an older vein promote a reactivation of the older fracture plane that increases the total aperture but not imperatively the total length of the vein. A mechanically more competent interface and a higher misorientation angle do support the cross cut of a younger crack through an older one.
Observations show that veins can intersect older veins at very low angles. Furthermore it occurs that parallel veins are closely spaced without showing signs of reactivation (for example arrays). This suggest that the strength of the vein fill and the interface is also a function of time: a completely sealed vein gets less likely reactivated than a vein that has not yet completely restored its strength by filling up with calcite and gluing the host rock walls together.
Differing nucleation and propagation characteristics of new cracks (e.g. crack speed) as well as anisotropies introduced by the growth of stylolites can be additional reasons for the high variability of vein interaction structures.
Every vein and every stylolite seam that forms in the host rock introduces a new anisotropy in the volume that has influence on the localization and behavior of following fractures. The overall anisotropy and complexity of the system therefore grows with ongoing deformation.

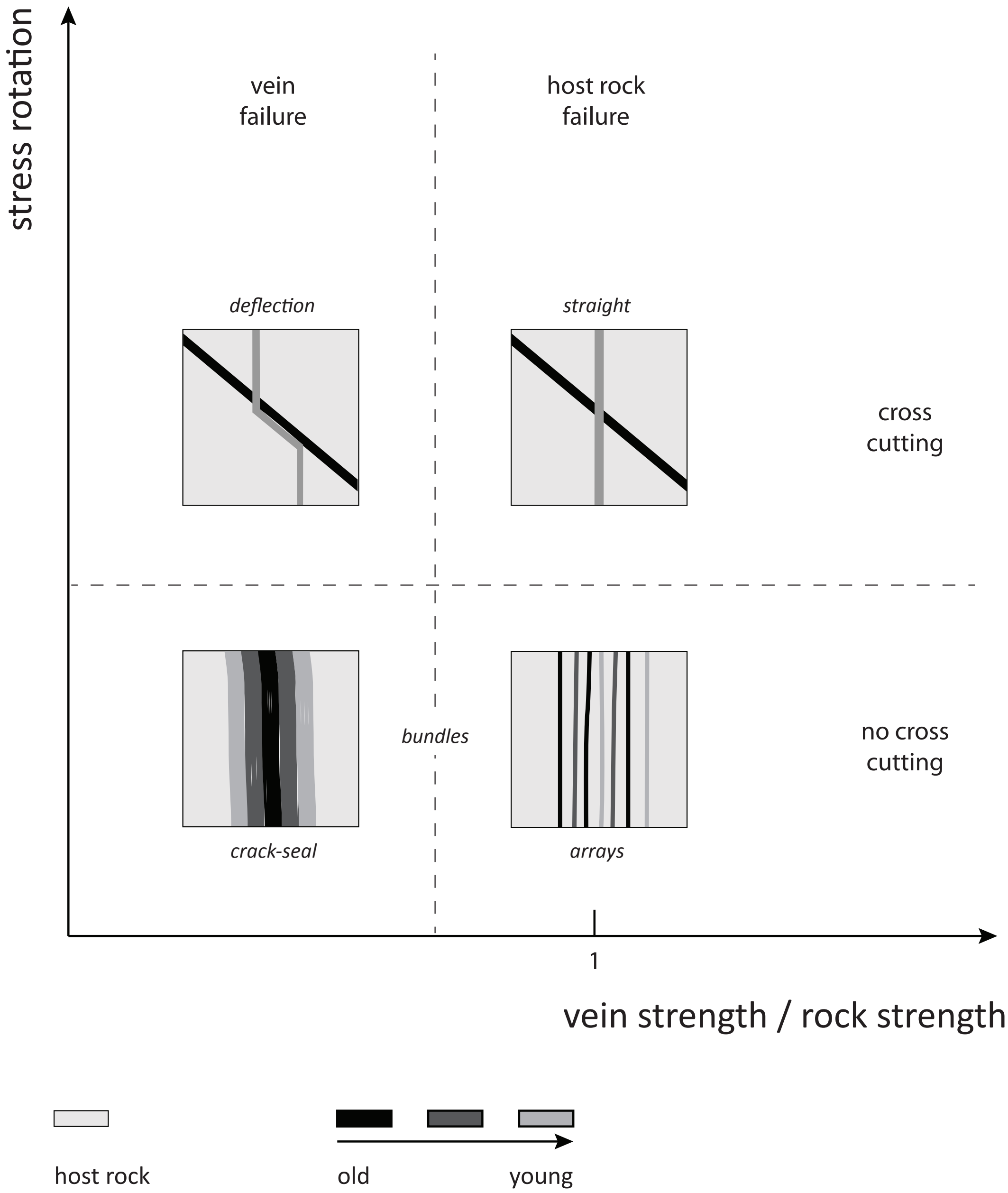

Figure 78: Schematic diagram how vein strenght and stress rotation control the geometry of vien interaction. If the direction of principal stresses is stable, vein strength ratio controls wether the vein is reopened (crack-seal), or a new vein forms (arrays). We suspect bundles to represent the transition between the crack-seal veins and arrays. If the direction of principal stresses changes, vein strength ratio controls whether a new fracture (vein) is temporarily deflected by an existing vein or it will cross cut the existing vein without any change in direction

4.2.3 **Fluid flow evolution model**

The most conspicuous observation that we made from the stable isotope analysis is that the host rock is highly depleted in oxygen (see figure 61) compared to the host rock values of Hilgers and Holland (Hilgers et al. 2006, Holland & Urai in press) as well as compared to the global values for carbonate rocks of upper cretaceous age (Veizer & Hoefs 1976).

The host rock samples in the studies of Hilgers and Holland were taken from deeper in the stratigraphy of the autochthonous carbonate sequence and match in general with the global isotopic signature for carbonate rocks of this age (Hilgers et al. 2006, Holland & Urai in press, Veizer & Hoefs 1976).

We explain this depletion in δ 18O by an alteration of the whole rock mass by external fluid with a light oxygen isotopy within the early tectonic history of the rocks (see Figure 79 b). Since the host rock values of Hilgers and Holland show no sign of such an alteration deeper within the carbonate system, we can assume that our sampling location is more proximal to the source of the external fluid, sequentially that the fluid was coming from higher in the stratigraphy.

The stratigraphic position of our outcrop is at top of the autochthonous Natih A formation, which is unconformably overlain by the semi autochthonous Muti formation and the thrust contact of the overriding Hawasina nappe respectively (see chapter 1.2). Both Muti formation and Hawasina nappes are possible sources for oxygen-depleted fluids.

An increased fluid flow is necessary to enable fluid-rock interaction (Cox 2007). Therefore the permeability of the rock mass had to be high during the alteration of the host rock.

This could be either explained by a high primary porosity due to poor compaction in this stage of the tectonic history, or by a high permeability enabled by an interconnected fracture pattern in a low-permeability matrix. The second possibility requires either high fluid pressure or high differential stresses to allow such networks to form. High fluid pressures promote the opening of dilatant fractures while under high differential stresses conjugate shear fractures can form. Both are capable to enhance permeability and both stress/ fluid pressure situations might have prevailed during the emplacement of the Hawasina and Sumail nappes.

Alteration of the isotope composition of the wall rock around fractures is limited to a halo of several mm (Cox 2007). The very high density of microveins that is ubiquitously observable in the thin sections can possibly explain the alteration of the entire host rock by fracture controlled fluid flow. Both explanations for an enhanced permeability are therefore possible.

Another possible explanation for the depletion of the rock mass in terms of its Oxygen isotopy is that the rocks were subaerially exposed before they were overridden by the Hawasina. A subaerial exposure, caused for example by a sea level drop, would allow the infiltration and alteration of the rocks by meteoric waters.

Which of these possible scenarios for the depletion in δ 18O apply for our outcrop could not be clarified in this study.

The next phase of the structural evolution of our outcrop is characterized by extensive veining. Veins are usually suborthogonal to bedding and occur in any strike direction. The mutually behaving overprinting relationships and crack seal textures in mostly dilating veins are indicative for episodic fracturing events under near lithostatic fluid pressures with a vertical σ1 and a highly variable orientation of the horizontal stress field (see also Chapter 4.2.1).

The isotopic composition of the veins is rock buffered, which means that it is in equilibrium with the isotopic composition of the depleted host rock (figure 79 c). The calcite precipitating fluid is therefore not advected from an external source but the rock mass is hydraulically isolated. We assume that the fluids oversaturation in calcite is maintained by the growth of stylolites, which is contemporary with vein formation, as we demonstrated in chapter 3.3.9.

A high number of veins show a significant drop in δ 13C values, while their oxygen isotope ratio stays in equilibrium with the host rock. This deviation can be explained by infiltration of light oxidized hydrocarbons (Methane and Ethane) into the system (Barker et al. 2006)(Figure 79 d).

The last structural event, as we can interpret it from our stable isotope data, is the opening of the system to an external fluid. It is characterized by a rise in δ 18O towards values of 26,18. This isotopy is in much better accordance with the measurements of Hilgers and Holland (Barker et al. 2006, Hilgers et al. 2006, Holland & Urai in press). The source of the fluid is interpreted to be carbonates from deeper in the autochthonous sequence, which were not altered by an external fluid in the first place (figure 79 e). The veins comprising this isotope signature are striking approximately E-W and are consistently younger than any other strike direction they intersect. They furthermore show evidence for a vertical shear component. Their strike directions match the common orientation of normal faults on the southern slope of the Jabal Akhdar (Holland et al. 2009a, Holland et al. 2009b). These Faults were already interpreted by Hilgers to mark the transition from a closed (Rock buffered) to a more open fluid system (Hilgers et al. 2006) (figure 79 e).

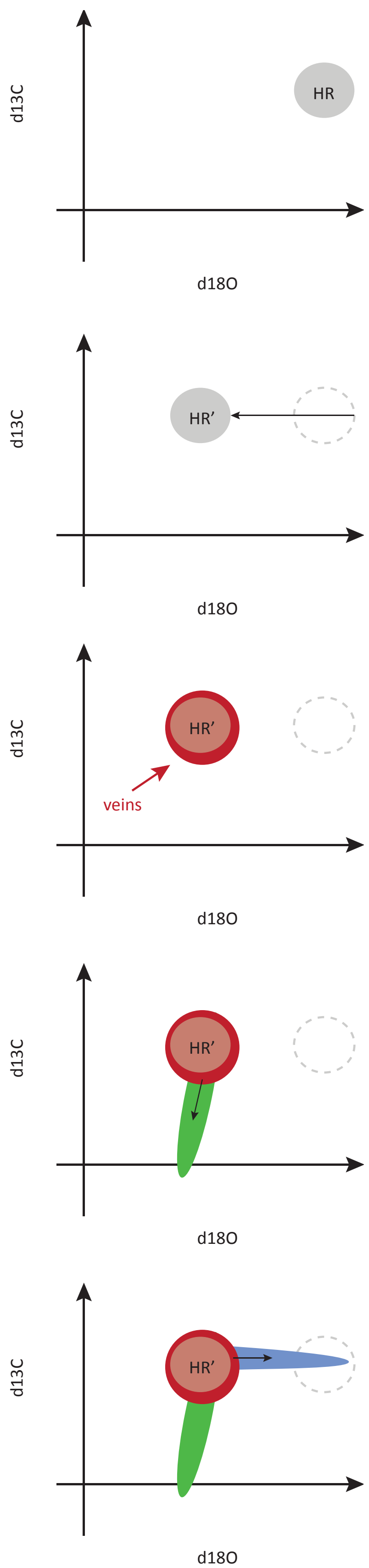

a. Deposition of Natih A limestones with a isotopy acording to the global isotopy for proximal limestones during Turonian time

b. Extensive alteration of the hostrock by an oxygen depleted fluid, likely induced by Ophiolite obduction

c. Formation of rock buffered calcite veins (red) in a closed fluid system

d. Infiltration of oxidized hydrocarbons leads to low d13C values in vein calcite (green)

e. Normal faults unlock the fluid system. Fluids from deeper stratigraphic levels seal fault related veins (blue) with a heavier d18O isotopy than the alterated hostrock

Figure 79: Illustration of the fluid flow model

4.3 Outlook (Simon Virgo)

The intention of this thesis is to provide an overview over the dataset we created and present some basic interpretation we made based on this data.

We do not make the claim for our interpretations or observations to be complete! We are convinced that a lot of questions can be addressed to this dataset and can be solved, be it by simple direct observations or sophisticated data mining. Even if a question might not be solvable directly by the given information, the character of the dataset allows identifying places in the outcrop that might bear the solution to this certain question and sample it well directed. The georeferenced framework allows to integrate all kinds of data (for example cathodoluminescent on thin sections, vein density distribution plots, orientation data of stylolites, etc…) without loosing its ability to be browseable and easy to overlook.

In the context of understanding the dynamics of high pressure cells and the evolution of crack seal textures this dataset can provide a valuable natural reference to compare analogue experiments and numerical simulations with. Future research will focus on identifying and quantifying the relevant processes in the evolution of such systems and will also hopefully provide new insights on the regional evolution of the Jabal Akhdar mountain range.

Beside analogue experiments and computer simulations we also see a big potential in the application of new visualization techniques. For example brittle failure mode diagrams in pore fluid factor-differential stress space can be used to infer pathways for differential stresses and fluid pressures that may act to create such complex vein networks as well as crack seal textures. How the growth of fractures, veins and also stylolites affect the boundary conditions such as the local stress, fluid pressure, permeability or saturation state of the fluid as well as what influence those features have as anisotropies to the evolution of the system might be questions worth thinking about.

4.3.1 Improvement suggestions for image acquisition workflow

During the work on the image data of the pavement we gained a lot of knowledge about the strength and weaknesses of our approach. If one decides to apply the presented technique to another outcrop we suggest considering the following improvements in the following chapters.

4.3.1.1 Stationary camera based image acquisition

We suggest to use a stationary camera based image acquisition, wherever the terrain around the outcrop offers an elevated site that allows taking photos of the outcrop with not too high off nadir angles. The biggest advantage of this method towards the dipod approach is, that the parallax effect is not an issue anymore and therefore the panorama can be created with a much higher accuracy.
The greater distance to the outcrop has to be countered with a suitable lens (For example a telephoto lens with 400mm focal length) to achieve the desired resolution. Further advantages of this method are that one has not to worry about drop shadows and that the image acquisition can be carried out much faster.

4.3.1.2 Dipod based stereo image acquisition

Rather than eliminating the parallax effect to achieve better results in the panorama creation it can be used to gain information about the topography of the surface. The technique this approach is based on is called stereo photogrammetry. There are several commercial software products available, which are capable to create digital surface models from image pairs that cover the same area from 2 slightly different directions. Orthorectified imagery can be created from the image pairs by using the 3 dimensional information derived from the parallax shift of features in the image pairs. Orthorectified tiles can be stitched to a large panorama simply by relocation, since lens distortion and parallax effects are already eliminated by the orthorectification.
Besides the parallax effect, the dipod based stereo image acquisition shares all disadvantages of the image acquisition approach used in this study. It is furthermore likely more time consuming, since twice as many pictures have to be shot, and the processing Workflow is more complex.

4.3.1.3 Airborne methods

The Dataset we like to create is meant to be similar to aerial imagery but with a smaller area of coverage and much higher resolution. It is therefore worth thinking about an image acquisition from a flying vehicle.
Within the last years small unmanned aerial vehicles (UAVs/drones) with 4 to 8 rotors (microcopter, quadcopter, hexacopter, octocopter) have become technically mature

and affordable and are nowadays used for a variety of remote sensing and surveillance applications in science, industry and military (Eisenbeiss 2009). Guided by GPS, barometric sensors and accelerometers (Inertial navigation system), commercially available drones are capable to autonomously follow an assigned route and take overlapping photographs that can be used for high resolution remote sensing.

4.3.1.4 Improvement of the gridding method

The result of the gridding, as we carried it out in this study, is a surface projection of a 2 m spaced orthogonal grid parallel to the mean orientation of the outcrop surface (in our case: 256/15).

Using a surface parallel reference plane is useful, because its distance to the surface does not grow too large and the error in projecting the grid points remains small (See Chapter 2.1.5.1.1.).

However if the dip of the surface is small, it is more convenient to choose a horizontal reference plane, since this makes the strike correction obsolete.

In any case we suggest to measure and store the distance of every projected grid point to the reference frame. Together with the orientation of the reference plane this can be used to create a (coarse) 3 dimensional surface model that for example can be used to test the validity of the 3d information provided by stereoscopic imaging (Chapter 5.1.1.2 and 5.1.1.3).

5 Conclusions

High resolution outcrop panoramas bridge the gap between satellite based remote sensing and fieldwork. Integrated in a GIS system they are a powerful tool to link observations and measurements on different scales.

The investigated vein network consists of subvertical, mostly dilational calcite veins that can be observed in any strike direction. They show mutual age relationships on macroscopic and microscopic scale. They formed under near lithostatic fluid pressure with a vertical σ_1 and a highly variable horizontal stress field.

The preserved fracture network does not represent a single opening event. host rock inclusions and vein interactions proof a dynamically evolving system, growing in a crack-seal manner.

The high diversity of vein characteristics and vein interaction structures are evidence for discontinous boundary conditions during the evolution of the vein network. Existing veins act as anisotropies depending on orientation and their sealing driven strength regeneration. They significantly influence the formation of new fractures.

Stylolite grow and formation is contemporaneous with vein formation. They maintain calcite oversaturation during the rock buffered stage of veining and can be regarded as chemical and mechanical anisotropies.

Stable Isotope values of the limestone host rock do not fit with data of previos work and literature data. The investigated rocks were altered by an external fluid prior to the formation of the vein network.

Most veins are host rock buffered. The low d13C values of some veins can relate to a infiltration of oxidized hydrocarbons. High d18O value occur in normal fault related veins.

The isotopic variability across one vein is comparable to the isotopic vaiation over the whole outcrop. this indicates episodic fluidflow in which some veins are preferentially reactivated and act as a pathway for various fluids with different chemistry.

6 Acknowledgements

We would like to thank our supervisor Janos Urai for the opportunity to conduct fieldwork in the Oman Mountains. He is thanked for his patience during the long time of the thesis' preparation and for keeping up our enthusiasm.

Werner Kraus' technical expertise has been very helpful in many ways. He supported us during fieldtrip preparation, outcrop gridding and sample preparation. We would like to thank Zoé Sobisch for her accompany and patience during our time in Al Hamra. Christoph Hilgers is thanked for co-supervising this thesis and for many discussions on the structural evolution of the Jabal Akhdar Anticline as well as his hospitality in Muscat.

Marc Holland is thanked for introducing us to the geology of the Oman Mountains and his advice on safety, fieldwork and infrastructure in Oman.

We spend a productive time with Steven Cox both in the field and in Canberra. He not only provided lab-time for stable isotope measurements, but also gave us very informative lectures on fluid flow and reactive transport modeling. The fruitful discussions on the fluid flow history of our outcrop are appreciated. Paul Stenhouse is acknowledged for being an excellent host in Canberra. He introduced us to stable isotope geology and made us familiar with sample preparation. It has been a pleasure to share the time with him during field seasons 2009 and 2010. Jo Cali's support as technical advisor for the mass spectrometer in Canberra has been appreciated.

The locals Sulaiman Al Abri and Amer Al Abri are acknowledged for their unmatched hospitality, support and help in many ways.

We would like to thank the German University of Technology, Muscat, especially Manuela Gutberlet for her introduction to the people in Al Hamra and Hussain Al Balushi, who organized visas and shipped our samples to Aachen.

Steffen Abe is thanked for his careful language review and discussions. Joyce Schmatz' help and advice on doing microscopy and interpreting microstructures has been appreciated.

We are grateful to Franz Grümmer, who designed and constructed the camera stand (dipod). Philippe Razin is thanked for his notice on the stratigraphic localization of the investigated outcrop. We would like to thank the company Gabriel OHG and especially Rainer Basner for his consultancy concerning the drilling setup.

This thesis was funded by the German Society for Petroleum and Coal Science and Technology (DGMK Project 718, dynamics of veins).

7 References

Adobe. 2007. Photoshop CS3 Extended, San Jose, California, U.S., Adobe Systems.

AutopanoWiki. 2007. Understanding Projection Modes. http://www.autopano.net/wiki-en/action/view/Understanding_Projecting_Modes.

AutopanoWiki. 2008. Interpolation and blenders. http://www.autopano.net/wiki-en/action/history/Interpolation_and_blenders.

AutopanoWiki. 2009a. Control Points Editor. http://www.autopano.net/wiki-en/action/view/Control_Points_Editor.

AutopanoWiki. 2009b. Render Settings. http://www.autopano.net/wiki-en/action/view/Render_Settings.

Barker, S. L. L., Cox, S. F., Eggins, S. M. & Gagan, M. K. 2006. Microchemical evidence for episodic growth of antitaxial veins during fracture-controlled fluid flow. *Earth and Planetary Science Letters* **250**(1-2), 331-344.

Bernecker, M. 2007. Facies architecture of an isolated carbonate platform in the Hawasina Basin; the Late Triassic Jebel Kawr of Oman. *Palaeogeography, Palaeoclimatology, Palaeoecology* **252**(1-2), 270-280.

Breton, J.-P., Bechennec, F., Le Metour, J., Moen-Maurel, L. & Razin, P. 2004. Eoalpine (Cretaceous) evolution of the Oman Tethyan continental margin; insights from a structural field study in Jabal Akhdar (Oman Mountains). *GeoArabia [Manama]* **9**(2), 41-58.

Burkhard, M. 1993. Calcite Twins, Their Geometry, Appearance and Significance as Stress-Strain Markers and Indicators of Tectonic Regime - a Review. *Journal of Structural Geology* **15**(3-5), 351-368.

Cali, J. A. 1997. Explanatory Notes for data from the Finnigan MAT 251 and Kiel Device. Research School of Earth Sciences, Australian National University.

Coplen, T. B. 1988. Normalization of oxygen and hydrogen isotope data. *Chemical Geology; Isotope Geoscience Section* **72**(4), 293-297.

Cox, S. F. 2007. Structural and isotopic constraints on fluid flow regimes and fluid pathways during upper crustal deformation: An example from the Taemas area of the Lachlan Orogen, SE Australia. *Journal of Geophysical Research* **112**, 23 PP.-23 PP.

Cox, S. F. 2010. The application of failure mode diagrams for exploring the roles of fluid pressure and stress states in controlling styles of fracture-controlled permeability enhancement in faults and shear zones. *Geofluids* **10**(1-2), 217-233.

Dunham, R. J. 1962. *Classification of carbonate rocks according to depositional texture*. American Association of Petroleum Geologists : Tulsa, OK, United States, United States.

Eisenbeiss, H. 2009. UAV photogrammetry. Unpublished Dissertation thesis, ETH Zürich.

ESRI. 2004. ArcMap 9.3. In: *ArcInfo Desktop 9.3*. ESRI, Redlands, California, U.S.

Filbrandt, J. B., Al-Dhahab, S., Al-Habsy, A., Harris, K., Keating, J., Al-Mahruqi, S., Ozkaya, S. I., Richard, P. D. & Robertson, T. 2006. Kinematic interpretation and structural evolution of north Oman, Block 6, since the Late Cretaceous and implications for timing of hydrocarbon migration into Cretaceous reservoirs. *GeoArabia [Manama]* **11**(1), 97-140.

Friedman, I., O'Neil, J. & Cebula, G. 1982. Two New Carbonate Stable Isotope Standards. *Geostandards Newsletter* **6**(1), 11-12.

GeoEye. 2009. GeoEye-1 Fact sheet. GeoEye, Dulles, Virginia.

Glennie, K. W. 2005. *THE GEOLOGY OF THE OMAN MOUNTAINS An outline of their origin*. Scientific Press Ltd, Beaconsfield.

Hilgers, C., Kirschner, D. L., Breton, J. P. & Urai, J. L. 2006. Fracture sealing and fluid overpressures in limestones of the Jabal Akhdar Dome, Oman Mountains. *Geofluids* **6**(2), 168-184.

Holland, M., Saxena, N. & Urai, J. L. 2009a. Evolution of fractures in a highly dynamic thermal, hydraulic, and mechanical system; (II), Remote sensing fracture analysis, Jabal Shams, Oman Mountains. *GeoArabia [Manama]* **14**(3), 163-194.

Holland, M. & Urai, J. L. in press. Evolution of anastomosing crack-seal vein networks in limestones: Insight from an exhumed high-pressure cell, Jabal Shams, Oman Mountains. *Journal of Structural Geology* **In Press, Corrected Proof**.

Holland, M., Urai, J. L., Muchez, P. & Willemse, J. M. 2009b. Evolution of fractures in a highly dynamic thermal, hydraulic, and mechanical system; (I), Field observations in Mesozoic carbonates, Jabal Shams, Oman Mountains. *GeoArabia [Manama]* **14**(1), 57-110.

Homewood, P., Razin, P., Grelaud, C., Droste, H., Vahrenkamp, V., Mettraux, M. & Mattner, J. 2008. Outcrop sedimentology of the Natih Formation, northern Oman; a field guide to selected outcrops in the Adam Foothills and Al Jabal al Akhdar areas. *GeoArabia [Manama]* **13**(3), 39-39.

Kolor. Autopano Giga 2. Kolor, Challes-les-Eaux, France.

Kraus, W. 1988. Das Universalsichtgerät nach KRAUS / Lanooy. *Der Präparator* **34**(1), 347-350.

Metz, H. C. 1994. *Persian Gulf States: Country Studies*. Federal Research Division, Library of Congress, Washington, D.C.

Passchier, C. W. & Trouw, R. A. J. 2005. *Microtectonics*. Springer : Berlin, Federal Republic of Germany, Federal Republic of Germany.

Ramsay, J. G. & Huber, M. I. 1984. *The Techniques of Modern Structural Geology, Volume 1: Strain Analyses*. Academic Press.

Ray, S. F. 1999. *Scientific Photography and Applied Imaging*. Focal Press.

Razin, P. 2010. Stratigraphic localization of Discotheque Pavement in the Natih Formation, Personal communication.

Robertson, A. H. F. 1987. Upper Cretaceous Muti Formation; transition of a Mesozoic carbonate platform to a foreland basin in the Oman Mountains. *Sedimentology* **34**(6), 1123-1142.

Santrock, J., Studley, S. A. & Hayes, J. M. 1985. Isotopic analyses based on the mass spectra of carbon dioxide. *Analytical Chemistry* **57**(7), 1444-1448.

Schroiff, K. 2010. Tokina AF 12-24mm f/4 AT-X Pro DX (Nikon) - Review / Test Report. www.photozone.com.

Searle, M. P. 2007. Structural geometry, style and timing of deformation in the Hawasina Window, Al Jabal al Akhdar and Saih Hatat culminations, Oman Mountains. *GeoArabia [Manama]* **12**(2), 99-130.

van Buchem, F. S. P., Razin, P., Homewood, P. W., Oterdoom, W. H. & Philip, J. 2002. Stratigraphic Organization of Carbonate Ramps and Organic-Rich Intrashelf Basins: Natih Formation (Middle Cretaceous) of Northern Oman. AAPG Bulletin 86(1), 21-53.

Veizer, J. & Hoefs, J. 1976. The nature of O18/O16 and C13/C12 secular trends in sedimentary carbonate rocks. Geochimica et Cosmochimica Acta 40(11), 1387-1395.

Zoomify. Zoomify Express. Zoomify Inc. , Santa Cruz, California.

8 Appendix

8.1 Table: stable isotope measurements

Measure ID	Sample ID	$d^{18}O_{SMOW}$	$d^{13}C_{VPDB}$	type
183	JS-PL-001	22,76	1,26	vein
185	JS-PL-001	22,84	1,18	host rock
187	JS-PL-003	22,55	-0,84	vein
189	JS-PL-003	22,70	1,22	vein
2	JS-PL-004	23,26	0,92	vein
193	JS-PL-005	22,78	0,73	vein
4	JS-PL-006	23,15	0,39	vein
5	JS-PL-007	22,88	1,10	vein
195	JS-PL-009	22,96	0,43	vein
196	JS-PL-009	22,75	-0,77	vein
198	JS-PL-009	22,71	-0,77	vein
7	JS-PL-011	22,88	0,50	vein
8	JS-PL-011	23,25	0,42	vein
11	JS-PL-012	22,74	-0,36	vein
63	JS-PL-013	26,21	1,30	vein
65	JS-PL-013	24,22	1,20	vein
66	JS-PL-013	22,88	1,57	host rock
70	JS-PL-014	25,27	1,29	vein
72	JS-PL-014	23,43	1,23	vein
74	JS-PL-015	26,22	1,74	host rock
76	JS-PL-016	23,14	1,53	vein
77	JS-PL-016	25,69	1,34	vein
79	JS-PL-016	23,76	1,43	vein
84	JS-PL-019	24,53	1,21	vein
88	JS-PL-023	23,36	1,34	vein
90	JS-PL-023	23,90	1,06	vein
91	JS-PL-024	24,43	1,21	vein
92	JS-PL-024	23,72	1,17	vein
94	JS-PL-024	24,30	0,95	vein
13	JS-PL-028	22,86	0,81	vein
97	JS-PL-031	22,92	1,04	vein
95	JS-PL-031	22,62	1,34	host rock
205	JS-PL-033	22,93	0,99	vein
98	JS-PL-035	22,98	1,03	vein
99	JS-PL-035	22,80	1,01	vein
101	JS-PL-035	22,65	1,43	host rock
105	JS-PL-036	23,01	0,96	vein
106	JS-PL-036	22,71	1,12	host rock
206	JS-PL-039	22,96	0,15	vein

Measure ID	Sample ID	$d^{18}O_{SMOW}$	$d^{13}C_{VPDB}$	type
110	JS-PL-046	22,92	1,21	vein
111	JS-PL-046	22,97	0,79	vein
112	JS-PL-046	22,64	1,19	host rock
201	JS-PL-047	23,14	1,07	vein
202	JS-PL-047	23,14	0,88	vein
15	JS-PL-049	23,20	1,63	vein
16	JS-PL-049	23,85	1,38	vein
17	JS-PL-050	23,13	1,60	vein
18	JS-PL-050	23,02	1,60	vein
19	JS-PL-051	23,02	1,50	vein
20	JS-PL-051	23,19	1,54	vein
199	JS-PL-053	23,03	0,28	vein
46	JS-PL-055	23,05	1,39	vein
47	JS-PL-055	22,81	1,91	host rock
25	JS-PL-056	22,94	0,54	vein
27	JS-PL-057	22,85	-0,21	vein
114	JS-PL-060	22,85	1,71	host rock
117	JS-PL-061	23,13	1,47	vein
118	JS-PL-061	22,88	1,61	host rock
122	JS-PL-062	22,60	1,50	host rock
49	JS-PL-063	23,25	0,65	vein
52	JS-PL-063	23,37	1,65	host rock
54	JS-PL-064	23,19	1,35	vein
29	JS-PL-066	23,28	1,54	host rock
35	JS-PL-071	23,34	1,68	vein
208	JS-PL-072	23,38	2,15	vein
36	JS-PL-073	23,61	1,54	vein
37	JS-PL-073	23,34	1,61	vein
59	JS-PL-074	24,50	1,75	vein
38	JS-PL-079	23,12	0,38	vein
124	JS-PL-081	22,94	0,81	vein
125	JS-PL-081	23,00	1,12	vein
126	JS-PL-082	23,02	1,14	vein
127	JS-PL-082	23,40	1,49	vein
128	JS-PL-082	23,16	1,39	vein
132	JS-PL-083	24,03	0,89	vein
133	JS-PL-083	23,16	1,26	vein
135	JS-PL-091	23,96	1,48	vein
137	JS-PL-091	23,08	0,38	vein
141	JS-PL-094	23,81	1,79	vein
144	JS-PL-094	22,98	1,14	vein
140	JS-PL-094	23,19	1,44	host rock
145	JS-PL-095	22,90	0,32	vein

Measure ID	Sample ID	$d^{18}O_{SMOW}$	$d^{13}C_{VPDB}$	type
148	JS-PL-096	22,89	0,10	vein
149	JS-PL-096	23,36	1,88	vein
151	JS-PL-097	23,14	0,08	vein
152	JS-PL-097	23,28	0,83	vein
153	JS-PL-099	22,70	-0,33	vein
154	JS-PL-099	23,72	1,19	host rock
156	JS-PL-100	22,99	-0,16	vein
158	JS-PL-100	23,03	0,29	vein
161	JS-PL-102	23,18	1,15	vein
162	JS-PL-103	23,01	1,08	vein
165	JS-PL-103	22,87	0,23	vein
167	JS-PL-104	22,79	0,34	vein
168	JS-PL-104	23,23	0,89	vein
169	JS-PL-104	23,48	1,94	vein
170	JS-PL-104	23,69	2,09	vein
171	JS-PL-105	23,40	1,20	vein
175	JS-PL-105	23,37	1,87	vein
174	JS-PL-105	23,42	1,72	host rock
180	JS-PL-110	23,05	1,39	vein
181	JS-PL-110	23,33	1,45	vein

8.2

8.3 **Data disks**